

Study of Reaction Mechanisms on Single Crystal Surfaces with Scanning Tunneling Microscopy

Atomically resolved CO oxidation
on Pd(111) and RuO₂(110)

D I S S E R T A T I O N

zur Erlangung des akademischen Grades
d o c t o r r e r u m n a t u r a l i u m
(Dr. rer. nat.)

im Fach Physik

eingereicht an der
Mathematisch-Naturwissenschaftlichen Fakultät I
der

Humboldt-Universität zu Berlin

VON

Herrn M.Sc. Sang Hoon Kim

geboren am 22.10.1973 in Changnyoung, Korea

Präsident der Humboldt-Universität zu Berlin :
Prof. Dr. J. Mlynek

Dekan der Mathematisch-Naturwissenschaftlichen Fakultät I :
Prof. Dr. M. Lindscheid

Gutachter:

1. Prof. Dr. J. Wintterlin
2. Prof. Dr. H. Niehus
3. Prof. Dr. R. Imbihl

eingereicht am: 21. März 2003
Tag der mündlichen Prüfung: 9. Juli 2003

Zusammenfassung

Ziel dieser Arbeit war, die Rastertunnelmikroskopie, die bereits zur Aufklärung von einfachen Reaktionsmechanismen eingesetzt wurde, für *kompliziertere* Reaktionen anzuwenden. Die Oxidation von CO auf Pd(111) und auf einem RuO₂(110)-Film auf Ru(0001) wurde untersucht. Strukturelle Analysen ergeben mikroskopische Verteilungen der Adsorbate in den Überstrukturen von O und CO auf Pd(111) und RuO₂(110). Dynamische und quantitative Analysen der Reaktionen liefern die Kinetik und die Mechanismen der Reaktionen direkt auf der mikroskopischen Ebene.

O-Atome auf Pd(111) sind bei mittleren Bedeckungsgraden ($0.10 < \theta_{\text{O}} < 0.15$) und bei Probertemperaturen ($T_{\text{sample}} > 135$ K) beweglich. Die Aktivierungsenergie der Diffusion (E_{diff}^*) beträgt 0.54 ± 0.08 eV, der präexponentielle Faktor der Sprünge Γ_{O} beträgt $10^{16 \pm 3} \text{ s}^{-1}$. Bei niedrigen Bedeckungen ($\theta_{\text{CO}} \sim 0$) sind die CO-Moleküle auf Pd(111) schon bei $T_{\text{sample}} = 60$ K sehr beweglich. Wenn man einen präexponentiellen Faktor von $\Gamma_{\text{O}} = 10^{13} \text{ s}^{-1}$ annimmt, ergibt sich für E_{diff}^* von CO ein Wert von 0.15 eV. Adsorbiert CO auf der (2×2) -O-Überstruktur bei $T_{\text{sample}} > 130$ K, kommt es mit steigendem Bedeckungsgrad von CO zu Phasenübergängen, zunächst in eine $(\sqrt{3} \times \sqrt{3})$ R30°-O-Struktur, dann in eine (2×1) -Struktur. Während der Phasenübergänge nimmt die Mobilität der O-Atome zu, was sich in einer Abnahme der E_{diff}^* um 10 bis 20 % (unter der Annahme von $\Gamma_{\text{O}} = 10^{16} \text{ s}^{-1}$) im Vergleich zu einer CO-freien Oberfläche niederschlägt. Am Ende der Phasenübergänge entstehen aus einer fast völlig ungeordneten (O+CO)-Phase viele kleine (2×1) -Inseln, die sich zu größeren Inseln zusammensetzen. Die (2×1) -Inseln sind bereits bei $T_{\text{sample}} = 136$ K sehr reaktiv. Die quantitative Analyse der Abreaktion der (2×1) -Inseln ergibt, dass die Reaktionsrate proportional zur Inselfläche und nicht zur Randlänge ist. Die Reaktionsordnung bezüglich $\theta_{(2 \times 1)}$ ist ~ 1 . Unter der Annahme eines Vorfaktors k_{O} von 10^{13} s^{-1} wurde für diese Reaktion ein E_{reac}^* von 0.41 eV abgeschätzt. Für eine CO-Adsorption auf der (2×2) -O-Überstruktur bei $T_{\text{sample}} < 130$ K kommt es nicht zu einem Phasenübergang, sondern CO adsorbiert auf der (2×2) -O-Struktur.

Der RuO₂(110)-Film wurde bei Temperaturen zwischen 650 und 900 K auf der Ru(0001)-Probe aufgewachsen. Die Morphologie des Oxidfilms hängt stark von der Temperatur der Probe während des Wachstums (T_{prep}) ab. Bei $T_{\text{prep}} \sim 650$ K ist die Morphologie überwiegend kinetisch bestimmt. Mit steigender Temperatur bis $T_{\text{prep}} = 900$ K werden thermodynamische Effekte immer wichtiger. Die Dicke der Oxidschicht hängt nicht von T_{prep} ab und beträgt 7 Å bis 15 Å, was 2 bis 5 (Ru-O)-Monolagen entspricht. Die thermodynamische Stabilität der Morphologie ergibt sich aus Experimenten, in denen die Oxidschicht durch Heizen auf verschiedene Temperaturen

partiell verdampft wurde. Der Film dampft nicht lageweise ab, sondern es entstehen Löcher in der ansonsten unverdampften Oxidschicht. Die Löcher haben eine charakteristische Form. Sie bilden Parallelogramme oder Rechtecke mit einer langen Achse in [001]-Richtung. Die Oberflächenenergie γ_{001} der einen Flanke der Löcher ist 2 bis 5 mal größer als γ_{110} der anderen Flanke. Beim Verdampfen des Films verbleiben die freigesetzten Ru-Atome des Oxids auf dem Substrat. Sie bilden dort eine komplizierte Morphologie von hexagonalen und runden Inseln.

Die mikroskopischen Beobachtungen der chemischen Prozesse auf dem Film bestätigen die auf den makroskopischen Untersuchungen basierenden Modelle. Ein neuer Befund ist, dass die CO-Moleküle bei Raumtemperatur auf den Ru_{1f}-Reihen stabil adsorbieren, sobald die Ru_{2f}-Reihen vollständig mit CO bedeckt sind. Der maximale Bedeckungsgrad $\theta_{\text{CO}_{1f}}$ ist 0.5, die CO_{1f}-Moleküle bilden lokal geordnete (2×1)-, c(2×2)- und (1×1)-Überstrukturen. Allerdings kommt es bei $\theta_{\text{CO}_{1f}} \sim 0.5$ zu einer langsamen Desorption. Wenn man ein k_o von 10^{16} s^{-1} annimmt, lässt sich ein E_{des}^* von 1.00 eV abschätzen. Unter der Annahme von Γ_o und k_o von 10^{13} s^{-1} lassen sich E_{diff}^* -Werte für O und CO zwischen 0.89 und 0.93 eV abschätzen, und für die Reaktion zwischen CO_{1f} und O_{1f} ein Wert von $E_{\text{reac}}^* \sim 0.87 \text{ eV}$. Die Reaktionen zwischen O_{2f} und CO_{1f}, zwischen O_{1f} und CO_{2f} sowie zwischen O_{1f} und CO_{1f} verlaufen überwiegend statistisch. Manchmal wird eine leicht bevorzugte Reaktion quer zu den Ru_{1f}- und Ru_{2f}-Reihen beobachtet. Unter steady-state-Bedingungen kann CO bei genügend großem Partialdruck auf der Oberfläche adsorbieren. Unter steady-state-Bedingungen werden die gleichen CO_{1f}-Überstrukturen beobachtet wie in einer CO-Atmosphäre oder bei der Titration mit CO. Bei massiver Dosierung der Oxidoberfläche mit O₂ und CO ($\sim 100 \text{ L}$) werden weiße Flecken beobachtet, die CO_{1f} ähnlich sind. Allerdings reagieren diese weder mit O₂ noch mit CO, was auf einen anderen chemischen Zustand der RuO₂(110)-Oberfläche als den sauberen Zustand hinweist.

Schlagwörter:

Rastertunnelmikroskop, CO-Oxidation, Pd(111), Rutheniumdioxid

Abstract

Scanning Tunneling Microscopy has already been established as a tool for the investigation of simple reaction mechanisms. The aim of this thesis was to apply this technique to study *more complicated* reactions. The oxidation of CO on Pd(111) and on a RuO₂(110) film grown on Ru(0001) was investigated. Structural analyses of the O, CO and (CO+O) adlayers on Pd(111) and on RuO₂(110) reveal the microscopic distributions of the adsorbates on the surfaces. Dynamic and quantitative analyses of the reactions yield the reaction kinetics and the reaction mechanisms in a direct way at the microscopic level.

O atoms on Pd(111) at intermediate coverages ($0.10 < \theta_{\text{O}} < 0.15$) show mobility at sample temperatures (T_{sample}) higher than 135 K. The activation energy for diffusion is $E_{\text{diff}}^* = 0.54 \pm 0.08$ eV and the pre-exponential factor for hopping is $\Gamma_{\text{O}} = 10^{16 \pm 3}$ s⁻¹. CO molecules on Pd(111) at low coverages ($\theta_{\text{CO}} \sim 0$) show very high mobility, even at $T_{\text{sample}} = 60$ K. Assuming a value for Γ_{O} of 10^{13} s⁻¹, a value of 0.15 eV was estimated for E_{diff}^* for CO. Adsorption of CO molecules on a (2×2)-O adlayer at $T_{\text{sample}} > 130$ K causes phase transitions of the adlayer into the ($\sqrt{3} \times \sqrt{3}$) R30°-O structure and finally into the (2×1) structure. During the phase transitions, the mobility of the O atoms increases, reflected by a 10 ~ 20 % lower E_{diff}^* (under the assumption that $\Gamma_{\text{O}} = 10^{16}$ s⁻¹) than in the absence of CO. At the end of the phase transitions, many small patches with a (2×1) superstructure emerge from a disordered (CO+O) co-adlayer, which then agglomerate to form larger (2×1) islands. (2×1) islands are highly reactive even at $T_{\text{sample}} = 136$ K. The quantitative analysis of the reaction of the (2×1) islands reveals that the reaction rate is proportional to the total area of the islands, rather than to the total length of the boundary of the islands. The reaction order is ~ 1 with respect to $\theta_{(2 \times 1)}$. For E_{reac}^* a value of 0.41 eV was estimated under the assumption of a pre-exponential factor $k_{\text{O}} = 10^{13}$ s⁻¹. Adsorption of CO molecules on the (2×2)-O adlayer at $T_{\text{sample}} < 130$ K does not cause a phase transition, but CO adsorbs on the (2×2)-O islands.

The RuO₂(110) film was grown on a Ru(0001) surface between 650 K and 900 K. The morphology of the oxide film is strongly dependent on the sample temperature during the preparation (T_{prep}). The morphology of the oxide film is predominantly kinetically controlled at $T_{\text{prep}} \sim 650$ K, and thermodynamic effects become more important as T_{prep} is increased to 900 K. The thickness of the oxide film is independent of T_{prep} , and it ranges between 7 Å and 15 Å, corresponding to 2 to 5 oxide (Ru-O) monolayers. Partial evaporation of the oxide film by flashing the sample to various temperatures indicates the thermodynamic stability of its morphology. The film does not evaporate layer by layer, but holes emerge in the film, which have a

characteristic shape. They form parallelograms or rectangles, and are longer in the [001] direction. The surface free energy γ_{001} of the (vertical) side of such a hole is 2 to 5 times higher than γ_{110} . When the oxide film is evaporated, the Ru atoms from the oxide film remain on the substrate and form a complicated morphology of hexagonal or circular adatom islands.

The microscopic observations of the chemical processes on the film confirm the current model based on previous macroscopic studies. In addition, it was found that CO molecules adsorb in a stable form on the Ru_{1f} rows at room temperature once the Ru_{2f} rows are filled with CO. The maximum coverage $\theta_{\text{CO}_{1f}}$ is 0.5 and the molecules form locally ordered (2×1) , $c(2 \times 2)$ and (1×1) superstructures. However, CO_{1f} desorbs slowly at $\theta_{\text{CO}_{1f}} \sim 0.5$. Under the assumption that $k_o = 10^{16} \text{ s}^{-1}$, E_{des}^* can be estimated as 1.00 eV. E_{diff}^* for O or CO on the surface can be estimated to range between 0.89 eV and 0.93 eV and E_{reac}^* for the reaction between CO_{1f} and O_{1f} is ~ 0.87 eV, all under the assumption that Γ_o or $k_o = 10^{13} \text{ s}^{-1}$. The reactions between O_{2f} and CO_{1f}, O_{1f} and CO_{2f}, and O_{1f} and CO_{1f} are mostly statistical. However, a preferential reaction perpendicular to the Ru_{1f} and Ru_{2f} rows is occasionally observed. Under steady-state reaction conditions, CO can adsorb on the surface, provided that the partial pressure of CO is sufficiently high. The CO_{1f} superstructure is the same under steady-state conditions as that in a pure CO atmosphere or during CO titration. When the surface is exposed to very large doses of O₂ and CO ($\sim 100 \text{ L}$), white dots similar to CO_{1f} are observed on the surface. However, they do not react with either O₂ or CO. This observation suggests that the chemical properties of the oxide surface in this state are different from those of the original clean RuO₂(110) surface.

Keywords:

Scanning Tunneling Microscopy, CO oxidation, Pd(111), Ruthenium dioxide

Contents

1	Introduction	1
2	Experimental Setup	5
2.1	Scanning Tunneling Microscopy (STM)	5
2.2	Variable temperature STM	6
2.3	Room temperature STM	7
2.4	STM tip	8
2.5	Sample preparation	9
2.6	Experimental errors	10
3	CO oxidation on Pd(111)	11
3.1	Introduction to CO oxidation on Pd(111)	11
3.2	Preparation of a clean Pd(111) surface	14
3.3	O/Pd(111)	14
3.4	CO/Pd(111)	18
3.5	Structural analysis of the phase transition in the mixed (CO+O) adlayer on Pd(111)	21
3.5.1	Overall process of the phase transition	21
3.5.2	The compressed ($\sqrt{3} \times \sqrt{3}$) R30°-O structure	24
3.5.3	The (2×1) structure and the surrounding CO phase	25
3.6	Dynamic analysis of the phase transition in the mixed (CO+O) adlayer on Pd(111)	29
3.7	Quantitative analysis of the reaction in the mixed (CO+O) adlayer on Pd(111)	32
3.7.1	Evaluation procedure of the quantitative measurements	32
3.7.2	Reaction mechanism of the (2×1) structure	33
3.8	The (CO+O) adlayer on Pd(111) at $T < 130$ K	41
3.9	Summary	44

4	CO oxidation on RuO₂(110) grown on Ru(0001)	47
4.1	Introduction to the oxide film RuO ₂ (110) grown on Ru(0001)	47
4.2	Preparation of RuO ₂ (110)/Ru(0001)	50
4.3	Mesoscopic morphology of RuO ₂ (110)/Ru(0001)	51
4.3.1	Effect of preparation temperature on the morphology of the oxide film	51
4.3.2	Partial evaporation of the oxide film and its equilibrium morphology	56
4.3.3	The Ru(0001) substrate in the proximity of the oxide film	64
4.3.4	Summary of section 4.3	70
4.4	Clean RuO ₂ (110) surface	71
4.5	Structural analysis of the RuO ₂ (110) surface during CO and O ₂ adsorption	74
4.5.1	CO adsorption on the RuO ₂ (110)–(1 × 1) surface	75
4.5.2	O ₂ adsorption on the CO/RuO ₂ (110) surface	81
4.5.3	Summary of section 4.5	83
4.6	Analysis of the reaction dynamics and of the diffusion of CO and O on RuO ₂ (110)	84
4.6.1	Reaction between O _{2f} and CO _{1f}	84
4.6.2	Reaction between O _{1f} and CO _{1f}	87
4.6.3	Summary of section 4.6	93
4.7	Reversibility of the reaction and steady-state conditions	94
4.8	Summary	100
5	Conclusions	103

Acronyms and symbols

DFT	Density Functional Theory
FIM	Field Ion Microscopy
HREELS	High Resolution Electron Energy Loss Spectroscopy
LDOS	Local Density of States
LEED	Low Electron Energy Diffraction
PEEM	Photoemission Electron Microscopy
RHEED	Reflection High Energy Electron Diffraction
SEM	Scanning Electron Microscopy
STM	Scanning Tunneling Microscopy
TDS	Temperature Desorption Spectroscopy
UHV	Ultra High Vacuum
UPS	Ultraviolet Photoelectron Spectroscopy
XPS	X-ray Photoelectron Spectroscopy
$\text{CO(O)}_{1\text{f}(2\text{f})}$	CO(O) on a 1f(2f)-cus-Ru row
cus	coordinately unsaturated sites
E_a^*	effective activation energy of the process a
E_F	Fermi energy
ES	equilibrium shape
eV	electronvolt, $1 \text{ eV} = 1.602177 \times 10^{-19} \text{ J}$
I_T	tunneling current
k_B	Boltzmann constant
k_o	pre-exponential factor for desorption and reaction rate
L	Langmuir, $1 \text{ L} = 1 \times 10^{-6} \text{ Torr}\cdot\text{s}$
ML	monolayer, $1 \text{ ML} = \text{one adsorbate per one substrate atom}$
O_{br}	O atom on the bridge site in a 2f-cus-Ru row
P_a	partial pressure of gas a
$\text{Ru}_{1\text{f}(2\text{f})}$	1f(2f)-cus-Ru atom
T_{sample}	sample temperature
T_{prep}	sample preparation temperature
U_T	tunneling voltage with respect to the tip potential (sample bias)
Γ	hopping rate
Γ_o	pre-exponential factor for hopping rate
γ_a	surface free energy of surface a
θ_a	coverage of adsorbate a , <u>the number of adsorbate a on the surface</u> the number of surface atoms

Chapter 1

Introduction

The study of catalytic reactions on solid surfaces comprises one of the main parts of surface science [1]. One important source of information about elementary steps and reaction mechanisms is the kinetics of the reactions, i.e., the reaction rates as a function of macroscopic variables such as partial pressures of participating gases. One inherent problem of *macroscopic* kinetics is that it represents an average value over very many particles, and there can be more than one reaction mechanism on the atomic scale to reproduce the same kinetics.

Scanning Tunneling Microscopy (STM) can, in principle, give *direct* and *microscopic* information about reaction mechanisms. In fact, there have been already many STM studies about elementary steps of catalytic reactions such as about adsorption of reactants, dissociation of molecules on surfaces, diffusion of adsorbates on surfaces, and reaction between adsorbates down to the atomic scale [2]. These studies have been concentrated on simple adsorbates (O, N, CO, NH₃, etc.) and on simple reactions such as CO oxidation, and were performed under special conditions such as by titration, i.e., by reacting off an already adsorbed reactant by exposing the surface to another reactant.

Most STM studies about reactions on solid surfaces have been *qualitative* ones, and they mainly concern static structural analyses of the surface during the reaction. For comparison with the macroscopic kinetics, *quantitative* measurements such as of reaction rates on the atomic scale are necessary. Recently, it was demonstrated in our group that such a quantitative analysis is possible with STM [3, 4]. It was found that, in the CO oxidation on Pt(111), the reaction rate is proportional to the length of the boundary of oxygen islands on the surface. By measuring the reaction rates at different temperatures, the activation energy for the reaction could be also determined, and it was in

good agreement with the value previously obtained by the macroscopic method [5].

Such an analysis could be achieved with STM because CO oxidation on Pt(111) had already been investigated before in great detail with other methods, and it is known to occur in a simple way [6, 7]. The experiment was carried out as a titration, i.e., by reacting off an adsorbed O adlayer by exposing it to CO gas.

The aim of this thesis is to apply the demonstrated ability of STM to investigate the reaction mechanisms of more *complicated* reactions. For this purpose, the oxidation of CO on Pd(111) and on RuO₂(110) grown on Ru(0001) were investigated. The oxidation of CO on Pd(111) is known to be accompanied by structural phase transitions of the (CO+O) coadlayer during the reaction [6, 8]. The phase transitions themselves have not been investigated microscopically, and the reaction mechanism is expected to be strongly influenced by the phase transitions. RuO₂(110) films have recently been discovered to be the active phase for CO oxidation on Ru(0001) [9]. This oxide film is a very good model system because it forms under conditions similar to those for technical catalysts, but still allows studies at a fundamental level thanks to the metallic nature of RuO₂ [10] and to the single crystal form of the film.

The organization of this thesis is as follows. In chapter 2, I present the experimental setups. A variable temperature STM (VTSTM) and a room temperature STM (RTSTM) were used. The preparation of the STM tips and the shadow effect of the tip during measurements are discussed, and also the sample preparation and experimental errors. In chapter 3, I first present structures and diffusion properties of O/Pd(111) and CO/Pd(111), and then the structural and the dynamic analyses of the phase transition in the (CO+O) coadlayer. Quantitative measurements of the reaction kinetics of the CO oxidation on Pd(111) indicate that the reaction mechanism is different from that of the CO oxidation on Pt(111). In chapter 4, I first present mesoscopic and microscopic morphologies of the RuO₂(110)/Ru(0001) films under various preparation conditions. Then the adsorption of CO and O₂ on this surface are treated and afterwards the reaction between the CO molecules and the O atoms on the surface. The reaction kinetics was determined from titration experiments from which I propose a mechanism for the reactions between the O atoms and the CO molecules on the oxide surface. Finally, I present measurements under steady-state reaction conditions and under massive exposure to O₂ and CO gas. The relevance of applying the results from the titration study to the

reactions under those conditions is discussed.

Chapter 2

Experimental Setup

2.1 Scanning Tunneling Microscopy (STM)

The main experimental method used in this thesis is Scanning Tunneling Microscopy (STM). Here only a short description of STM is given; detailed introductions and explanations of this technique are available in monographs [11, 12, 13].

The STM technique was developed by Binnig, Rohrer, Gerber, and Weibel in 1981 at the IBM Research Center in Zurich [14, 15]. In the STM a sharp metal tip is brought close (several Å) to a sample surface, so that electrons can quantum mechanically tunnel through the vacuum gap between tip and sample. When a voltage V is applied between tip and sample, a tunneling current I flows through the gap. If the voltage V is low, the tunneling current I shows an exponential dependence on the width of the vacuum gap d as

$$I \propto V \cdot \exp(-A \cdot \sqrt{\bar{\varphi}} \cdot d), \quad (2.1)$$

where $A = 1.025 \text{ (eV)}^{-1/2} \text{Å}^{-1}$ and $\bar{\varphi}$ is the average potential barrier height of the gap [12]. For a typical value of the barrier height $\varphi \sim 4 \text{ eV}$, Eq. (2.1) shows that a 1 Å change in d roughly produces a change of one order of magnitude of I . This extremely sensitive dependence of I on d enables to precisely control the height of the tip above the surface. According to a theoretical study of Tersoff and Hamann, the tunneling current is proportional to the local density of states (LDOS) of a sample at the position of the tip apex [16, 17]. If one scans the sample surface with the tip while holding the current I constant (constant current mode) by adjusting the vertical position of the tip, one obtains an image of the topography of the scanned area from the recorded vertical

position of the tip. The resolution reaches the atomic scale, but the topography is a combination of geometric and electronic effects.

Experiments were carried out by means of two different STMs in our group. One is a variable temperature STM (VTSTM) with the ability of setting the sample temperature between 60 K and 300 K, the other is a room temperature STM (RTSTM).

2.2 Variable temperature STM

The UHV chamber housing the variable temperature STM was designed by T. Gritsch [18]. The UHV in the chamber is created by a pumping system consisting of a turbomolecular pump (Pfeiffer Vacuum, TPU 330), a diffusion pump (Leybold-Heraeus, Leybodiff 30L), and a rotary pump (Edwards, EDM 12). In addition, a titan sublimation pump and an ion pump (Leybold-Heraeus, NIZ-3-S) ensure a base pressure below 10^{-10} Torr. For the study of CO oxidation on Pd(111), an additional non-evaporable getter (NEG) pump (SAES getters, CapaciTorr CF100) was installed in order to reduce the partial pressure of H₂. H₂ can adsorb on Pd(111), dissolve into the bulk and cause undesirable side effects [19]. In order to isolate the STM from floor vibrations, the entire chamber can be decoupled from the floor by a pneumatic spring system (Newport, XL-A). The pressure in the chamber is measured with an ionization gauge (Varian, VT 971-0015), and the composition of the rest gas in the chamber and the pureness of dosed gases are checked with a quadrupole mass spectrometer (QMS) (Balzers, Prisma). The QMS is also used for thermal desorption spectroscopy (TDS). A Low Energy Electron Diffraction (LEED) with four grid optics (Varian) is installed as an additional surface characterization tool. The gases needed for experiments and preparations (O₂ purity 4.8; Ar purity 5.0 (Messer Griesheim), and CO purity unknown (Linde)) are dosed into the chamber through leak valves (Varian). The STM part is beetle type [20, 21] and was constructed by R. Schuster and J. Wintterlin [22].

Single crystals used as samples are fastened to molybdenum sample holders with stripes of a tantalum sheet ($t = 0.1$ mm) by spot welding. The sample can be held in a manipulator for preparation, or on a copper block for STM measurements. For preparation, the sample mounted to the manipulator can be heated to > 1000 °C by electron bombardment and be sputtered with an ion gun. After the preparation, the sample is transferred from the manipulator to the STM by a wobble stick. The

copper block of the STM is connected to a liquid helium cryostat by a copper braid, allowing to cool the sample to 60 K. The sample can be simultaneously heated by radiative heating from the back side, so that any temperature between 60 K and 300 K can be adjusted. The sample temperature is measured with Ni and NiCr wires spot welded on the back side of the sample (chromel-alumel, type K).

CO oxidation on Pd(111) was investigated with this STM because the reaction occurs too fast at room temperature [23].

2.3 Room temperature STM

The room temperature STM (RTSTM) is housed in another chamber. The pumping system and surface characterization tools are similar, but this chamber is additionally equipped with an Auger Electron Spectrometer (AES) (Varian). A detailed description of the chamber is found in [24]. The STM part is made of a piezodrives, which consists of three mutually perpendicular piezoelectric transducers. There is no temperature varying capability. The STM was originally constructed by J. Wiechers and J. Wintterlin [24, 25] and further developed by J. Wintterlin, J. Trost, and S. Renisch to allow for fast imaging at up to 20 frames/s [26, 27]. However, the video function was not used in this work.

In this chamber the RuO₂(110) experiments were performed. The preparation of RuO₂(110) required to dose the Ru(0001) surface with large amounts of O₂ ($> 10^5$ L, 1 L = 1×10^{-6} Torr·s) [28]. To keep the chamber pressure low during the O₂ exposure, a gas shower system was constructed as part of this thesis. The design was based on the one constructed by S. Schwegmann [29]. In the gas shower system, molecules from the gas container go through a multi channel plate (MCP) consisting of many pores (radius 10 μ m, length 3 mm) before they enter the chamber so that a directed beam of molecules is created. When the sample surface is brought close to the MCP (~ 1 mm), the local pressure of the gas on the sample surface is ~ 100 times higher than the background pressure in the chamber [30]. With the shower system, the total pressure in the chamber could be kept as low as 10^{-5} Torr during the RuO₂(110)/Ru(0001) preparation.

2.4 STM tip

The tips used in the study were predominantly fabricated electrochemically and occasionally mechanically. In the electrochemical method, a vertically fastened tungsten (W) wire ($\phi = 0.25$ mm for VTSTM and $\phi = 0.7$ mm for RTSTM) was etched in 2 M NaOH solution until the part below the etching neck broke off. The sharpest tip fabricated in this way had a tip radius of ~ 50 nm (Fig. 2.1a). For experiments in which gases are dosed during scanning, it is important that the tip is as sharp as possible. When the tip is blunt, the shadow effect of the tip prevents gas molecules to adsorb under the tip. The reaction is then limited by the adsorption rate of the gas molecules, and one cannot obtain the true reaction rate from such measurements. A freshly prepared tip with a radius of ~ 100 nm was sharp enough to suppress the shadow effect. However, when the tip was repeatedly crashed into the sample during coarse approach or intentionally to improve the resolution, the tip radius became as large as ~ 5 μm (Fig. 2.1b). Usually, such a crooked tip does not prevent images with atomic resolution. However, gas dosing experiments were affected.

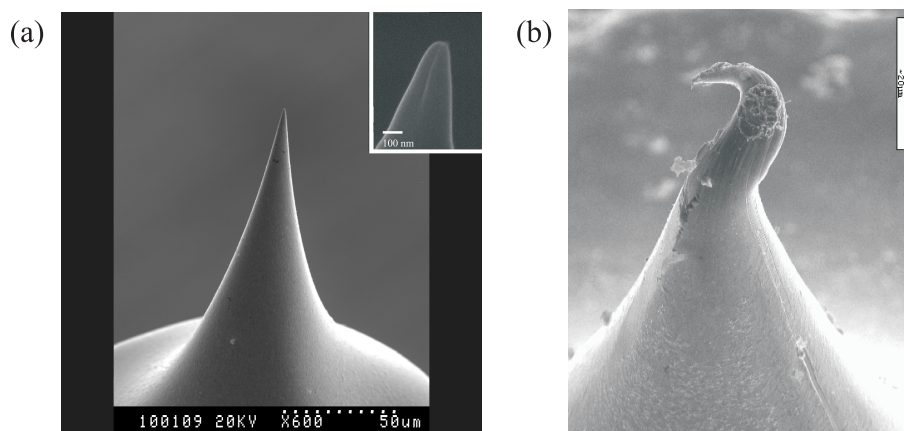


Figure 2.1: SEM image of the STM tip. (a) Directly after electrochemical preparation in 2 M NaOH solution. The inset shows that the tip radius is ~ 50 nm. (b) After some crashes against the sample. The tip is severely crooked, and the tip radius is as large as ~ 5 μm .

In the mechanical method, a Pt-Ir wire ($\phi = 0.25$ mm) was sharpened on a diamond grinder. A tip of this material was used to check a possible influence of O_2 gas on the standard W tips, causing instability of the tip during the scanning. Although the tip was not as sharp as

the electrochemically prepared one, atomic resolution was usually obtained. On the other hand, Pt-Ir tips did not show significantly higher stability than tips made from W.

During the measurements, it turned out that the tunneling parameters are also important to minimize the shadow effect. The smaller the tunneling voltage U_T and the higher the tunneling current I_T , the smaller is the distance d between the tip and the sample and the larger is the shadow effect. Of course, U_T cannot be made arbitrarily high and I_T arbitrarily low in order to make d large, because it is very difficult to obtain an atomic resolution under such conditions, and at high U_T (> 2 V) the electric field between tip and sample becomes too strong. Therefore, intermediate values were used, i.e., $0.2 \sim 0.8$ V for U_T and $0.4 \sim 7$ nA for I_T .

2.5 Sample preparation

The Pd(111) sample used in this work had already been used in another study [31]. Therefore, a routine preparation procedure was sufficient to get a well prepared Pd(111) surface. Main contaminants on Pd(111) were carbon and sulfur [32]. Sulfur could be removed by Ar^+ sputtering and carbon by exposing the surface to O_2 . Cleaning consisted of Ar^+ sputtering ($P_{\text{Ar}} = 1 \times 10^{-5}$ Torr, 1 keV, ion current $\sim 1 \mu\text{A}$), 3 to 4 cycles of oxidation ($P_{\text{O}_2} = 2 \times 10^{-7}$ Torr) at 700 K for ~ 10 minutes, and flashing to 1050 to 1100 K [31]. This flash temperature was sufficiently high to desorb residual O atoms from the surface. If the sample was flashed to higher temperatures than 1100 K, sulfur segregated again to the surface. A further contaminant was H_2 from the residual gas in the chamber that can adsorb on the surface and dissolve into the bulk. The H atoms can react with adsorbed O atoms to produce water [19], which makes the O adlayer on Pd(111) unstable. In order to minimize the amount of H_2 in the chamber, a NEG pump was added to the chamber as described in section 2.2. The pump reduced the amount of H_2 gas by one order of magnitude at 10^{-10} Torr. The cleanliness of the prepared Pd(111) was controlled by exposing the sample to ~ 10 L O_2 at room temperature and observing the $(2 \times 2)\text{-O/Pd(111)}$ structure with STM.

The Ru(0001) sample had also been used in previous studies [27, 33, 34, 35, 36] and was consequently well prepared. Therefore, only a routine preparation procedure was necessary. The cleaning included Ar^+ sputtering ($P_{\text{Ar}} = 1 \times 10^{-5}$ Torr, 1 keV, ion current $\sim 1 \mu\text{A}$), \sim

10 cycles of oxidation with 10 L O₂ at ~ 600 K to remove carbon contaminants, and flashing the sample up to 1300 K [27]. The cleanliness of the prepared Ru(0001) surface was checked with STM.

2.6 Experimental errors

Temperature

For measuring the temperature with the Ni-NiCr thermocouple, ice water was used as reference. In his thesis S. Völkening calibrated the temperature scale and found that the maximum error is 5 K at low temperatures and becomes smaller with increasing temperature [4].

Gas dosage

Gases were dosed for a determined time at a determined pressure. Gas pressures and times during dosing were relatively correctly measured (< 10 %). Opening and closing of the leak valve at the beginning and at the end of the dosage caused the largest error. In order to reduce the error when small amounts of gases were dosed, lower partial pressures of the gases and longer dosing times were applied. The overall error is estimated to be 20 %.

Chapter 3

CO oxidation on Pd(111)

3.1 Introduction to CO oxidation on Pd(111)

For the CO oxidation on Pt(111) it has recently been shown by STM that the reaction rate is proportional to the length of perimeters of oxygen islands on the surface [3, 4]. This finding means that the reaction only occurs at the boundary of oxygen islands. The result contrasts the usual assumption of a statistical distribution of reactants that underlies the usual construction of kinetic equations for surface reactions [37]. By measuring reaction rates at different temperatures, the activation energy for the reaction was also obtained.

On the background of these findings for the Pt(111) surface, a project was started to investigate the analogous reaction on Pd(111). It was expected that this surface may display even richer phenomena than the Pt case. CO oxidation on Pd(111) has been studied in detail with macroscopic methods [38]. It is well known that O-, CO-, and mixed (CO+O) adlayers form variously ordered structures on Pd(111). In analogy to Pt(111), the product molecule, CO₂, readily desorbs from the surface as soon as it is formed [39], and the reaction occurs between adsorbed particles (Langmuir-Hinshelwood (LH) mechanism) [38]. However, one major difference from the CO oxidation on Pt(111) is that on Pd(111) phase transitions occur in the (CO+O) coadlayer at low temperatures (< 230 K) [40].

When Pd(111) is exposed to ~ 10 L O₂ at room temperature, dissociatively adsorbed O atoms form a (2×2) superstructure, which is the saturated superstructure ($\theta_{\text{O}} = 0.25$) at room temperature [41]. H. Conrad et al. concluded from their LEED experiments that if the (2×2) -O structure is exposed to CO at 200 K, the O adlayer becomes compressed to a more dense $(\sqrt{3} \times \sqrt{3})$ R30° structure ($\theta_{\text{O}} = 0.33$).

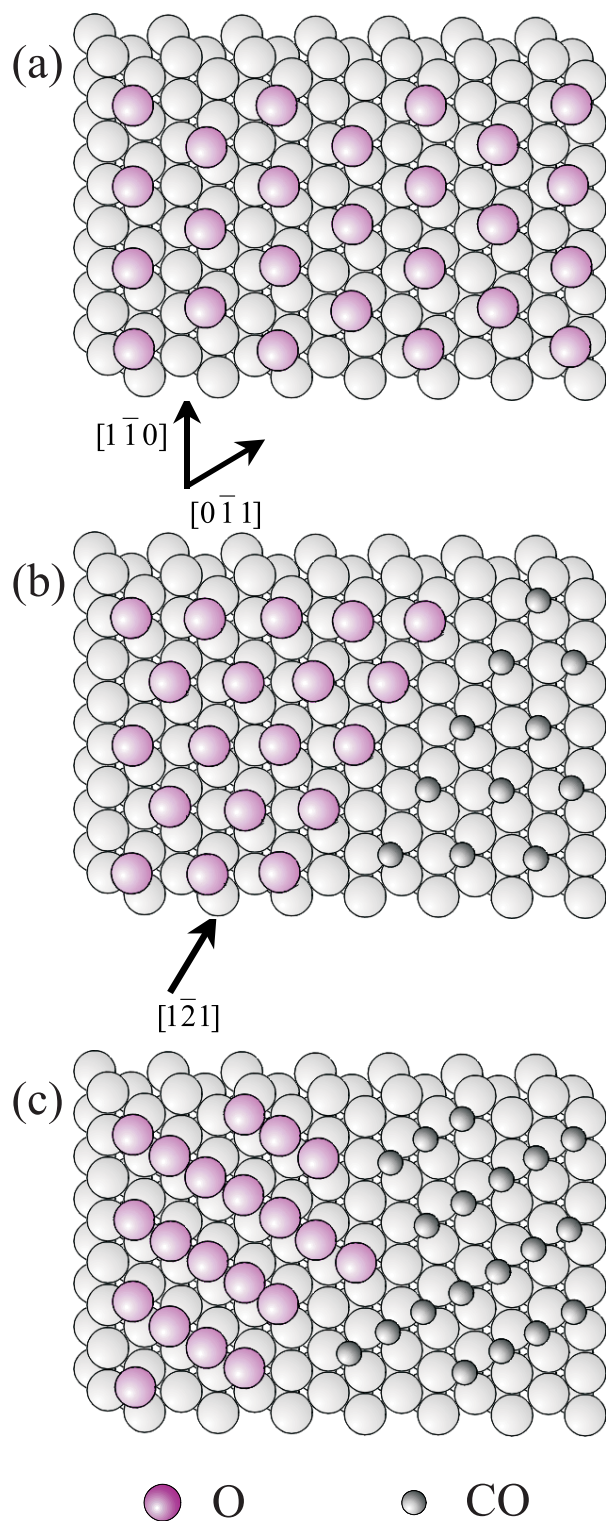


Figure 3.1: Model for the phase transition of the (CO+O) coadlayer on Pd(111). (a) (2×2) -O, (b) $(\sqrt{3} \times \sqrt{3})$ R30°-O and $(\sqrt{3} \times \sqrt{3})$ R30°-CO, (c) (2×1) -O and (2×1) -CO [31].

The adsorbed CO molecules also form an ordered structure, namely a $(\sqrt{3} \times \sqrt{3})$ R30° structure [8]. It was concluded that repulsive interactions between adsorbed O atoms and adsorbed CO molecules cause the formation of separated islands of O and CO. This compression of the O adlayer is a rather unusual phenomenon. Usually, when a (2×2) -O adlayer on a (111) metal surface is exposed to CO, a mixed (CO+O) adlayer is formed [42]. When the Pd(111) surface with the $(\sqrt{3} \times \sqrt{3})$ R30°-O and the $(\sqrt{3} \times \sqrt{3})$ R30°-CO adlayer is further exposed to CO at low temperatures (< 230 K), the O adlayer is even more compressed to a (2×1) structure. This structure is no longer formed when the sample temperature is higher than 230 K [40]. By observing CO₂ production at sample temperatures as low as 240 K in temperature desorption spectroscopy (TDS) experiments, H. Conrad et al. concluded that the (2×1) adlayer is highly reactive [8]. T. Matsushima et al. concluded that the CO oxidation involving the (2×1) adlayer occurs even at temperatures as low as ≤ 190 K, and that it occurs *inside* the (2×1) adlayer by angle resolved TDS [40]. On the other hand, it has not been clear so far if the (2×1) adlayer contains CO molecules or not. While early studies with UPS suggest that the (2×1) structure contains O as well as CO [8, 43], a recent DFT calculation suggests that separate (2×1) -O and (2×1) -CO islands are more stable [31]. The latest models for the phase transitions of the (CO+O) coadlayer on Pd(111) are shown in Fig. 3.1.

The models about the phase transitions of the (CO+O) coadlayer and the reaction of the (2×1) adlayer are entirely based on macroscopic studies. *Microscopic* observations are necessary to verify these models and to study the consequences. Particularly important is the question, if the density changes in the O and CO adsorbate phases - during coadsorption of O and CO on Pd(111) but not on Pt(111) - lead to different reaction mechanisms and kinetics in both cases. A *quantitative* measurement of the reaction kinetics to answer this question does not exist so far, neither microscopically nor macroscopically.

In this chapter, I first present the structure and the diffusion properties of the O/Pd(111) and CO/Pd(111) adlayers. Next, the phase transition of the (CO+O) coadlayer on Pd(111) is investigated. Then, I present quantitative measurements of the reaction kinetics of the CO oxidation involving the (2×1) islands. The results indicate that the reaction mechanism is different from that on the Pt(111) surface.

3.2 Preparation of a clean Pd(111) surface

The preparation method is described in detail in section 2.5. Main contaminants on Pd(111) are carbon and sulfur [32]. Carbon was removed by exposing the surface to O₂ and sulfur by Ar⁺ sputtering. A further contamination was H₂ from the rest gas that reacts with adsorbed O atoms to produce water [19], which makes the O adlayer on Pd(111) unstable. In order to minimize the amount of H₂ in the chamber, a special getter pump (NEG pump) was attached to the chamber (for details, see section 2.5).

For the preparation of the O adlayer, the cleaned Pd(111) surface was dosed with 10 to 20 L O₂ at room temperature. If the LEED displayed a clear (2 × 2) pattern, the temperature was lowered and an experiment was started. In the case of a diffusive or faint (2 × 2) pattern, the cleaning procedure was repeated until a clear LEED pattern was observed. Occasionally, the Pd(111) surface was exposed to smaller amounts of oxygen than 10 L to prepare O adlayers with $\theta_{\text{O}} < 0.25$. Because molecularly adsorbed O₂ on Pd(111) dissociates when the sample temperature is higher than 200 K [44], sometimes O adlayers were prepared by exposing the sample to ~ 3 L O₂ at a sample temperature of < 200 K, followed by heating the sample for a short time to ~ 220 K. The O adlayers obtained in this way usually have low coverages ($\theta_{\text{O}} \sim 0.10$).

3.3 O/Pd(111)

There are three ordered superstructures of O on Pd(111) known from LEED studies; a (2 × 2), a ($\sqrt{3} \times \sqrt{3}$) R30°, and a (1 × 1) superstructure [19, 41, 45]. There was a controversy whether the (2 × 2) pattern stems from a (2 × 2) adlayer ($\theta_{\text{O}} = 0.25$) or a (2 × 1) adlayer in three rotation domains ($\theta_{\text{O}} = 0.50$) [45]. The (2 × 2) LEED pattern turned out to originate from an (2 × 2)-O adlayer by an STM study [19]. H. Conrad et al. found that when the (2 × 2)-O/Pd(111) adlayer is further exposed to O₂ at 200 K, a more dense O adlayer giving a ($\sqrt{3} \times \sqrt{3}$) R30° LEED pattern is formed [41]. We investigated structures of the O adlayer with $\theta_{\text{O}} \leq 0.25$, which is relevant for the CO oxidation on Pd(111).

Fig. 3.2 shows an STM image of the (2 × 2)-O adlayer. Because the dark defects appear to be O vacancies, the hexagonally ordered white dots most likely are the O atoms. O atoms on metals are usually

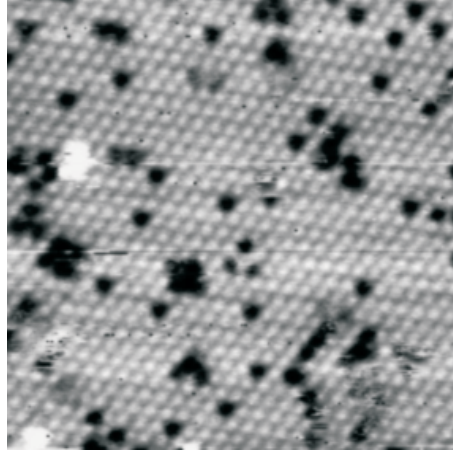


Figure 3.2: (2×2) -O adlayer on Pd(111). O atoms are imaged as white dots. Dark dots are vacancies. $U_T = 0.4$ V, $I_T = 2.2$ nA. $160 \text{ \AA} \times 160 \text{ \AA}$.

imaged as dark dots because the LDOS at E_F reduces due to the high electronegativity of an oxygen atom [27]. This was mostly the case also in our experiments, but imaging conditions as in Fig. 3.2 also occurred quite frequently. This different imaging is presumably due to chemisorption of an O atom at the apex of the tip [46].

For $\theta_O < 0.25$, O atoms form (2×2) islands, showing that it is the attractive interaction between O atoms that leads to the formation of the (2×2) superstructure (Fig. 3.3). Starting at ~ 135 K, O atoms on Pd(111) become mobile (Fig. 3.3a). The mobility of O atoms increases with increasing sample temperature (T_{sample}). At $T_{\text{sample}} = 152$ K, the boundaries of the islands show many diffusion events (Fig. 3.3b). At $T_{\text{sample}} = 185$ K, the O atoms are so mobile that islands form and disappear between two images. Most of the O atoms outside the islands are imaged as dashes (Fig. 3.3c), similarly as on Ru(0001) at room temperature [27]. In the series of such images the hopping rates of the O atoms were determined. At 137 K and 152 K, the number of O atoms that changed their positions could be counted directly. At 185 K, each dash represents an isolated O atom under the tip that jumps away when the tip comes back in the next scan line. In this case, the hopping rate was determined from the scanning frequency in horizontal direction (f_x), 4.8Hz, and from the relative number of two lines wide dashes that represent the probability that the O atom remains at the same site in the next line scan. This estimation is possible because the probability for each O atom to remain at the same adsorption site in

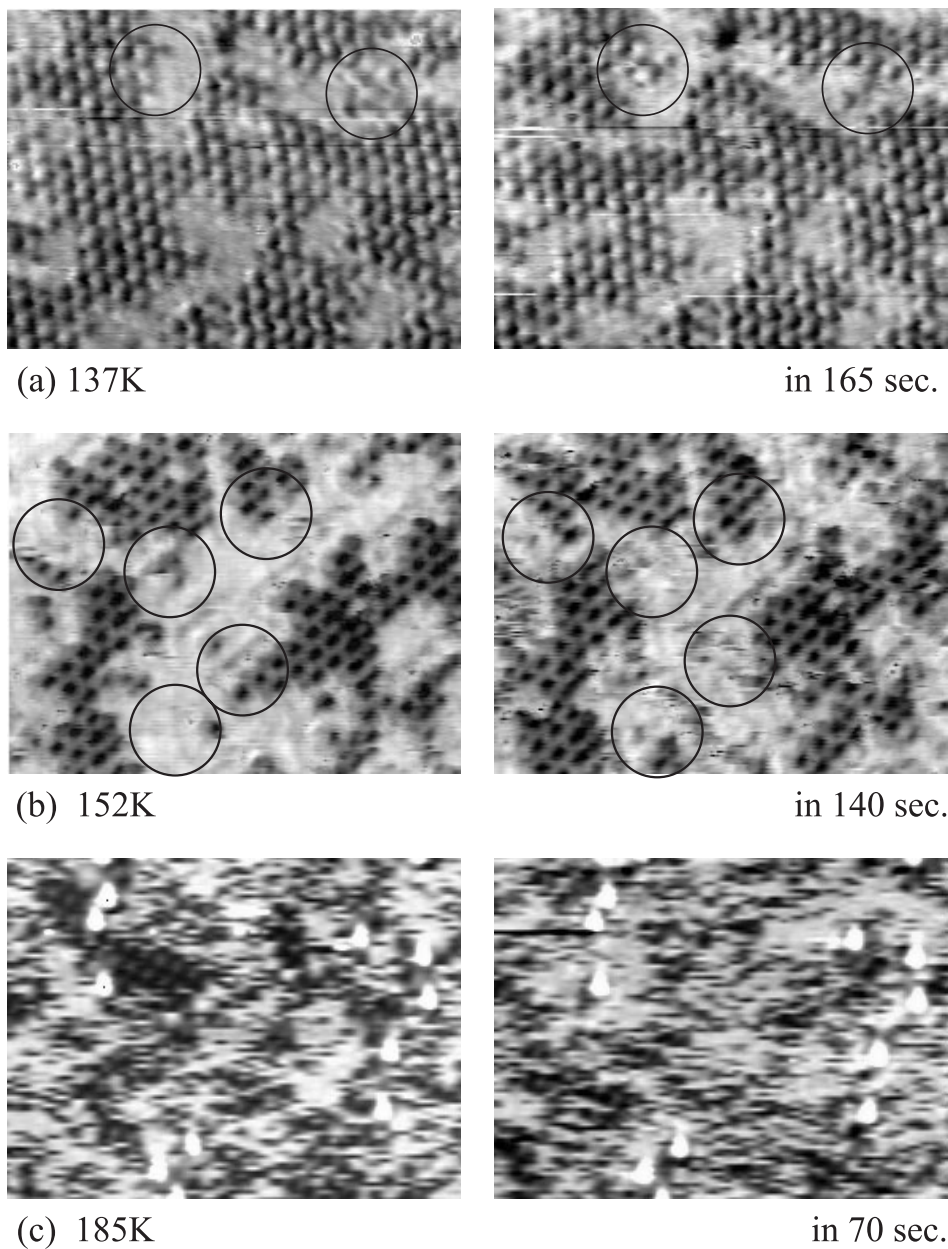


Figure 3.3: Diffusion of O atoms on Pd(111) at various temperatures. Each pair of images shows the same area with the time interval indicated below the images. O atoms are imaged as (a) white dots, (b) and (c) dark dots. (a) $U_T = 0.37$ V, $I_T = 2.2$ nA, (b) and (c) $U_T = 0.4$ V, $I_T = 0.7$ nA. $110 \text{ \AA} \times 80 \text{ \AA}$.

the time interval between two lines is given by a Poisson distribution [26, 27]. The hopping rates Γ at various T_{sample} are listed in Table 3.1. Note that the measured hopping rates include effects from interactions between O atoms, because the coverages of the O atoms are not small, namely $0.4 < \theta_{\text{O}}/\theta_{\text{O-max}} < 0.6$ (Table 3.1).

Table 3.1: Hopping rates of the O atoms on Pd(111) at various temperatures. The rates are calculated as the ratio of the number of hopped atoms to the number of total atoms

Temp.(K)	Coverage($\theta_{\text{O}}/\theta_{\text{O-max}}$)	Hopping rate $\Gamma(\text{s}^{-1})$
137	0.61	$(1.6 \pm 1.2) \times 10^{-4}$
152	0.39	$(3.6 \pm 2.0) \times 10^{-3}$
185	0.4 ~ 0.5	21 ± 10

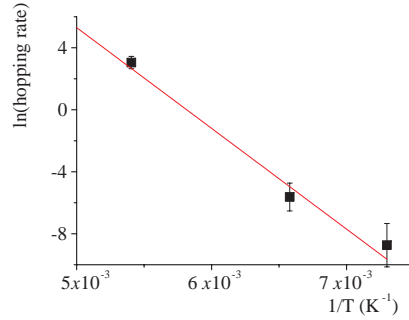


Figure 3.4: Arrhenius plot of the hopping rates of the O atoms on Pd(111). $E_{\text{diff}}^* = 0.54 \pm 0.08$ eV and $\Gamma_{\text{o}} = 10^{16 \pm 3} \text{ s}^{-1}$ are measured.

From the Arrhenius plot of the measured hopping rates, an activation energy for diffusion $E_{\text{diff}}^* = 0.54 \pm 0.08$ eV and a preexponential factor $\Gamma_{\text{o}} = 10^{16 \pm 3} \text{ s}^{-1}$ are obtained (Fig. 3.4). The adsorption energy of O_2 molecule $E_{\text{ad}}(\text{O}_2)$ on Pd(111) up to $\theta_{\text{O}} = 0.15$ measured by TDS is ~ 2.4 eV [41]. With the dissociation energy of O_2 $E_{\text{diss}}(\text{O}_2) = 5.2$ eV [6], the adsorption energy with respect to the atomic oxygen $E_{\text{ad}}(\text{O})$ is ~ 3.8 eV using $E_{\text{ad}}(\text{O}) = 1/2(E_{\text{ad}}(\text{O}_2) + E_{\text{diss}}(\text{O}_2))$ [6]. The value for E_{diff}^* thus appears reasonable considering that E_{diff}^* is usually 10 to 20 % of the adsorption energy [47], and it agrees well with a theoretical value of 0.59 eV from a DFT calculation [31]. The measured $E_{\text{diff}}^*(\text{O})$ on Pd(111) is also similar to values on other transition metal surfaces

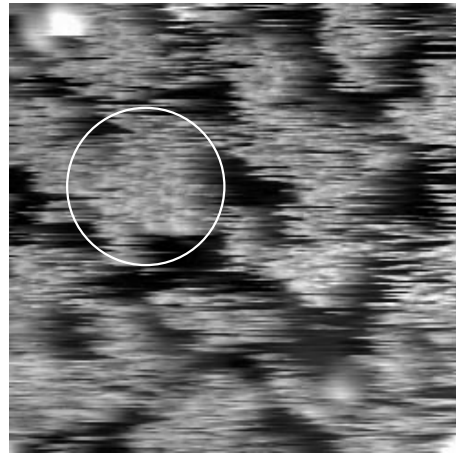
such as Pt(111) or Ru(0001), which are 0.43 eV and $0.55 \sim 0.7$ eV, respectively [48, 33]

3.4 CO/Pd(111)

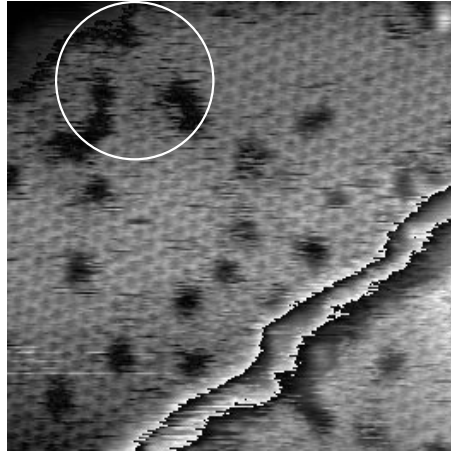
There are many more ordered structures of CO than of O on Pd(111). At least 17 ordered structures of CO/Pd(111) are known up to date [49]. At room temperature, CO forms a $(\sqrt{3} \times \sqrt{3})$ R30° superstructure at $\theta_{\text{CO}} = 0.33$, and a $c(4 \times 2)$ superstructure at $\theta_{\text{CO}} = 0.5$ [8]. Between $\theta_{\text{CO}} = 0.33$ and $\theta_{\text{CO}} = 0.5$, 5 ordered structures are known [49]. $\theta_{\text{CO}} = 0.5$ is the saturated coverage of CO at room temperature. At 90 K, the maximum coverage is 0.75 [50]. Compression of the adlayer from lower coverage to higher coverages is most likely not continuous, but a sequence of discrete, ordered structures [51]. $(\sqrt{3} \times \sqrt{3})$ R30°, $c(4 \times 2)$, and (2×2) ($\theta_{\text{CO}} = 0.75$) superstructures were recently observed with STM [52]. For the present study of CO oxidation, the relevant coverage range is ≤ 0.5 .

Fig. 3.5 shows adsorbed CO on Pd(111) for $\theta_{\text{CO}} \leq 0.5$. After an exposure of 0.4 L CO at 70 K, fluctuating islands with a $(\sqrt{3} \times \sqrt{3})$ R30° structure are resolved (Fig. 3.5a). CO molecules at the boundary of the islands are mobile and are imaged as streaks. Individual CO molecules outside the islands are too mobile to be imaged with STM. The fully developed $(\sqrt{3} \times \sqrt{3})$ R30°-CO adlayer with $\theta_{\text{CO}} = 0.33$ is observed after adsorption of 0.8 L CO (Fig. 3.5b). In this case, the hexagonally ordered dark dots must be the CO molecules. CO molecules on Pd(111) are usually imaged as white dots; the different imaging is presumably due to the presence of an O atom or a CO molecule at the apex of the tip (section 3.3). Streaky regions near the vacancies (circle) show that CO molecules near the vacancies are still mobile. When the $(\sqrt{3} \times \sqrt{3})$ R30°-CO/Pd(111) adlayer is further exposed to CO, striped patterns are formed indicating the $c(4 \times 2)$ -CO structure (Fig. 3.5c) [52].

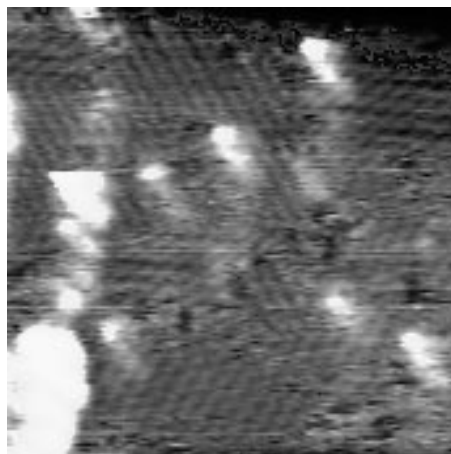
Fig. 3.5a shows that individual CO molecules outside the CO islands are not resolved even at $T_{\text{sample}} = 70$ K. At $T_{\text{sample}} = 60$ K, the lowest accessible temperature in our STM, individual CO molecules show instant formation and dispersion of $(\sqrt{3} \times \sqrt{3})$ R30° islands (Fig. 3.6). The surface was first exposed to a very small amount of O₂ (0.02 L), then to 0.6 L of CO. Individual CO molecules are still imaged only as dashes (Fig. 3.6b, arrow). Only at the borders of O₂ islands, CO molecules are sufficiently immobilized and form islands. The island formation of CO shows that there are attractive interactions between



(a) CO 0.4L



(b) CO 0.8L



(c) CO 5.0L

Figure 3.5: CO on Pd(111) at $\theta_{\text{CO}} \leq 0.5$. (a) Fluctuating islands of CO with $\theta_{\text{CO}} < 0.33$. Locally ordered $(\sqrt{3} \times \sqrt{3})$ R30° structures exist in the islands (circle). CO molecules outside of the islands are mobile and appear as streaks. $U_{\text{T}} = -0.5$ V, $I_{\text{T}} = 2.2$ nA. (b) The $(\sqrt{3} \times \sqrt{3})$ R30°-CO structure on Pd(111). Dark areas are vacancies. $U_{\text{T}} = -0.3$ V, $I_{\text{T}} = 3.8$ nA. (c) The $c(4 \times 2)$ -CO structure on Pd(111). Different domains are observed. White bumps are contaminants. $U_{\text{T}} = -0.8$ V, $I_{\text{T}} = 2.2$ nA. $T_{\text{sample}} = 70$ K. $90 \text{ \AA} \times 90 \text{ \AA}$.

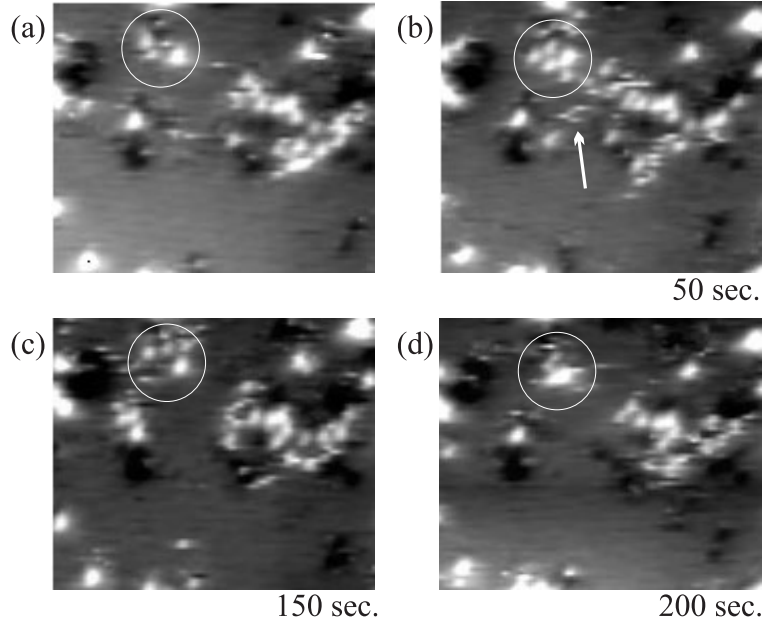


Figure 3.6: Diffusion of individual CO molecules on Pd(111). The series shows the same area after exposure to 0.02 L O₂ and 0.6 L CO at $T_{\text{sample}} = 60$ K. Dark areas are occupied with O₂. An instant formation of a $(\sqrt{3} \times \sqrt{3})$ R30°-CO island is observed (circle) near the O₂ islands. CO molecules are imaged as white dots. $U_{\text{T}} = -0.2$ V, $I_{\text{T}} = 0.6$ nA. $100 \text{ \AA} \times 80 \text{ \AA}$.

CO molecules that enable the formation of the $(\sqrt{3} \times \sqrt{3})$ R30°-CO superstructure (Fig. 3.5).

The mobility of CO at 60 K can be estimated from the series in Fig. 3.6. If one compares Fig. 3.6 with Fig. 3.3c, one finds a similar behavior of the particles. They form islands, and the islands dissipate in a short time. Therefore, the mobility of the O atoms at $T_{\text{sample}} = 180$ K is similar to the mobility of the CO molecules at $T_{\text{sample}} = 60$ K, in the order of 10 s^{-1} . Individual and immobile CO molecules have been imaged with STM at $T_{\text{sample}} = 25$ K [53]. Assuming a preexponential factor of 10^{13} s^{-1} , the usual assumption for adsorbates on metal surfaces, a diffusion barrier of $E_{\text{diff}}^* = 0.15$ eV is estimated from the data presented here.

The adsorption energy of CO on Pd(111) up to $\theta_{\text{CO}} = 0.33$ has been measured by analyzing adsorption isotherms and by molecular beam experiments to be 1.4 to 1.5 eV [54, 55]. The value of $E_{\text{diff}}^* = 0.15$ eV is thus about 10 % of the adsorption energy, in agreement with our expectation. That the value with respect to E_{ad} is smaller than for O

is probably due to the fact that CO is a molecule. In general, CO is very mobile on transition metals [9]. A. Seitsonen et al. found in their DFT calculations that the adsorption energies of CO on various sites, such as on-top, bridge, and 3-fold hollow on Ru(0001) and Rh(111) are very similar to each other (± 0.1 eV) [31]. On Pt(111), the situation is similar [56]. Because the adsorption energies are alike, CO molecules can easily hop from one adsorption site to another.

3.5 Structural analysis of the phase transition in the mixed (CO+O) adlayer on Pd(111)

3.5.1 Overall process of the phase transition

Fig. 3.7 shows structural changes of the (CO+O) coadlayer as the (2×2) -O adlayer is exposed to CO at $T_{\text{sample}} \sim 140$ K. The T_{sample} is near the lowest temperature at which the phase transition occurs (130 K). Although previous investigations suggested the onset of the reaction at ≤ 190 K [40], reaction to CO₂ had not been expected to occur at such a low temperature. Before the surface was exposed to CO, the STM tip was withdrawn in order to exclude shadow effects of the tip. The images in Fig. 3.7 do not show the same area, but they show characteristic features.

Fig. 3.7a shows the (2×2) -O adlayer with some vacancies. The hexagonally ordered dark dots are O atoms, the white dots vacancies. Most of the white dots are isolated, but some form short chains. When the adlayer is exposed to CO, the number of these chains increases (Fig. 3.7b). This observation could mean a local lifting of the (2×2) order by the displacement of O atoms, or CO molecules occupy sites within the (2×2) structure and appear bright. For the latter case, mixing of some CO into the (2×2) -O superstructure is energetically plausible. A DFT calculation by A. Seitsonen et al. shows that the energy of the mixed (2×2) -(O+CO) per unit cell is only ~ 0.6 eV higher than the separate (2×2) -O and (2×2) -CO structures [31].

When the adlayer is further exposed to CO, compression of the (2×2) -O adlayer occurs (Fig. 3.7c). White dots are CO molecules, and the dark area is the O adlayer. Although individual O atoms in the O adlayer are not resolved, the internal structure of the O adlayer shows that the ordering of the O adlayer is the same as the ordering of white

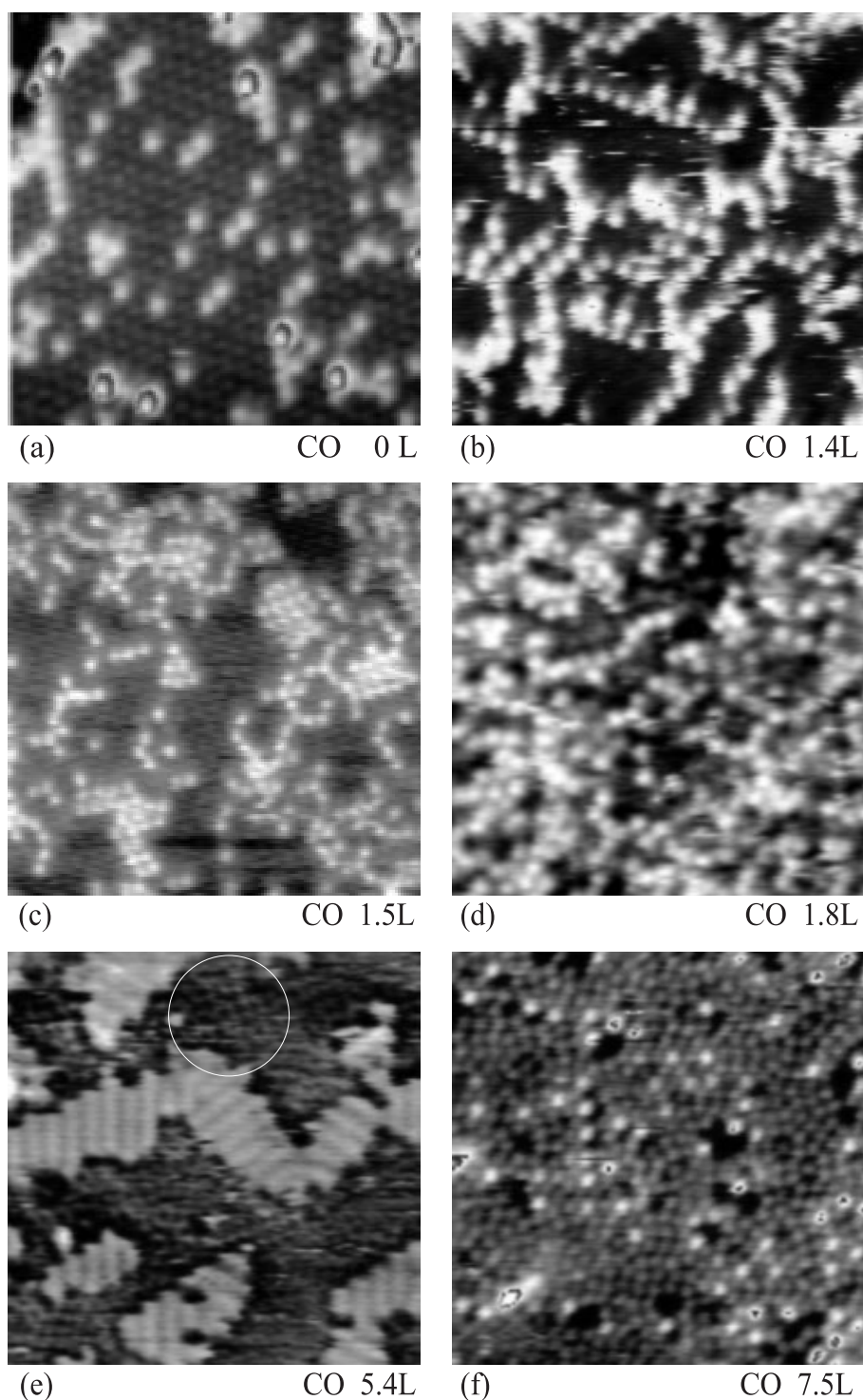


Figure 3.7: Static observation of the phases occurring during adsorption of CO on the oxygen covered Pd(111) surface. The images are from several measurements, i.e., they do not show the same area. (a) (2×2) -O, (b) (2×2) -O + CO chains in the (2×2) structure, (c) small islands of $(\sqrt{3} \times \sqrt{3})$ R30°-O and $(\sqrt{3} \times \sqrt{3})$ R30°-CO, (d) mixed and disordered coadlayer of (CO+O), (e) (2×1) islands and surrounding CO adlayer, (f) disordered CO adlayer after the (2×1) islands have reacted off. $U_T =$ (a), (e), and (f) 0.4, (b) 0.5, (c) and (d) -0.3 V, $I_T =$ (a) 0.7 and (b)–(f) 2.2 nA. $T_{\text{sample}} \sim 140$ K. $120 \text{ \AA} \times 120 \text{ \AA}$.

dots. White dots are arranged in a $(\sqrt{3} \times \sqrt{3})$ R30° superstructure, as seen from the 30° rotation of the structure with respect to Fig. 3.7a. The dark areas in between also display a $(\sqrt{3} \times \sqrt{3})$ R30° structure.

The compression shows that the $(\sqrt{3} \times \sqrt{3})$ R30°-O superstructure originates from a *repulsive* interaction between O and CO. Note that the (2×2) -O superstructure is due to *attractive* interactions between O atoms, and $(\sqrt{3} \times \sqrt{3})$ R30°-CO islands are also due to *attractive* interactions between CO molecules. The findings are in agreement with the calculations by A. Seitsonen et al. [31], according to which CO molecules and O atoms form separate $(\sqrt{3} \times \sqrt{3})$ R30° structures. In their calculations, the mixing energy for a mixed $(\sqrt{3} \times \sqrt{3})$ R30°-(CO+O) per unit cell is even 2.83 eV [31]. Therefore, separate $(\sqrt{3} \times \sqrt{3})$ R30°-O and $(\sqrt{3} \times \sqrt{3})$ R30°-CO islands are strongly favored over a mixed $(\sqrt{3} \times \sqrt{3})$ R30°-(O+CO) adlayer.

With more CO, the mixed (CO+O) coadlayer becomes disordered (Fig. 3.7d). This state is the most unstable one in the phase transition and was observed for a very short time in the in situ experiments (section 3.6).

With further CO exposure, the disordered phase orders into (2×1) islands and a surrounding CO adlayer with $\theta_{\text{CO}} \sim 0.5$ (Fig. 3.7e). White islands display parallel and 30 to 50 Å long stripes, which represent the (2×1) structure. Three equivalent growth directions of the island are observed in the image. The atomic structure of the islands is shown in Fig. 3.11. Between the islands, local $c(4 \times 2)$ ordering of the surrounding CO adlayer was observed (circle in Fig. 3.7e), which is better resolved in Fig. 3.10. The shape of the (2×1) islands in Fig. 3.7e is typical. The length of the (2×1) islands perpendicular to the stripes reaches as long as ~ 100 Å, corresponding to an aspect ratio of up to 1 : 3.

With further exposure to CO, the (2×1) islands react off even at $T_{\text{sample}} = 140$ K, extending the previous reports of a minimum reaction temperature of ≤ 190 K [40]. Our data show that the reaction occurs as long as the phase transition can occur, i.e., at $T_{\text{sample}} > 130$ K. After the reaction, the Pd(111) surface is fully covered with adsorbed CO (Fig. 3.7f). The CO adlayer is globally disordered, but locally it displays the $c(4 \times 2)$ superstructure.

Each stage of the phase transition will be discussed in detail in the following sections.

3.5.2 The compressed ($\sqrt{3} \times \sqrt{3}$) R30°-O structure

Fig. 3.7c shows that ($\sqrt{3} \times \sqrt{3}$) R30°-O domains indeed exist separately from the ($\sqrt{3} \times \sqrt{3}$) R30°-CO domains. Fig. 3.8 shows further details of the formation of the compressed ($\sqrt{3} \times \sqrt{3}$) R30°-O structure. The initial (2×2)-O adlayer was exposed to ~ 1.6 L CO at $T_{\text{sample}} = 144$ K. White dots are O atoms, and they form well ordered ($\sqrt{3} \times \sqrt{3}$) R30°-O islands. The internal structure of the CO area is not resolved, but it is clear that many disordered O atoms are mixed with CO. This observation means that the phase transition is limited by the mobility of the O atoms. The repulsive interaction between CO and O is strong enough to compress the (2×2)-O adlayer to form the ($\sqrt{3} \times \sqrt{3}$) R30°-O structure, but not so strong to repel O atoms outside of the CO domain.

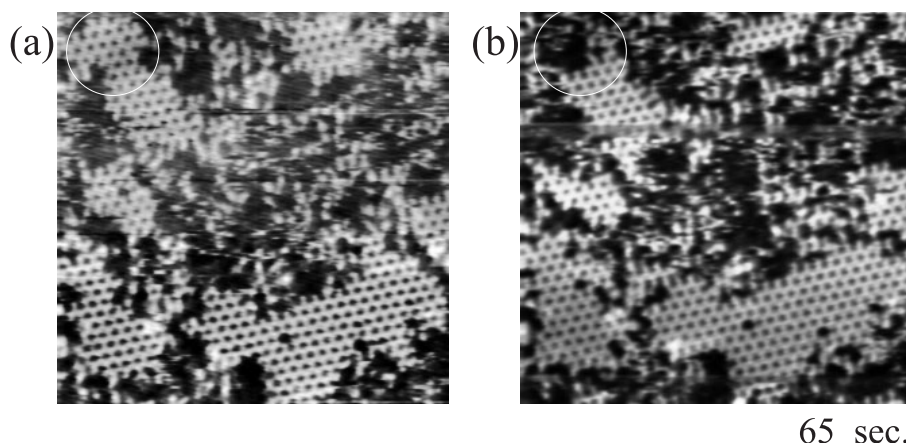


Figure 3.8: ($\sqrt{3} \times \sqrt{3}$) R30°-O islands with a disordered CO adlayer. O atoms are imaged as white dots. (b) shows the same area as (a) after 65 seconds. O atoms in the CO adlayer show a higher mobility than the O atoms without CO. $U_T = 0.6$ V, $I_T = 0.4$ nA. $T_{\text{sample}} = 144$ K. $130 \text{ \AA} \times 145 \text{ \AA}$.

However, the mobility of the O atoms in the CO domains is higher than on the empty surface (cf. Fig. 3.3a with Fig. 3.8b). Even entire islands disappear (circle), indicating a lowering of the adsorption energy of O atoms by the repulsive interaction from CO molecules.

The reduction of E_{diff}^* can be quantified by comparing the hopping rate of O atoms without CO (Γ_1) and the rate estimated from the series in Fig. 3.8 (Γ_2) at $T_{\text{sample}} = 144$ K. Γ_1 at $T_{\text{sample}} = 144$ K is estimated as $7 \times 10^{-4} \text{ s}^{-1}$ (Fig. 3.4). For Γ_2 only a crude estimation is possible because O atoms hop many times between two successive images. A

lower limit follows from the assumption that O atoms which change their positions between two successive images hop only once. Γ_2 must then be higher than the hopping rate of the O atoms on the empty surface at 152 K, $(3.6 \pm 2.0) \times 10^{-3} \text{ s}^{-1}$ (Table 3.1). An upper limit is given by the rate at $T_{\text{sample}} = 185 \text{ K}$, $21 \pm 10 \text{ s}^{-1}$ (Table 3.1) because larger O islands do not float like the O islands on the empty surface at $T_{\text{sample}} = 185 \text{ K}$ (Fig. 3.3). Γ_2 is thus between 10^{-2} and 10^{-1} s^{-1} , between a factor of 10 and 10^2 higher than Γ_1 . If we use the measured Γ_{O} of O on Pd(111), 10^{16} , from section 3.3, E_{diff}^* from Γ_2 is 0.47 to 0.50 eV. This value is 10 to 20 % lower than the measured $E_{\text{diff}}^* = 0.54 \text{ eV}$ for O atoms without neighboring COs (section 3.3).

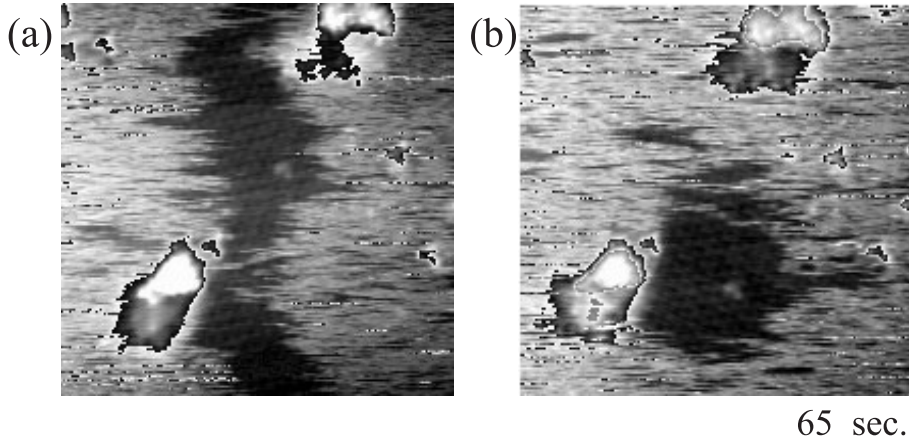


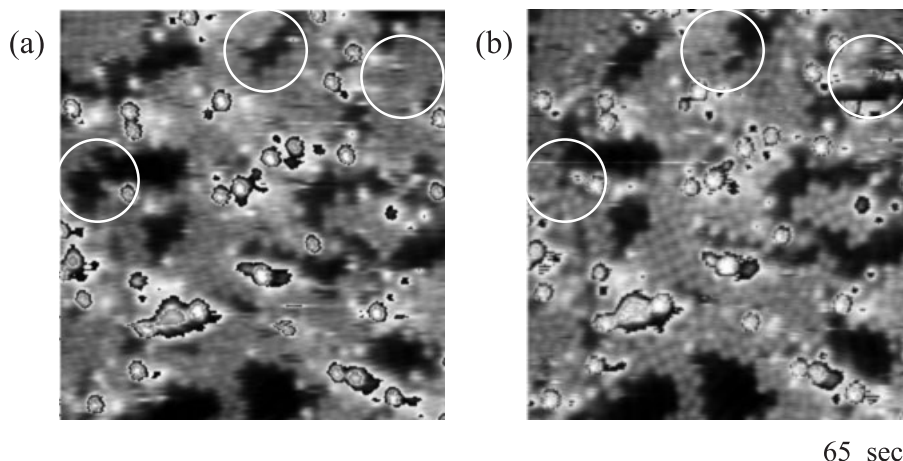
Figure 3.9: (a) $(\sqrt{3} \times \sqrt{3})$ R30°-O island at higher T_{sample} . (b) shows the same area as (a) after 65 seconds. $U_{\text{T}} = -0.4 \text{ V}$, $I_{\text{T}} = 0.7 \text{ nA}$. $T_{\text{sample}} = 180 \text{ K}$. $110 \text{ \AA} \times 110 \text{ \AA}$.

The situation remains similar at higher temperatures. Fig. 3.9a shows a compressed $(\sqrt{3} \times \sqrt{3})$ R30°-O island after the (2×2) -O adlayer was exposed to 2 L CO at $T_{\text{sample}} = 180 \text{ K}$. The O island is floating rapidly as shown in Fig. 3.9b. Without CO a similarly high mobility is reached at a temperature 5 K higher (Fig. 3.3c).

3.5.3 The (2×1) structure and the surrounding CO phase

The atomic structure of the CO phase between the (2×1) islands is resolved in Fig. 3.10. Here, (2×1) islands are imaged as dark areas and CO molecules as gray dots. White bumps are contaminants. The

local rectangular ordering in the CO phase is caused by the $c(4 \times 2)$ superstructure. The CO molecules adapt themselves to the shape and position of the (2×1) islands and form an ordered structure along the boundaries of the (2×1) islands. Therefore, the CO adlayer does not have a global ordering.



65 sec.

Figure 3.10: Mobility of the (2×1) islands and $c(4 \times 2)$ structure of CO adlayer after the phase transition. (2×1) islands are prepared by exposing the initial (2×2) -O adlayer to 5.4 L CO. CO molecules are imaged as gray dots. Dark area is (2×1) islands. White bumps are contaminants. (b) shows the same area as (a) in 65 seconds. Mobility of the shape of (2×1) islands is indicated with circles. $U_T = 0.4$ V, $I_T = 0.7$ nA. $T_{\text{sample}} = 134$ K. $105 \text{ \AA} \times 105 \text{ \AA}$.

In contrast to the CO areas surrounding the $(\sqrt{3} \times \sqrt{3})$ R30°-O islands (Fig. 3.8), the CO domains surrounding the (2×1) islands do not contain single O atoms. This strict separation of the (2×1) domains and the CO phase indicates that the repulsive force between CO and O becomes strong enough to repel all the isolated O atoms outside the CO phase (cf. with Fig. 3.8). This difference between the repulsive forces is also reflected by the dynamic behaviour. While the $(\sqrt{3} \times \sqrt{3})$ R30°-O islands are almost floating at $T_{\text{sample}} = 180$ K (Fig. 3.9), (2×1) islands are less mobile at the same temperature. There is only some change of shape of the islands similar to the changes shown in Fig. 3.10, which is at a lower temperature (indicated with circles).

Fig. 3.7e shows that after the phase transition, about 34 % of the total area is covered by (2×1) islands. We have never observed the (2×1) covered area to exceed ~ 50 % of the total area. This loss in O coverage is caused by the fact that already some reaction has occurred in this stage. The highest (2×1) coverage was achieved

by minimizing the reaction by controlling the CO coverage. This was achieved by exposure of the (2×2) -O adlayer to 1 L CO at $T_{\text{sample}} = 170$ K, followed by very slow heating (within about 1 hour) the sample to 180 K to activate the phase transition only thermally, without further exposure to CO. The phase transition indeed occurred very slowly, and the (2×1) islands occupied 53 % of the total area (Fig. 3.11a). From this observation we conclude that the density of O atoms in the (2×1) structure is twice as high as the density of O atoms in the (2×2) -O adlayer, as expected from the symmetry and previous studies [8, 40], and that there does not occur reaction during the phase transition.

The structure along the rows in the (2×1) phase was resolved only in exceptional cases. One example is shown in Fig. 3.11b. The suggested model for the (2×1) structure (Fig. 3.11b) assumes that the islands consist of O atoms only [31]. Whether the (2×1) islands also contain CO molecules is still controversial [8, 31, 40, 43]. Early studies with UPS observed a lowering of the ionization energy of the CO 4σ level in the presence of the (2×1) structure [8, 43]. An angle resolved TDS experiment showed that the product molecule, CO_2 , is highly collimated to the surface normal in the same situation [40]. These studies were taken as evidence that the (2×1) structure consists of O as well as CO. However, the DFT calculation by A. Seisonen et al. strongly indicates that separate (2×1) -O and (2×1) -CO islands are more stable [31]. From the STM data alone it cannot be decided if the image in Fig. 3.11b resolves O atoms or CO molecules between the O atoms. However, considering the clear result of the DFT investigation and the rather indirect evidence for CO in the (2×1) phase, it will be assumed that the (2×1) structure is a pure O phase.

Once the (2×1) islands have formed, the species near the boundaries (inside as well as outside) of the islands show some mobility at $T_{\text{sample}} > 130$ K. The shape of the islands changes (circles in Fig. 3.10). With increasing temperature, the mobility increases somewhat, but it is never so high that the entire islands are floating like the $(\sqrt{3} \times \sqrt{3})$ $\text{R}30^\circ$ -O islands in Fig. 3.9. The island coverage remains constant, i.e., there does not occur any reaction without exposing the sample to CO gas at $T_{\text{sample}} > 130$ K.

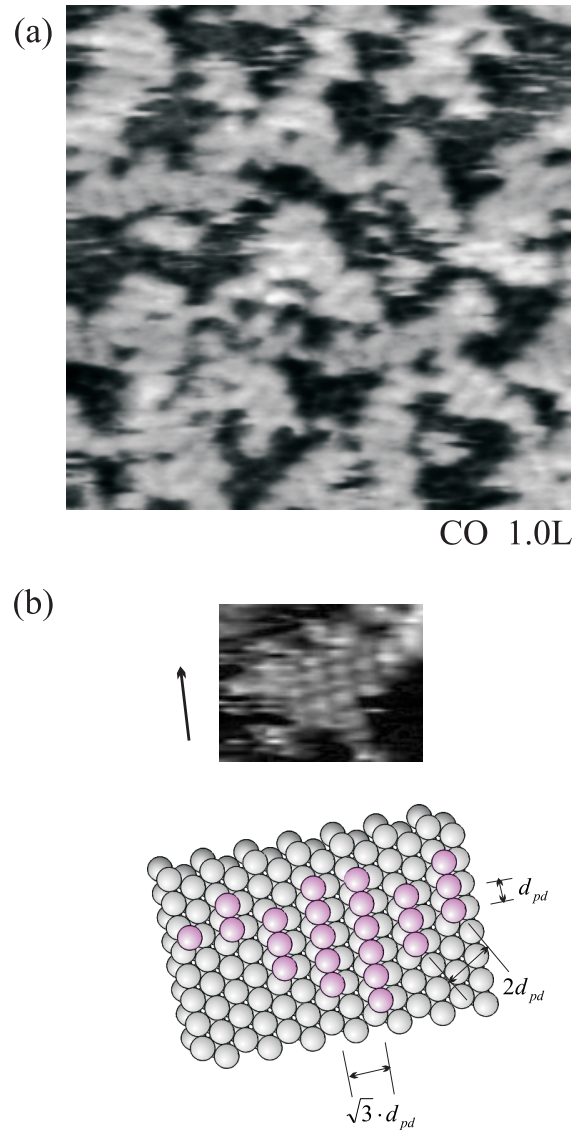


Figure 3.11: Atomically resolved (2×1) island at the maximum coverage. (a) 53 % of the entire surface is covered with (2×1) islands. $U_T = 0.4$ V, $I_T = 0.7$ nA. $T_{\text{sample}} = 180$ K. $120 \text{ \AA} \times 120 \text{ \AA}$. (b) Internal structure of a (2×1) island. White dots form the (2×1) superstructure. A model for the (2×1) structure is shown below. Note that the distance between the rows is $\sqrt{3}d_{\text{pd}}$, where d_{pd} is the distance between Pd atoms on the substrate, 2.74 \AA [40]. $U_T = 0.3$ V, $I_T = 2.2$ nA. $T_{\text{sample}} = 143$ K. $35 \text{ \AA} \times 20 \text{ \AA}$.

3.6 Dynamic analysis of the phase transition in the mixed (CO+O) adlayer on Pd(111)

All observation presented so far were made *after* the surface was exposed to given amounts of CO. In the following, dynamic observations under a partial pressure of CO will be reported.

Fig. 3.12 shows an experiment at $T_{\text{sample}} = 134$ K. A well-ordered (2×2) -O adlayer was prepared first (Fig. 3.12a). The dark dots are O atoms, and there are some empty areas in the (2×2) -O adlayer. During exposure to CO, the (2×2) -O adlayer disappears (Figs. 3.12 b–d), and a disordered structure is formed. In a second stage, small and long (2×1) patches emerge (Fig. 3.12e). White dots which constitute (2×1) islands form small patches or chains, and they are mostly connected. Then, the small (2×1) patches agglomerate to form larger (2×1) islands (Fig. 3.12f). The (2×1) islands remain stable if the surface is not exposed to further CO. If the surface is further exposed to CO, the (2×1) islands react off with adsorbing CO (not shown). The initial θ_{O} in Fig. 3.12a is 0.17, and the final θ_{O} in Fig. 3.12f is 0.18. Therefore, within experimental error, there does not occur any reaction of O atoms during the phase transition as is shown in section 3.5.3.

At a somewhat higher temperature the phase transition occurs so fast that many changes occur in one image during the scanning (Fig. 3.13). Again, a well-ordered (2×2) -O adlayer was prepared (Fig. 3.13a). Here, O atoms are white dots. In the lower part of Fig. 3.13a, the state of the tip changes (dark arrow), and O atoms appear gray and vacancies white. Then the state of the tip does not change throughout the series. Scanning in the vertical direction is continuously up and down as is indicated with a white arrow in each image. In Fig. 3.13b the adlayer begins to disappear in the upper part of the image, and small (2×1) patches emerge in the lower part of the image. The intermediate, completely disordered, mixed adlayer of O and CO is not observed here. Small (2×1) patches are still observed in the lower part of the next image (Fig. 3.13c), and they agglomerate to form larger (2×1) islands in the upper part of the image. The (2×1) islands can again be identified by their streaky structure. The agglomerated (2×1) islands finally stabilize (Fig. 3.13d). The completely disordered, mixed adlayer of O and CO exists only for a short time compared to the other stages of the phase transition. The initial θ_{O} in Fig. 3.13a is 0.16, and the final θ_{O} in Fig. 3.13d is 0.14 indicating that some amount

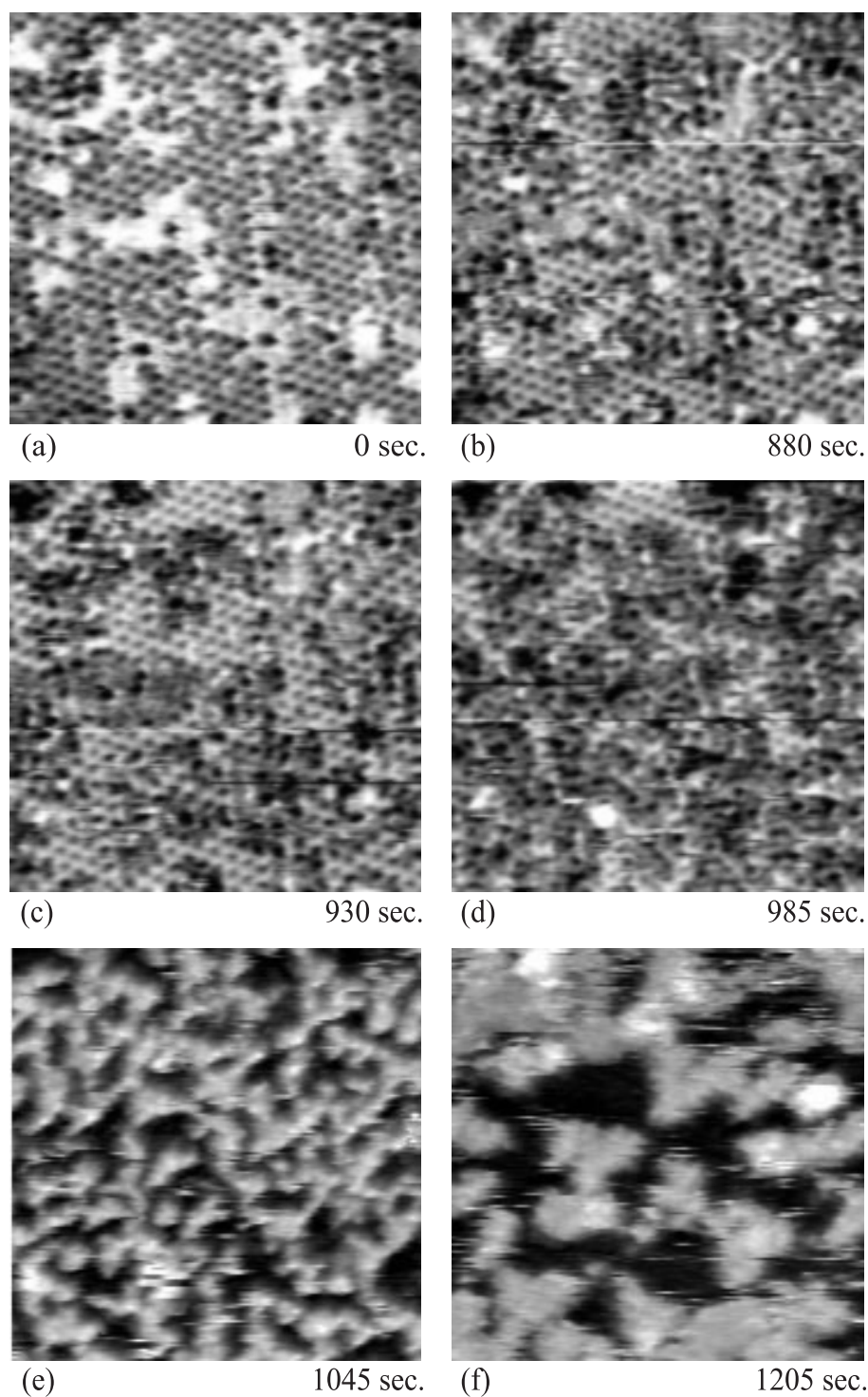


Figure 3.12: Dynamic observation of the phase transition of (CO+O) coadlayer on Pd(111). $P_{CO} = 2 \times 10^{-8}$ Torr. O atoms are imaged as dark dots. Time indicated below each image is the elapsed time since the surface was exposed to CO. The series shows the same area. (a) (2×2) -O adlayer. (b)–(d) Disintegration of the (2×2) -O adlayer. (e) Initial stage of the (2×1) island formation. (f) Agglomeration of small (2×1) patches. $U_T = 0.4$ V, $I_T = 0.7$ nA. $T_{\text{sample}} = 134$ K. $125 \text{ \AA} \times 125 \text{ \AA}$.

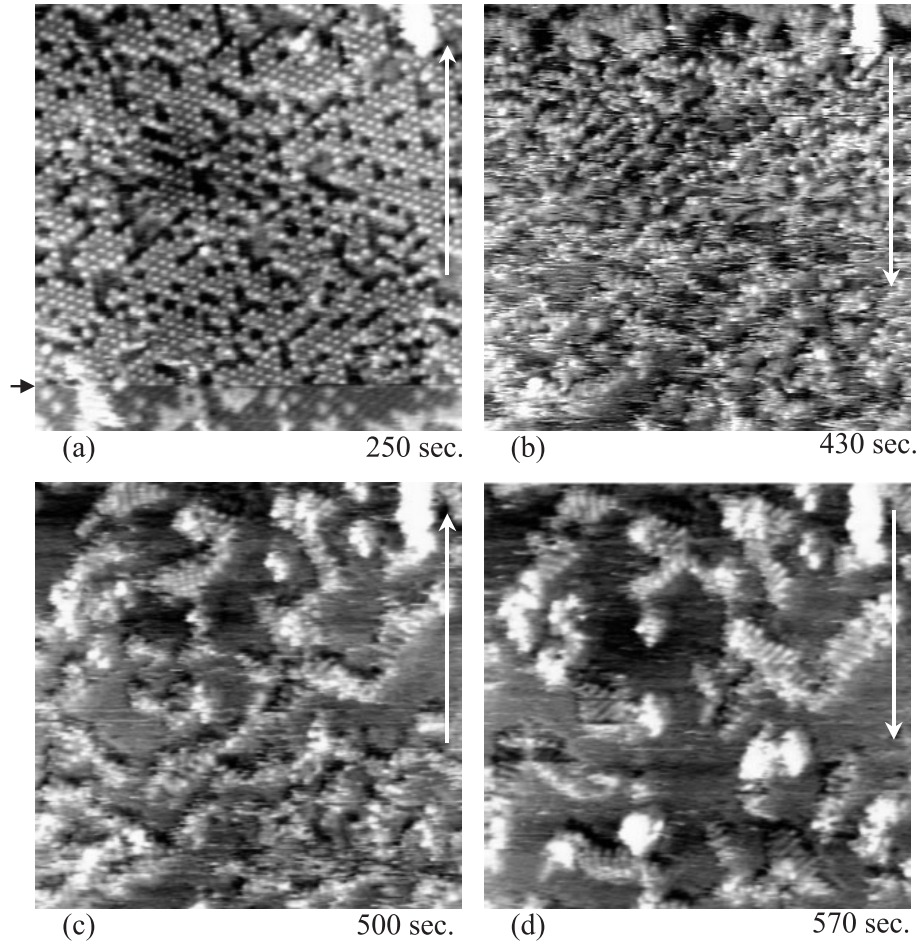


Figure 3.13: Dynamic observation of the phase transition at elevated T_{sample} . $P_{\text{CO}} = 2 \times 10^{-8}$ Torr. O atoms are imaged as white dots. Time indicated below each image is the elapsed time since the surface is exposed to CO. The series shows the same area. (a)–(d) The scan direction is shown with an arrow. $U_{\text{T}} = 0.3$ V, $I_{\text{T}} = 2.2$ nA. $T_{\text{sample}} = 143$ K. $240 \text{ \AA} \times 240 \text{ \AA}$.

of O reacts off in the series.

The features of the dynamic phase transition are almost the same as the features under static conditions except that the compression of the (2×2) -O adlayer to the $(\sqrt{3} \times \sqrt{3}) R30^\circ$ -O structure was not observed. A new observation is the initial stage of the (2×1) formation in Fig. 3.12e. The typical (2×1) islands (Fig. 3.7e) are in reality the product of the agglomeration of small (2×1) patches emerging from a disordered, mixed adlayer. This observation also shows that the shapes and positions of the agglomerated and stabilized (2×1) islands have

nothing to do with the domains of the initial (2×2) -O adlayer, because there is complete disordering and mixing of O and CO between the two states. The compression of the (2×2) -O adlayer to (2×1) islands does not occur at the positions of the initial (2×2) -O islands.

The compression of the (2×2) -O adlayer to $(\sqrt{3} \times \sqrt{3})$ R30°-O islands could not be observed in the dynamic experiments. The (2×2) order remains until the O adlayer completely disintegrates. The STM tip may play a role here or the transition may be too fast to be resolved. Another phenomenon is the longer induction time from the beginning of the CO exposure to the beginning of the phase transition than in the previous LEED experiments [40, 31]. The induction times are ~ 800 seconds in Fig. 3.12 and ~ 400 seconds in Fig. 3.13 at $P_{\text{CO}} = 2 \times 10^{-8}$ Torr. In LEED experiments, it was ~ 100 seconds at $P_{\text{CO}} = 2.5$ to 5.0×10^{-9} Torr. These long induction times are most likely due to the shadow effect of the STM tip. When the tip radius is too large, CO adsorption on the surface directly under the tip is reduced. This effect will be discussed in detail in section 3.7.

3.7 Quantitative analysis of the reaction in the mixed (CO+O) adlayer on Pd(111)

3.7.1 Evaluation procedure of the quantitative measurements

For a quantitative analysis, a series of STM images was obtained at the same area during exposure to CO. A graphic program *NIH Image 1.60/ppc* was used to determine the island coverage (θ) and also the length of the island perimeters (L). Next, the time evolution of θ was plotted. Because θ in each image represents an average value during the scanning time of the image (~ 60 seconds), each value on the time axis ($\theta(t)$) was placed at the middle point of the time for each image. The reaction rates were obtained from the slopes between $\theta(t)$ s. The time points for obtained reaction rates were placed at the middle point of the time points for the $\theta(t)$ s.

Errors in the measurements of θ or L arose from uncertain features for which it was unclear whether they belong to the islands or to contaminants or defects. Usually, contaminants or defects are not reactive and remain at their positions during the experiment. Therefore, they

do not appear in the rate measurements because they are additive constants for each image. Other ambiguities in the measurement appear as errors, where margins are mostly $< \pm 3 \%$ and at maximum $< \pm 10 \%$ of the measured quantity.

The statistical error from the finite numbers of O atoms (n) can be estimated from $n = 250$ to 300 at the beginning of the reaction, and n decreases as the reaction progresses. The statistical error, $\sim 1/\sqrt{n}$, is thus $\sim 6 \%$ at the beginning and is not problematic compared to the experimental error. It increases at the end of the reaction, lowering the validity of the measured quantity. However, because the absolute values at the end are much smaller than the values at the beginning, their absolute errors are not serious.

3.7.2 Reaction mechanism of the (2×1) structure

During the CO oxidation on Pd(111) involving the (2×1) structure, T. Matsushima et al. observed by angle resolved TDS that the product molecule, CO_2 , was highly collimated to the surface normal [40]. In these experiments, the (2×2) -O structure was exposed to CO at $T_{\text{sample}} = 190$ K and heated, leading to a CO_2 peak at 230 K. The perpendicular desorption suggested that the reaction sites are closely surrounded by O or CO, restricting the parallel motion of the desorbing CO_2 . It was thus concluded that the reaction occurs inside the (2×1) islands.

In order to minimize the tip shadow effect (section 2.4) in the quantitative STM experiments, the sharpest tip that could be prepared by the electrochemical etching was used (tip radius ~ 50 nm). Great care was taken to avoid contact with the sample during coarse approach. With such a tip, the reaction indeed showed induction times comparable to the previous LEED studies. The rates calculated in this section can therefore be taken as realistic.

Fig. 3.14 shows an experiment at $T_{\text{sample}} = 144$ K. (2×1) islands were prepared by exposing the initial (2×2) -O adlayer to 7 L CO (Fig. 3.14a). The series show the time evolution of the same area. Fig. 3.14 a–c shows the area before further exposure to CO gas, Fig. 3.14 d–f the time evolution when CO was introduced into the chamber.

Before the exposure, the islands show some mobility (circles in Fig. 3.14a, b). In particular, there are some shape changes (rhombi in Fig. 3.14a, c), and in one case an entire island disappears (squares in Fig. 3.14a, b). Such a spontaneous event suggests perturbations causing reactions at T_{sample} as low as 144 K. However, the number of islands affected by such processes is small. When the surface was exposed to

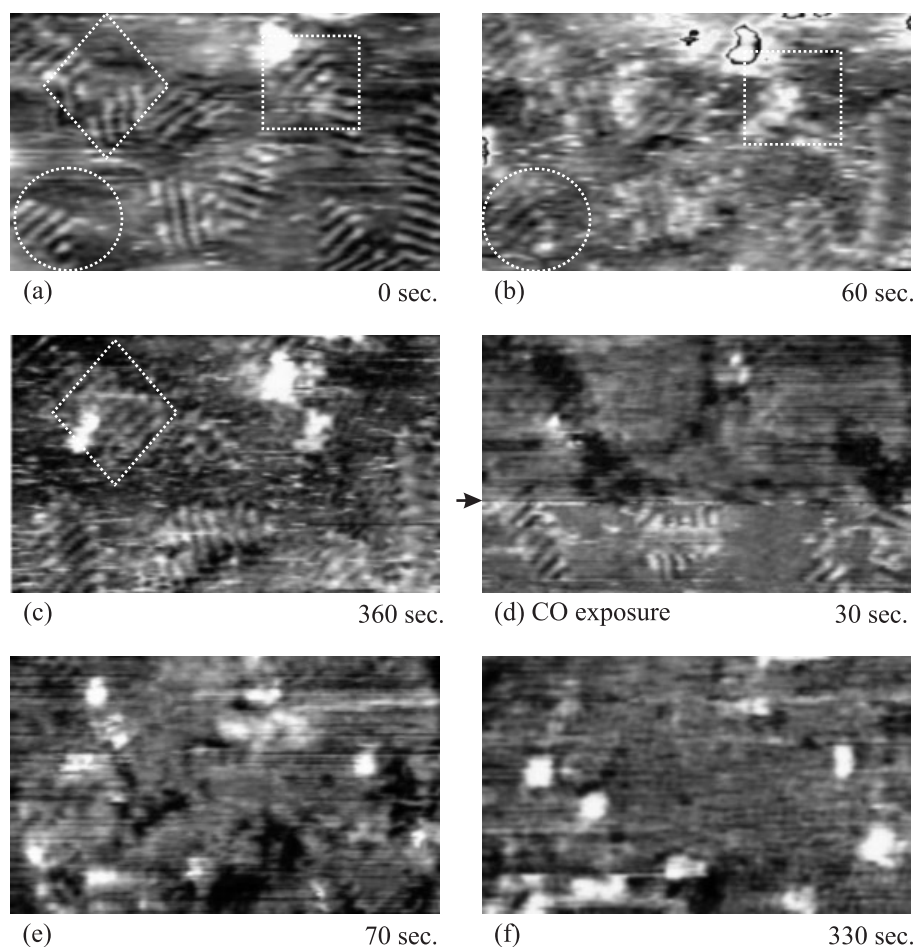


Figure 3.14: In situ observation of the reaction of (2×1) islands. $P_{\text{CO}} = 2 \times 10^{-7}$ Torr. The series shows the same area. The CO exposure begins between (c) and (d). Time indicated below images (a)–(c) is the elapsed time without exposure to CO, and below (d)–(f) during exposure to CO. Islands with alternating bright and dark rows are (2×1) islands. In (d), the state of the tip changed (indicated with an arrow), and the islands are imaged dark thereafter. $U_{\text{T}} = 0.4$ V, $I_{\text{T}} = 2.2$ nA. $T_{\text{sample}} = 144$ K. $130 \text{ \AA} \times 80 \text{ \AA}$.

CO gas, a clear reaction started. (Figs. 3.14 d–f). The progressing reaction is also reflected in the time evolution of the (2×1) coverage ($\theta_{(2 \times 1)}$) (Fig. 3.15).

In the beginning of the experiment, the (2×1) islands are imaged as alternating bright and dark rows (Fig. 3.14 a–c). The state of the tip changed shortly after the CO exposure was started (an arrow in Fig. 3.14d), after which the islands were imaged dark. The islands become

smaller and eventually disappear, and the reaction is homogeneous, i.e., all islands shrink simultaneously. Although detailed changes of the island shape could not be resolved, $\theta_{(2 \times 1)}$ and the boundary length of the islands could still be determined. Fig. 3.15 shows the time evolution of $\theta_{(2 \times 1)}$.

Fig. 3.15 clearly shows the transition from the fluctuating islands in the absence of CO gas to the fast reaction when CO was dosed at $t = 0$ second. In order to make sure that the reaction rate during exposure to CO gas is not limited by the CO adsorption rate, the rate at which CO molecules impinge on the surface must always be high. An indication that this is the case is the high density of CO between the islands that is higher than the $(\sqrt{3} \times \sqrt{3})$ R30°-CO adlayer (Fig. 3.10). In addition, experiments at a different P_{CO} were performed. We find that when P_{CO} is 2×10^{-8} Torr, one order of magnitude lower than in Fig. 3.15, the decrease of $\theta_{(2 \times 1)}$ vs time is the same as in Fig. 3.15. This observation clearly shows that the adsorption rate of CO gas does not affect the reaction rate.

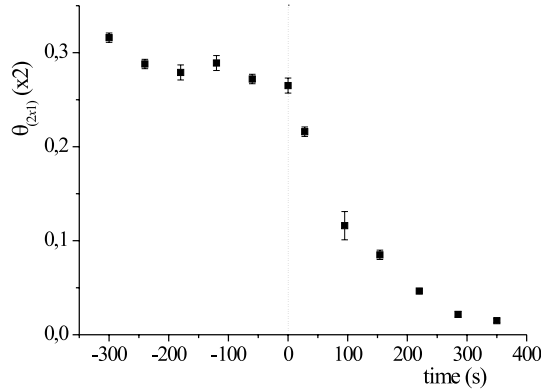


Figure 3.15: Time evolution of $\theta_{(2 \times 1)}$ from Fig. 3.14. The dotted line indicates the beginning of the CO exposure.

The kinetics for the reaction of the (2×1) phase can be generally formulated as follows.

$$-\frac{d\theta_{(2 \times 1)}}{dt} = k \cdot \theta_{(2 \times 1)}^m \cdot \theta_{\text{CO}}^n \quad (3.1)$$

As shown above, under reaction conditions there is a surplus of CO, and θ_{CO} can be considered as constant. Then Eq. (3.1) can be written

as

$$-\frac{d\theta_{(2\times 1)}}{dt} = k' \cdot \theta_{(2\times 1)}^m . \quad (3.2)$$

The reaction order m in Eq. (3.2) is obtained from a double logarithmic plot of the reaction rate vs $\theta_{(2\times 1)}$. Fig. 3.16 shows the plot from the data in Fig. 3.15 ($t > 0$). The slope of the linear fit is 1.2 ± 0.3 , representing the reaction order m with respect to $\theta_{(2\times 1)}$. The reaction rate is hence approximately proportional to the area covered by the (2×1) phase. The reaction of the (2×1) structure with a reaction order of ~ 1 was even observed at $T_{\text{sample}} = 136$ K (not shown).

The rate was furthermore tried to be correlated with the length of the island perimeters ($L_{(2\times 1)}$). In the case of the CO oxidation on Pt(111) the rate was proportional to the borders of (2×2) -O islands, indicating that the reaction only occurred at the borders between O and CO domains [3].

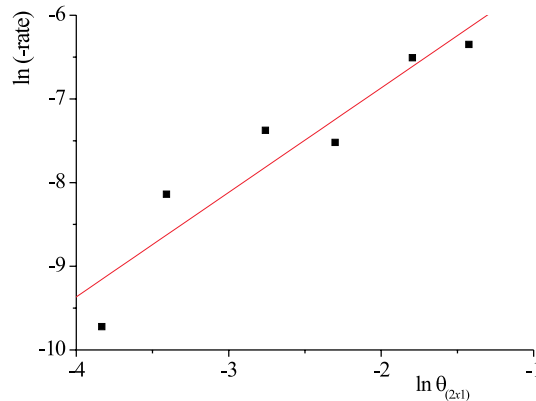


Figure 3.16: Double logarithmic plot of the reaction rate vs $\theta_{(2\times 1)}$. The slope of the linear fitting is 1.2 ± 0.3 .

For this comparison, the raw data of the reaction rates are compared with the data of the reaction rates divided by $L_{(2\times 1)}$ and with the data of the reaction rates divided by $\theta_{(2\times 1)}$. Note that the values are normalized so that the data points at $t = 320$ s have similar values. The result clearly shows different behaviors with time (Fig. 3.17). While the raw data and the $\text{rate}/L_{(2\times 1)}$ data show a pronounced decrease with time, the $\text{rate}/\theta_{(2\times 1)}$ remains constant. The difference is outside the experimental errors as shown in the graph. This analysis shows

without any assumption about the form of the kinetics that the reaction rate is better described to be proportional to $\theta_{(2 \times 1)}$, rather than to $L_{(2 \times 1)}$. From this analysis it is concluded that the reaction of the (2×1) island is actually not described by a simple reaction at the island perimeters. This reaction is therefore different from the CO oxidation on Pt(111) [3], which occurs at the perimeters of O islands and displays the expected proportionality of the rate to $L_{(2 \times 2)_O}$ and a reaction order of 0.5.

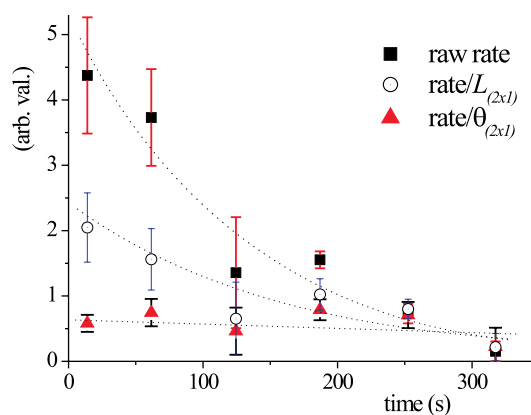


Figure 3.17: Time evolution of raw data of the reaction rate, $\text{rate}/L_{(2 \times 1)}$, and $\text{rate}/\theta_{(2 \times 1)}$. Dotted lines are eye guides.

Models for surface reactions usually assume a random distribution of reactants on the surface (Langmuir gas), the most simple situation one can assume. One typical example of deviation from such a simple situation is the formation of islands of reactants on the surface. There are many experimental examples showing that island formation affects macroscopic kinetics [57]. Detailed theoretical studies about the effect of island formation on the kinetics show that a mean field approximation, which is mathematically equivalent to the assumption of a random distribution of reactants, is often too simple [58]. Usually it is assumed that a reaction order of 0.5 implies islands of adsorbates in the reaction [59]. This assumption is based on the fact that the island perimeter (L) is proportional to the square root of the area of the island ($\sqrt{\theta}$) for islands with a compact shape. However, for the reaction of the (2×1) structure on Pd(111) this is not the case. Although there are islands of adsorbates during the reaction, the reaction order with respect to

$\theta_{(2 \times 1)}$ is ~ 1 .

How can this surprising result be explained? In section 3.3, it was shown that the (2×2) -O adlayer is formed due to the *attractive* interactions between O atoms. In section 3.5.3, we found that O atoms exist only in the (2×1) island and that they form the (2×1) superstructure. In the (2×1) islands the O atoms interact *repulsively* with each other because of the short distances (Fig. 3.11b). The nearest neighbor distance is d_{pd} , the next nearest neighbor distance is $\sqrt{3}d_{\text{pd}}$, both of which are repulsive because the related structures do not form spontaneously. Therefore, the atoms are much more weakly bound to the substrate and much more reactive than the O atoms in the (2×2) -O adlayer. Note that the increase of the reactivity enables the reaction only at the most compressed phase ((2×1) phase), not at the $(\sqrt{3} \times \sqrt{3})$ R30°-O phase. O atoms in the $(\sqrt{3} \times \sqrt{3})$ R30°-O phase are not reactive (section 3.5.3), where the nearest neighbor distance is $\sqrt{3}d_{\text{pd}}$. Furthermore, CO molecules can be pushed into the islands between the O atom rows, or CO molecules from the gas phase may directly adsorb between the rows. On Pt(111) similar interstitial CO molecules exist within the (2×2) -O structure. However, the binding energy of these molecules is almost the same as for CO molecules between the islands [60], and the activation energy for a reaction of these interstitial molecules is high. Therefore, only CO molecules at the island perimeters, which occupy unfavorable sites, are reactive. For Pd(111), interstitial CO molecules in the (2×1) structure are energetically very unfavorable [31]. The activation energy must therefore be small, which explains the very low onset temperature for the reaction. Furthermore, all O atoms have the same reaction probability, irrespective of their positions at the island perimeters or in the interior of the islands. However, an equal reaction probability of all particles is precisely the condition underlying the reaction kinetics of a Langmuir gas, which predicts a reaction order of 1. Both characteristics of the reaction on Pd(111) that are different from the Pt(111) case can therefore be traced back to the behavior of the O atoms, which can form denser structures on Pd(111).

We can estimate an effective activation energy for the reaction E_{reac}^* . With $m \sim 1$ the integration of Eq. (3.2) yields

$$\theta_{(2 \times 1)} = \theta_{(2 \times 1)}^0 \cdot e^{-k't}, \quad (3.3)$$

where $\theta_{(2 \times 1)}^0$ is the coverage of the (2×1) islands at $t = 0$ in Fig. 3.15. As expected from Eq. 3.3, a double logarithmic plot of $\theta_{(2 \times 1)}/\theta_{(2 \times 1)}^0$ vs $e^{-k't}$ indeed falls on a straight line fit, and $k' = (7.8 \pm 0.4) \times 10^{-3} \text{ s}^{-1}$ is

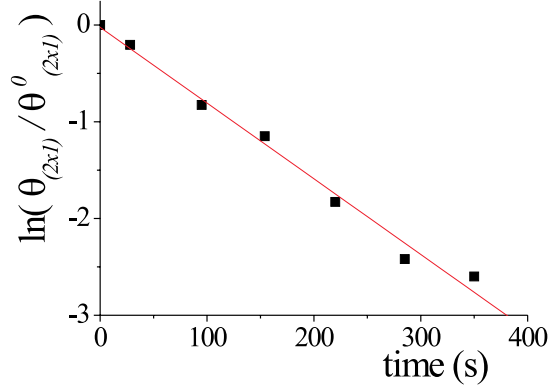


Figure 3.18: Double logarithmic plot of $\theta_{(2 \times 1)} / \theta_{(2 \times 1)}^0$ vs. $e^{-k't}$. The slope of a linear fit of the data is $(7.8 \pm 0.4) \times 10^{-3} \text{s}^{-1}$.

obtained from the slope of the line (Fig. 3.18). Assuming an Arrhenius behavior, the pseudo first-order reaction constant k' can be written as

$$k' = A \cdot k_o \cdot \exp(-E_{\text{reac}}^* / k_B T), \quad (3.4)$$

where A is a constant between $0 \sim 1$ because it contains θ_{CO} (Eq. (3.2)). Then, under the assumption of a preexponential factor k_o of 10^{13}s^{-1} and $A = 0.5$, E_{reac}^* is 0.41 eV (Table 3.2).

Table 3.2: Estimated activation energy E_{reac}^* for the reaction of the (2×1) structure. For comparison with values from the literature, see text

Substrate	$k_o (\text{s}^{-1})$	$E_{\text{reac}}^* (\text{eV})$
Pd(111)	10^{13} (assumed)	0.41
(our results)	5×10^7 (assumed)	0.26
Pd(111) [38] T > 300 K		0.61 ± 0.08
Pt(111) [3, 60]	5×10^7	0.49

For CO oxidation above room temperature on an O-precovered Pd(111), T. Engel et al. measured $E_{\text{reac}}^* = 1.08 \text{ eV}$ at $\theta_{\text{CO}} \leq 0.02$ and $\sim 0.61 \text{ eV}$ at $\theta_{\text{CO}} = 0.33$ by molecular beam experiments [38] (Table 3.2). C. Zhang et al. calculated the reaction barriers by DFT [61], and they obtained $E_{\text{reac}}^* = 0.89 - 0.93 \text{ eV}$ for the reaction at $\theta_{\text{O}} = 0.25$. This value corresponds to the measured E_{reac}^* at $\theta_{\text{CO}} \leq 0.02$ (1.08 eV)

by T. Engel et al., because O forms islands of the (2×2) structure with a local coverage θ_{O} of 0.25. The reaction at $\theta_{\text{CO}} = 0.33$ is thought to occur between disordered CO molecules and O atoms in or at the periphery of $(\sqrt{3} \times \sqrt{3})$ R30°-O islands [23]. The lower E_{reac}^* for this reaction, 0.61 eV, shows the influence of the repulsive interaction between the O atoms. From these considerations it is expected that E_{reac}^* for the reaction of the (2×1) structure should be even lower than 0.61 eV, in agreement with the estimated value of 0.41 eV.

T. Matsushima et al. measured $E_{\text{reac}}^* = 1.3$ eV for the reaction between CO and O atoms in or at the periphery of $(\sqrt{3} \times \sqrt{3})$ R30°-O islands, and 1.0 eV for the reaction between CO and O atoms in or at the periphery of the (2×1) islands by preparing the states at $T = 100$ K and doing TDS [40]. Although these absolute values are much larger than the values by T. Engel et al., they show the same trend with coverage. Because of the varying temperature in a TDS experiment, the absolute numbers are less reliable here.

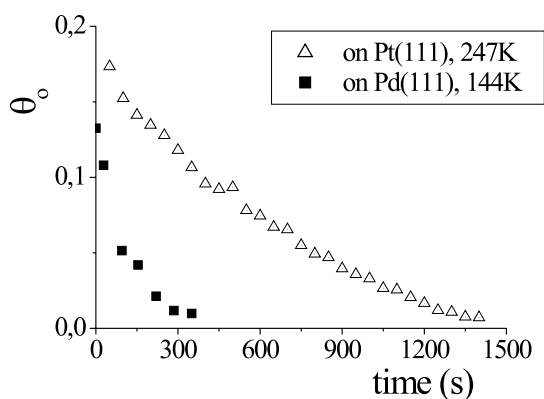


Figure 3.19: Comparison of CO oxidation on Pd(111) and Pt(111). P_{CO} was 5×10^{-8} Torr on Pt(111) and 2×10^{-7} Torr on Pd(111). Note the temperature difference. Data from Pt(111) are from [4].

For the CO oxidation on Pt(111), J. Wintterlin et al. measured $E_{\text{reac}}^* = 0.49$ eV in their STM study [3, 60] (Table 3.2). It is reasonable that the present result for Pd(111) is lower than this value, considering that CO oxidation on Pt(111) still occurs very slowly at $T \sim 250$ K, i.e., about 100 K higher than the onset temperature on Pd(111) (Fig. 3.19). This result agrees well with the compression effects on Pd(111) and the resulting lower adsorption energies of O atoms and CO molecules. For

CO oxidation on Pt(111) a preexponential factor of $k_o = 5 \times 10^7 \text{ s}^{-1}$ was also measured [60]. This value is very low considering the usual value of 10^{13} s^{-1} . If we use this value for the Pd(111) data, E_{reac}^* becomes 0.26 eV. This low value is also not surprising considering that the reaction occurs with such high rates at low temperatures.

Such an extremely high reactivity in the case of the Pd(111) surface is due to the compression of the (2×2) -O adlayer by CO. The (2×1) phase is highly compressed, and the O atoms in the islands feel strong repulsive interactions. Then the question is why there occurs such a phase transition on Pd(111), but not on Pt(111)? On both surfaces, there are initially attractive interactions between the O atoms, leading to a (2×2) superstructure. One possible explanation was given by A. Seitsonen et al. on the basis of DFT calculations [31]. They found that it only costs 0.10 eV/atom to compress the (2×2) -O structure into a $(\sqrt{3} \times \sqrt{3})$ R30°-O structure, while for CO the energy gain is 0.67 eV/molecule when it adsorbs on the bare Pd(111) surface compared to adsorption on sites within the (2×2) -O structure. Therefore, compression of the (2×2) -O structure and formation of separate CO domains is energetically favorable over the mixed (2×2) -(O+CO) coadsorption. The compression from the $(\sqrt{3} \times \sqrt{3})$ R30°-O structure to the (2×1) structure is very likely to occur for the same reason. According to those calculations, the unfavorable adsorption in the (2×2) -O phase is due to the fact that the only available adsorption site in this structure is on top of a Pd atom (on the three-fold site all Pd atoms are bound to O atoms). However, for Pd(111) the on-top site is 0.5 eV less stable than fcc sites, which are occupied by CO on the empty surface. On the other hand, the adsorption energies of CO on various adsorption sites of Pt(111) are very similar to each other [56]. On other transition metal surfaces, such as Ru(0001) and Rh(111), the situation is not different [31].

3.8 The (CO+O) adlayer on Pd(111) at $T < 130$ K

As mentioned in section 3.5, the phase transitions of the (CO+O) coadlayer occur at $130 \text{ K} < T_{\text{sample}} < 230 \text{ K}$. Below $T_{\text{sample}} < 130 \text{ K}$, the LEED pattern did not give clear evidence for a phase transition [40]. STM experiments below 130 K also show a different behavior of the system than at higher temperatures.

Fig. 3.20 shows (2×2) -O islands on Pd(111) under a partial pressure

of CO at $T_{\text{sample}} = 101$ K. O atoms are imaged as dark dots forming a (2×2) superstructure (Fig. 3.20a). The O islands are surrounded by bare substrate. O atoms at this temperature are immobile before exposure to CO and almost immobile in the presence of CO.

When CO is dosed, brighter dots appear, mainly at the boundaries of the (2×2) -O islands (Figs. 3.20b, c). This phenomenon can be explained as follows. As the CO concentration between the O islands increases, repulsive forces build up. CO molecules at the borders of the O islands are pushed to adsorption sites that are different from those occupied in the pure CO phase, where they are imaged differently. The apparent height of CO molecules in the STM image is known to vary according to adsorption sites [62].

When the density of CO in the CO phase reaches a critical value, CO begins to adsorb *inside* the O islands (Fig. 3.20d). In this image, a CO molecule in an O island is imaged as a very bright dot. In addition, there are some dashes inside the O island that can be interpreted as CO molecules which change adsorption sites during the scanning. In a later stage, CO remains stable inside the O island as seen in Fig. 3.20e. These processes are different from the phase transitions at $T_{\text{sample}} > 130$ K because the CO molecules inside the O island form a (2×2) superstructure, suggesting that there remains some part of the (2×2) -O structure. It is unclear whether some reaction between CO and O occurs in Figs. 3.20 e–h. The O islands shrink, but this does not necessarily mean that O atoms react off because O atoms can still exist between CO molecules. Considering that the reaction occurs only in the compressed (2×1) phase at $T_{\text{sample}} > 130$ K, it is very likely that a reaction does not occur at these temperatures without the compression. This phenomenon persists up to $T_{\text{sample}} = 130$ K, confirming the LEED result [40].

At even lower temperature, CO adsorbed on the (2×2) -O adlayer forms a mixed (2×2) superstructure with O. Fig. 3.21 shows the development of this phase at $T_{\text{sample}} = 60$ K. Such a mixed coadlayer is the usual observation on other metal surfaces [42]. That it occurs on Pd(111) only at such low temperatures suggests that the repulsive interactions between CO and O on Pd(111) are much stronger than on other metal surfaces.

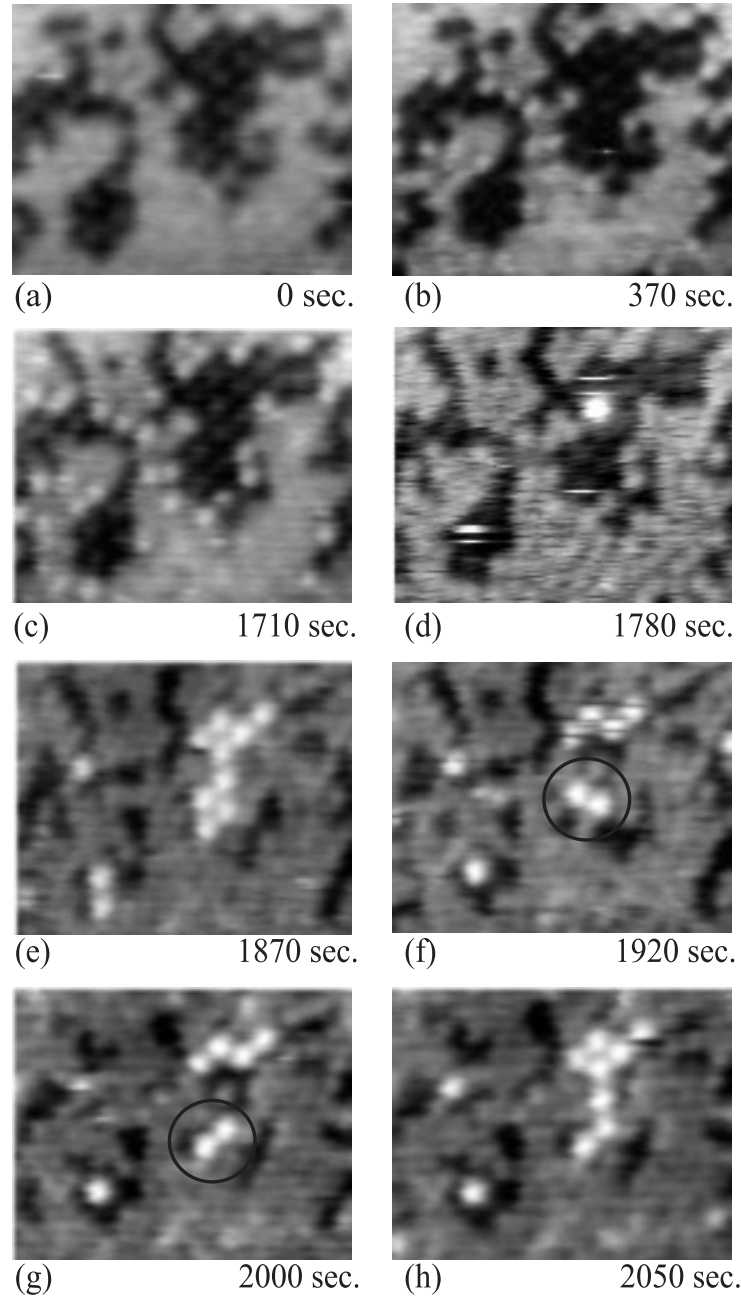


Figure 3.20: CO adsorption on the O covered Pd(111) at $T_{\text{sample}} < 130$ K. $P_{\text{CO}} = 5 \times 10^{-9}$ Torr. The series shows the same area. Dark dots are O atoms. Time indicated below the image is the elapsed time since the surface is exposed to CO. (a) O atoms form (2×2) islands. (b), (c) Adsorbed CO along the boundaries of the islands are imaged brighter. (d) CO begins to adsorb inside the (2×2) -O islands. One CO molecule is imaged as a white dot in a (2×2) -O island. (e) CO adsorbed inside the (2×2) -O islands forms also a (2×2) superstructure. (f)–(h) CO adsorbed inside the (2×2) -O islands shows some mobility. $U_{\text{T}} = 0.4$ V, $I_{\text{T}} = 0.7$ nA. $T_{\text{sample}} = 101$ K. $50 \text{ \AA} \times 40 \text{ \AA}$.

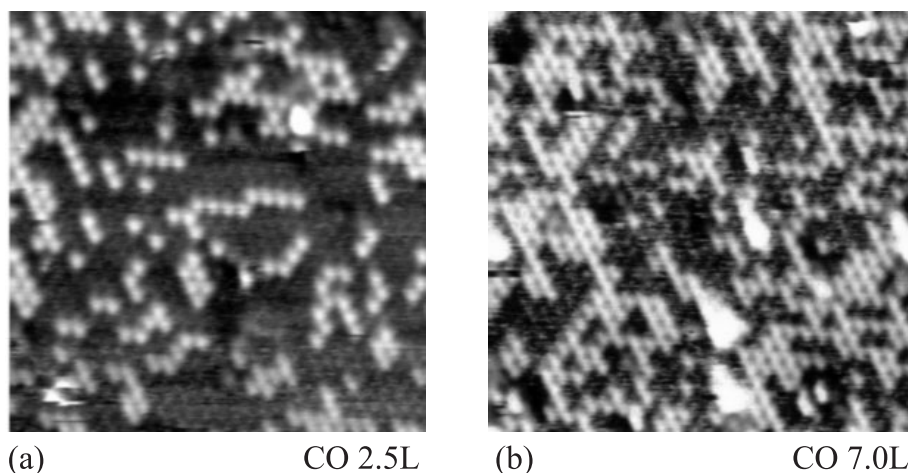


Figure 3.21: Mixed (2×2) -(CO+O) coadlayer at low temperature. The images do not show the same area. White dots are CO molecules. $U_T = 0.5$ V, $I_T = 2.2$ nA. $T_{\text{sample}} = 60$ K. $110 \text{ \AA} \times 110 \text{ \AA}$.

3.9 Summary

STM was used to investigate microscopic features of O/Pd(111), CO/Pd(111), and (CO+O)/Pd(111) and to obtain insight into the mechanisms of the reaction between CO and O. O atoms on Pd(111) at low coverages ($\theta_O < 0.25$) interact attractively with each other and form (2×2) islands before they build up the (2×2) adlayer at $\theta_O = 0.25$. The atoms become mobile at $T_{\text{sample}} > 135$ K. An activation energy for the diffusion $E_{\text{diff}}^* = 0.54 \pm 0.08$ eV was obtained, and the preexponential factor for the hopping $\Gamma_o = 10^{16 \pm 3} \text{ s}^{-1}$ for $0.4 < \theta_O / \theta_{O\text{-max}} < 0.6$ (see Table below). CO molecules on Pd(111) at low coverages ($\theta_{\text{CO}} < 0.33$) interact attractively with each other and form $(\sqrt{3} \times \sqrt{3})$ R30° islands before they build up the $(\sqrt{3} \times \sqrt{3})$ R30° adlayer at $\theta_{\text{CO}} = 0.33$. They display a high mobility even at $T_{\text{sample}} = 60$ K. An E_{diff}^* of 0.15 eV was estimated for CO (assuming the Γ_o as 10^{13} s^{-1} for $\theta_{\text{CO}} \sim 0$) (see Table below).

Adsorption of CO on the (2×2) -O adlayer at $T_{\text{sample}} > 130$ K causes a phase transition of the adlayer to first form a $(\sqrt{3} \times \sqrt{3})$ R30°-O, then a (2×1) structure. CO molecules first occupy sites in the (2×2) -O superstructure. With increasing coverage the repulsive interactions between adsorbed CO molecules and O atoms cause compression of the

Diffusion	$\Gamma_o(\text{s}^{-1})$	E_{diff}^* (eV)
O	$10^{16\pm3}$	0.54 ± 0.08
CO	10^{13} (assumed)	~ 0.15
O between ($\sqrt{3} \times \sqrt{3}$) R30°-CO islands	10^{16} (assumed)	$0.47 \sim 0.50$
Reaction	$k_o(\text{s}^{-1})$	E_{reac}^* (eV)
CO + O of (2×1) islands	10^{13} (assumed) 5×10^7 (assumed)	0.41 0.26

(2×2)-O adlayer into ($\sqrt{3} \times \sqrt{3}$) R30° islands. Simultaneously, adsorbing CO molecules form small ($\sqrt{3} \times \sqrt{3}$) R30° areas on the emptied space. The repulsive interaction is not strong enough to drive all individual O atoms out of the CO domains, and the ($\sqrt{3} \times \sqrt{3}$) R30°-CO areas do not merge to form larger islands. The mobility of the O atoms in the CO domains is 10 to 10^2 higher than the mobility of O atoms without CO. The individual O atoms are less strongly bonded to the substrate due to the repulsive force from neighboring CO molecules. The E_{diff}^* of the O atom is estimated to be 10 to 20 % lower than the E_{diff}^* of the O atom without CO (see Table above). With further exposure to CO, the ($\sqrt{3} \times \sqrt{3}$) R30°-O islands become smaller, and disordered domains with individual O atoms and small ($\sqrt{3} \times \sqrt{3}$) R30°-CO islands become larger. At some point, the (CO+O) adlayer is almost completely disordered. With further exposure to CO, many small patches with a (2×1) superstructure emerge in this mixed adlayer. The (2×1) patches agglomerate into larger (2×1) islands, leading to a stabilization. O atoms exist only in the islands, and they form (2×1) superstructure in the islands. The density of O atoms in the (2×1) islands is thus twice that of the (2×2)-O adlayer. Outside the (2×1) islands, CO molecules form a $c(4 \times 2)$ superstructure, but they are not globally ordered. During the phase transition, practically no reaction occurs between O and CO.

(2×1) islands are highly reactive, and they sometimes react off spontaneously. When the surface in this state is exposed to CO gas, the (2×1) islands completely react off at temperatures as low as 136 K. Quantitative analysis of the time dependence of the reaction reveals that the reaction rate is proportional to the area of the islands, rather than to the length of the boundaries of the islands. The reaction order is ~ 1 with respect to $\theta_{(2 \times 1)}$. The STM data do not allow discriminating between (2×1) structure models with only O atoms in the structure and those assuming a (CO+O) mixed composition, but the analysis

was based on the former model. The reaction order suggests that all O atoms have the same reaction probability, consistent with a reaction in the interior of the (2×1) structure. The result contrasts the same reaction on Pt(111), where the reaction order was 0.5 and the reaction was limited to the perimeter sites of (2×2) -O islands. It is suggested that this difference is caused by the compression of the O adlayer by CO for Pd(111), which does not occur on Pt(111). The compression leads to repulsive interactions between the O atoms and thus, to a weaker bonding and higher reactivity. Furthermore, there are no favorable CO adsorption sites in the compressed phases. Therefore, CO molecules impinging from the gas phase on these areas, or being pushed onto the quite small (2×1) islands from the high density CO areas, must be very reactive. In contrast to Pt(111), reactive configurations do therefore not only occur at the island perimeters, but homogeneously across the interior of the islands. E_{reac}^* is estimated to be 0.41 eV under the assumption of $k_o = 10^{13} \text{ s}^{-1}$, and 0.26 eV for $k_o = 5 \times 10^7 \text{ s}^{-1}$, the value for Pt(111) (see Table above). These values are reasonable considering the previous macroscopic studies and the fact that it is lower than E_{reac}^* for the CO oxidation on Pt(111), which was 0.49 eV.

Adsorption of CO on the (2×2) -O adlayer at $T_{\text{sample}} < 130 \text{ K}$ does no longer cause any phase transitions. CO molecules at the borders of (2×2) -O islands occupy adsorption sites different from those in the CO domains, and CO eventually adsorbs in the (2×2) -O islands. CO molecules in the (2×2) -O also form a (2×2) superstructure.

Chapter 4

CO oxidation on $\text{RuO}_2(110)$ grown on $\text{Ru}(0001)$

4.1 Introduction to the oxide film $\text{RuO}_2(110)$ grown on $\text{Ru}(0001)$

Platinum(Pt)-group metals (Pt, Pd, Ru, Rh, and Ir) are efficient catalysts for CO oxidation under high pressure conditions similar to those for industrial catalysts [63]. Among these, Ru is the most efficient one [64, 65]. However, while the other Pt-group metals are also efficient under UHV conditions, Ru is a very poor catalyst in UHV [66, 67]. This peculiar property of Ru is a representative example of the so called ‘pressure gap’ problem in the study of heterogeneous catalysts [68].

The reason why Ru is a poor catalyst under UHV could be explained relatively easily. At low temperatures (~ 300 K), the saturation coverage (θ) of O_2 on $\text{Ru}(0001)$ surface is 0.5. Dissociatively chemisorbed O_2 forms an ordered (2×1) superstructure [69]. At this coverage, bonding between metal surface and oxygen is so strong that the activation barrier between O and CO for the reaction on the surface is too high [70].

On the other hand, the high catalytic reactivity of Ru under high pressure conditions has escaped any explanation until very recently. C. H. F. Peden et al. suggested from their high pressure experiments (> 1 atm) that the high catalytic reactivity might be due to an O phase on the $\text{Ru}(0001)$ with $\theta \sim 1$ [71, 72]. They found that the reaction rates were the highest at high O coverages with almost no CO molecules on the surface, whereas for other platinum-group metals the rates were the highest when the O coverage was as high as the CO

coverage [73, 74]. It was speculated that under high pressure conditions O atoms are still chemisorbed on Ru(0001) while the other Pt-group metal surfaces begin to be oxidized and hence become deactivated [73]. A few years later, C. Stampfl et al. found from their DFT calculation that the ordered O adlayer with $\theta = 1$ is thermodynamically stable at room temperature [75]. Indeed, the (1×1) -O adlayer on Ru(0001) was found experimentally with LEED at room temperature [76]. This phase was prepared by exposing (2×1) -O/Ru(0001) to NO₂ gas at an elevated temperature of 600 K. The maximum coverage of $\theta = 0.5$ found in previous investigation was therefore caused by kinetic limitations. Because the O atoms in the (1×1) -O adlayer are much weaker bonded¹ to the metal surface, this phase was believed to cause Ru to be highly reactive under high pressure conditions [76].

Meanwhile, A. Böttcher et al. found that while CO/CO₂ conversion rates are lower than 10^{-4} when the uptake of oxygen on the surface is less than 3 ML, the rate increases by almost two orders of magnitude when the oxygen coverage is higher than 3 ML [74, 77]. They exposed a Ru(0001) surface to several 10^6 L of oxygen while varying the sample temperature between 300 ~ 900 K. With increasing sample temperature, the uptake of oxygen increased up to 20 ML.

Soon after this discovery, H. Over et al. found that a new superstructure appears on Ru(0001) under the conditions in [74]. With the help of LEED, DFT, and STM, a structure model was proposed [9]. The superstructure turned out to be an epitaxially grown oxide film, and the stoichiometry of the oxide surface is RuO₂(110) (Fig. 4.1). The high reactivity is attributed to the existence of ‘coordinately unsaturated sites’ (cus) [78] on the oxide surface.

RuO₂-oxide formation on the Ru surface at high temperatures and under high pressures of oxygen had been known from FIM studies for quite some time [79, 80]. The main interest in these studies was, however, not in the oxide formation on the metal surface itself, but in the volatile RuO₃ and RuO₄ formation which reduces the metal weight during catalytic reactions [81]. The RuO₂(110) surface was also studied before, but as an electrode surface [82].

The discovery of H. Over et al. is very exciting because the RuO₂(110)/Ru(0001) system forms under conditions similar to those of technical processes, but nonetheless allows studies at a fundamental level thanks to the metallic nature of RuO₂ [10, 82, 83, 84] and to the single crystal form of the oxide film under UHV. Of course, intensive studies have been

¹ 0.8 eV less than O atoms in the (2×2) -O phase.

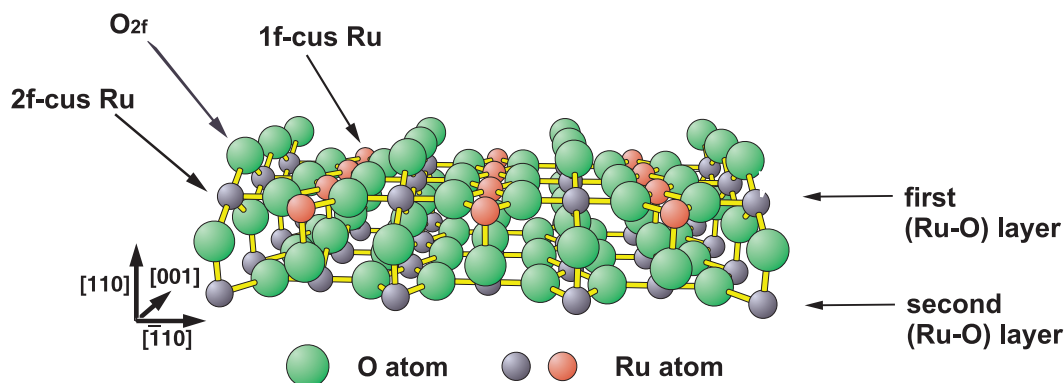


Figure 4.1: Stick-and-ball model of the $\text{RuO}_2(110)$ surface. Nomenclature for various species are explained in section 4.5.

conducted to characterize the oxide film itself and to investigate chemical properties of the film with standard surface science tools, e.g. LEED [28, 85, 86, 87], HREELS [86, 88, 89, 90], XPS [91, 92], PEEM [93, 94], STM [95, 96], and TDS [97, 98]. Theoretical studies have also been intensive [99, 100, 101, 102].

These studies established adsorption and reaction models of CO and O_2 on the oxide surface mostly based on *macroscopic* results. The established models can be summarized as the Mars-van Krevelen model [103]. In this reaction model, oxygen atoms on the oxide surface react with adsorbing reactants (CO), so that the oxide surface becomes reduced. The oxide surface is restored by oxygen atoms from dissociatively adsorbing O_2 [9, 104].

Although this model appears reasonable, there is so far no *microscopic* investigation that might give more insight into the reaction mechanism. For the CO oxidation on $\text{RuO}_2(110)$, there is so far no experimental study about the *kinetics* and the *mechanisms*. What is the reaction order of the reaction between CO and O on the oxide surface? Does the reaction occur statistically or not? How mobile are the adsorbed CO molecules and O atoms, and do the mobilities affect the reaction mechanisms?

Furthermore, there are no microscopic studies about the formation of the oxide film on $\text{Ru}(0001)$. There exist macro- to mesoscopic studies about oxide formation on $\text{Ru}(0001)$ surface. W. Mitchell et al. studied the initial stages of oxidation of $\text{Ru}(0001)$ surface with TDS, LEED, and HREELS. They proposed that a suboxide layer (RuO_x) exists as a transition layer between the substrate and the full oxide film (RuO_2)

[81]. After the discovery of RuO₂(110) film, A. Böttcher et al. monitored the initial oxidation stages of Ru(0001) on a mesoscopic scale with PEEM [93, 94]. They first observed nuclei or grains of oxide ($< 2 \mu\text{m}$), then an expansion of the nuclei as long strips along the main crystallographic directions of Ru(0001). Meanwhile, theoretical works predicted an interesting formation mechanism of the oxide film [101, 105]. K. Reuter et al. found that, when the (1 \times 1)-O/Ru(0001) adlayer (oxygen uptake 1 ML) is further exposed to O₂, the incorporation of more O atoms beneath the uppermost Ru layer (subsurface oxygen) is still exothermic up to total oxygen uptake of 2 ML. The subsurface oxygens were predicted to accumulate into dense two-dimensional islands with a local (1 \times 1) superstructure. The uppermost Ru layer is thus sandwiched between two dense O layers. This O-Ru-O trilayer then separates from the bulk and unfolds into the more open RuO₂(110) structure.

In this chapter, I first present the mesoscopic and microscopic morphologies of the oxide film under various preparation conditions observed with STM. Boundaries of the oxide film and the Ru(0001) surface in their proximity are also discussed. Then I present our STM studies of CO adsorption, O₂ adsorption, and the reaction between CO molecules and O atoms on the oxide surface on the atomic scale, which provide direct verification of the established models and identify unknown or unclear physical and chemical processes on the surface. Then I present the first experimental study of the reaction kinetics and the reaction mechanism between O atoms and CO molecules on the oxide surface by *in situ* observation of the reactions. Finally, I present observations of the reaction under steady-state conditions, where the oxide surface is exposed to CO and O₂ gas simultaneously. All measurements were done at room temperature.

4.2 Preparation of RuO₂(110)/Ru(0001)

Before preparation of the oxide film, the Ru(0001) sample was cleaned by Ar⁺ sputtering ($P_{\text{Ar}} = 1 \times 10^{-5}$ Torr, 1 keV, ion current $\sim 1 \mu\text{A}$), ~ 10 cycles of oxidation with 10 L O₂ at ~ 600 K to remove carbon contaminants, and flashing the sample up to 1300 K [27]. The cleanliness of the surface was checked with STM.

The standard method to obtain the oxide film on Ru(0001) is exposing the surface to $6 \times 10^4 \sim 6 \times 10^6$ L of O₂ gas at sample temperatures between 600 K and 900 K [9, 89, 90, 93, 94, 98]. 900 K is at the onset

of the oxygen peak from the evaporating RuO₂(110) oxide film in TDS (~ 1050 K) [86]. Therefore, 900 K is almost the highest temperature where the oxide can be formed.

We prepared the oxide film by exposing Ru(0001) surface with either 2×10^5 L or 1×10^6 L of oxygen at sample temperatures between 650 K and 900 K. The oxygen pressure was either 1×10^{-4} or 1×10^{-3} Torr, and the exposure time was 2000 or 1000 seconds, respectively. In order to achieve 1×10^{-3} Torr of oxygen in the UHV chamber, a gas shower system was installed with a microcapillary array, whose details are described in section 2.3. When the sample surface is brought to the shower system as close as 1 mm, the partial pressure of oxygen directly at the sample surface is about 100 times higher than in the chamber [30].

After preparing the oxide film, the growth of the oxide film was checked with LEED [28]. With 2×10^5 L of oxygen, both the pattern of the oxide and the (1×1) pattern of the substrate were observed, with 1×10^6 L of oxygen only the pattern of the oxide. With 1×10^6 L the oxide film was not necessarily thicker than with 2×10^5 L, but it covered the surface more completely [30].

Once the oxide film is grown, it remains stable until it is flashed off at temperatures higher than 1000 K [86]. Wider oxide terraces were obtained by flashing to lower temperatures (800 \sim 950 K). However, the higher the flashing temperature, the smaller the remaining oxide patches, making it more difficult to find oxide regions suitable for STM studies.

4.3 Mesoscopic morphology of RuO₂(110)/Ru(0001)

4.3.1 Effect of preparation temperature on the morphology of the oxide film

Fig. 4.2 shows the mesoscopic morphology of the oxide film at increasing temperatures during the preparation. Generally, the oxide layer grows anisotropically in one of three preferential directions according to the Ru(0001) substrate. The anisotropy becomes more obvious with increasing preparation temperature (T_{prep}). One explicit relation between the growth direction of the oxide film and the symmetry of the substrate is shown in Fig. 4.7. The shape of step edges and the width of the oxide layers vary depending on T_{prep} . In general, the morphology of epitaxially grown films is determined thermodynamically from sur-

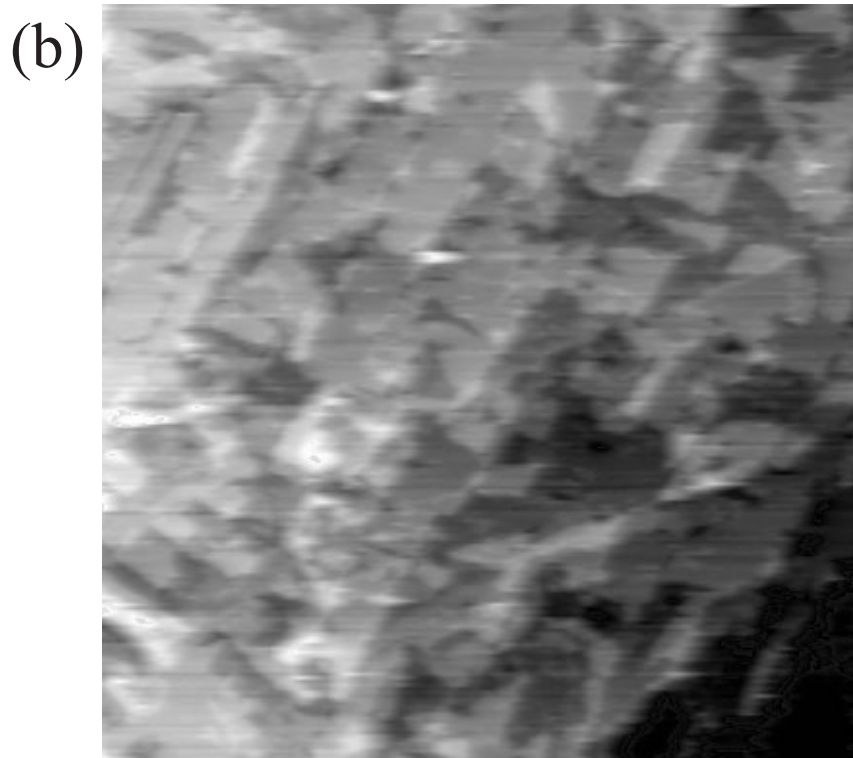
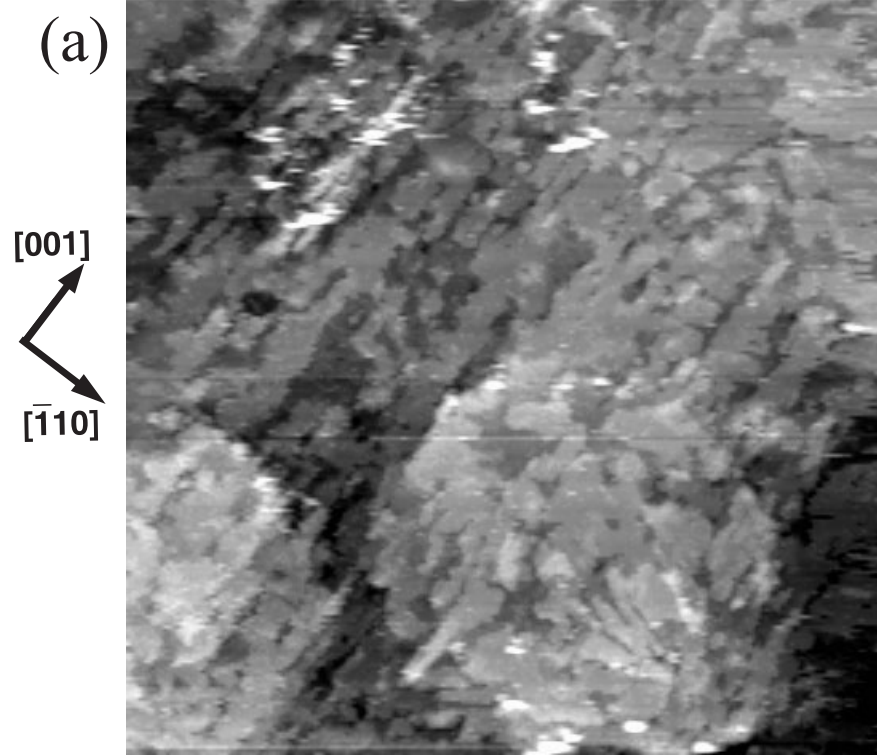
face and interface free energies of the film-substrate system as well as kinetically from kinetic parameters such as diffusion barriers [106, 107]. One expects that the growth of the oxide film is mostly kinetically determined at low T_{prep} s, and more and more by thermodynamic effects as T_{prep} goes up [108].

At $T_{\text{prep}} \sim 650$ K, step edges are very rough and hardly straight, making the uppermost oxide layer appear like cornflakes (Fig. 4.2a). The area of a rift-free single domain of the uppermost oxide layer is not large, at most $200 \text{ \AA} \times 200 \text{ \AA}$. At $T_{\text{prep}} \sim 700$ K, step edges are less rough and more straight, and rift-free single domains are a little larger than those at $T_{\text{prep}} \sim 650$ K (Fig. 4.2b). At $T_{\text{prep}} \sim 850$ K, step edges are straight and several hundred \AA long. The area of the single domains of the layer is larger than $400 \text{ \AA} \times 800 \text{ \AA}$ (Fig. 4.2c). At $T_{\text{prep}} \sim 900$ K, step edges are smoother than those at $T_{\text{prep}} \sim 850$ K.

A clean surface of the substrate Ru(0001) is shown in Fig. 4.3 for comparison. It has flat, broad terraces and ascending from left to right, monoatomic steps. The round bumps on terraces are due to subsurface bubbles of Ar atoms. They result from the Ar⁺ sputtering during sample cleaning and are not completely removed in the subsequent annealing [109]. Note that these subsurface bubbles are still shine through up to the oxide surface (Fig. 4.2c, indicated by a circle).

The thickness of the oxide film does not much depend on T_{prep} , in contrast to previous findings by STM and RHEED [96]. It is mostly 7 to 15 \AA regardless of T_{prep} between 650 K and 900 K. When the film is grown at 800 to 900 K, we occasionally find large mountains (several hundred to several thousand \AA diameter) in the oxide that are not flat at all. The RuO₂(110) film itself at $T_{\text{prep}} \sim 900$ K has still a thickness similar to that at $T_{\text{prep}} \sim 650$ K. It appears therefore that $\sim 15 \text{ \AA}$ represents some maximum thickness of epitaxially grown RuO₂(110), and when the oxidation proceeds further, the film does not grow any more epitaxially and becomes disordered.

The distance between (Ru-O) layers (Fig. 4.1) in [110] direction in the RuO₂(110) single crystal is 3.11 \AA [28]. Thus, the measured values of 7 to 15 \AA corresponds to 2 \sim 5 layers. Most steps on the oxide surface are one or two layers high (3 to 6 \AA), but steps 2.0 \AA high or 1.0 \AA high are also observed at high T_{prep} (Figs. 4.2c, d, indicated with short arrows). These less-than-monolayer-high steps reflect the step structures of the substrate, as will be discussed in section 4.3.3. Occasionally, we also observe step heights of less than one monolayer at the border of the oxide film and the Ru(0001) surface (Fig. 4.4). The atomic structure of the oxide film shows that the lowest layer (in



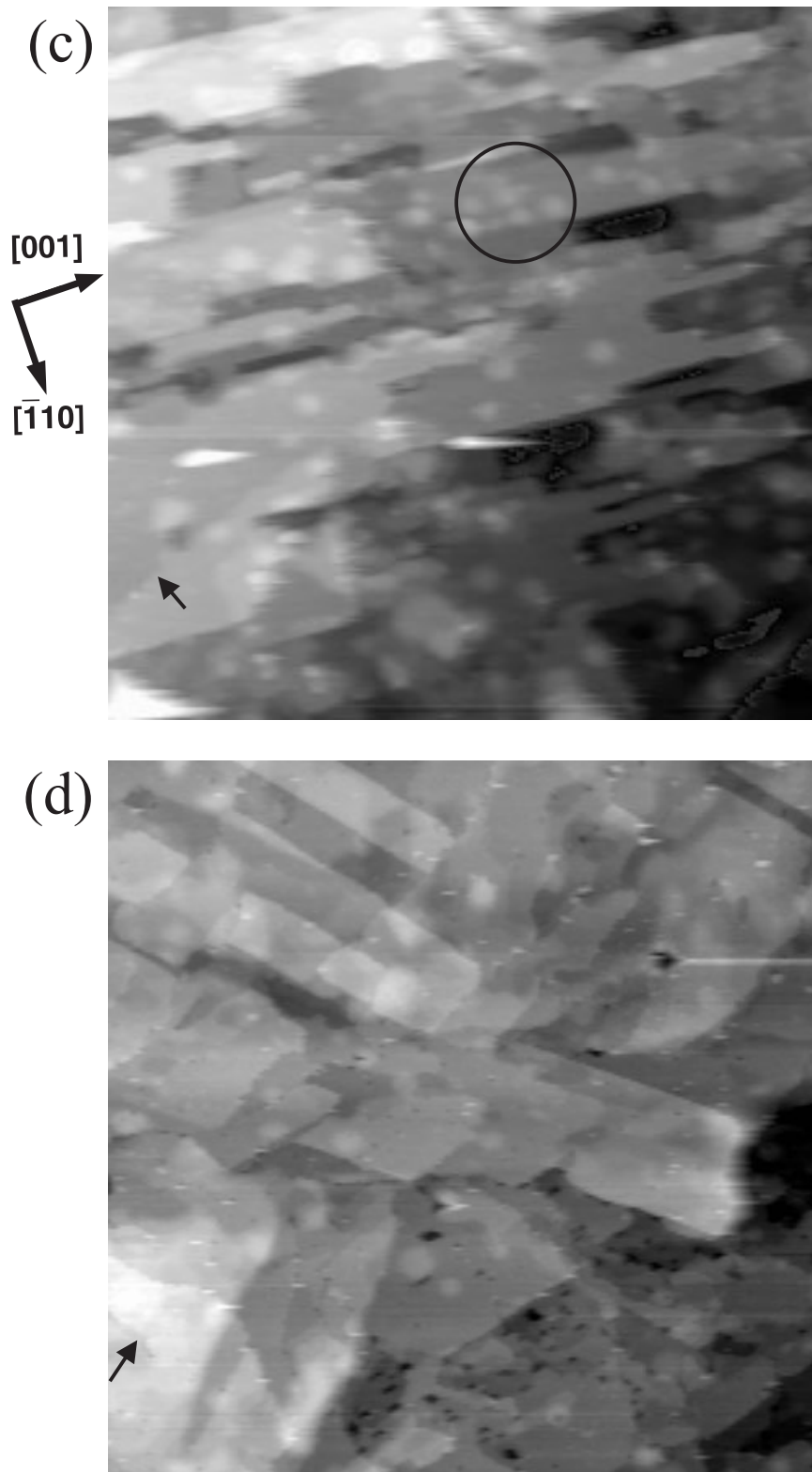


Figure 4.2: Mesoscopic morphology of the $\text{RuO}_2(110)$ oxide film grown at various preparation temperatures (T_{prep}). $T_{\text{prep}} =$ (a) 650 K, (b) 700 K, (c) 850 K, (d) 900 K. $U_{\text{T}} = -0.6$ V, $I_{\text{T}} = 2.2$ nA. $2700 \text{ \AA} \times 2700 \text{ \AA}$.

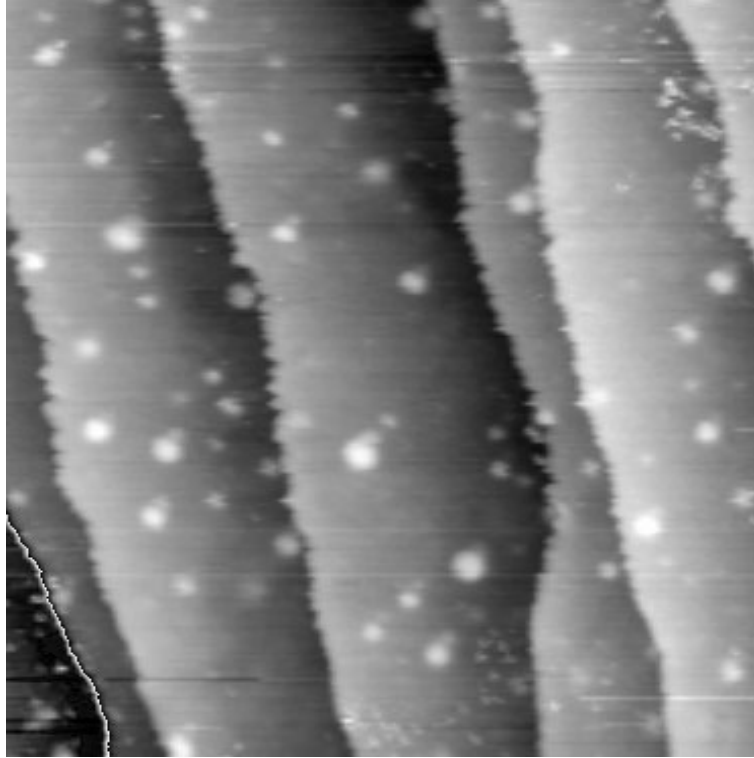


Figure 4.3: Mesoscopic morphology of clean Ru(0001). $U_T = -0.6$ V, $I_T = 2.2$ nA. $2700 \text{ \AA} \times 2700 \text{ \AA}$.

the middle of the image) is identical to that of the uppermost oxide layer (on the left of the image). This finding is different from the theoretical expectation (section 4.1) that a O-Ru-O trilayer is unfolded into a more open $\text{RuO}_2(110)$ rutile structure when at least two trilayers are stacked [101]. The lowest layer in Fig. 4.4 is only $\sim 0.5 \text{ \AA}$ higher than the substrate. We can explain this phenomenon in the following way. Because a monolayer oxide film is 3.11 \AA thick [28], the oxide film must be $\sim 2.5 \text{ \AA}$ embedded in the substrate. The depth roughly corresponds to the height of a monoatomic step of Ru(0001), 2.15 \AA [101]. Therefore, the oxide film can be regarded as having grown on a substrate layer one step lower.

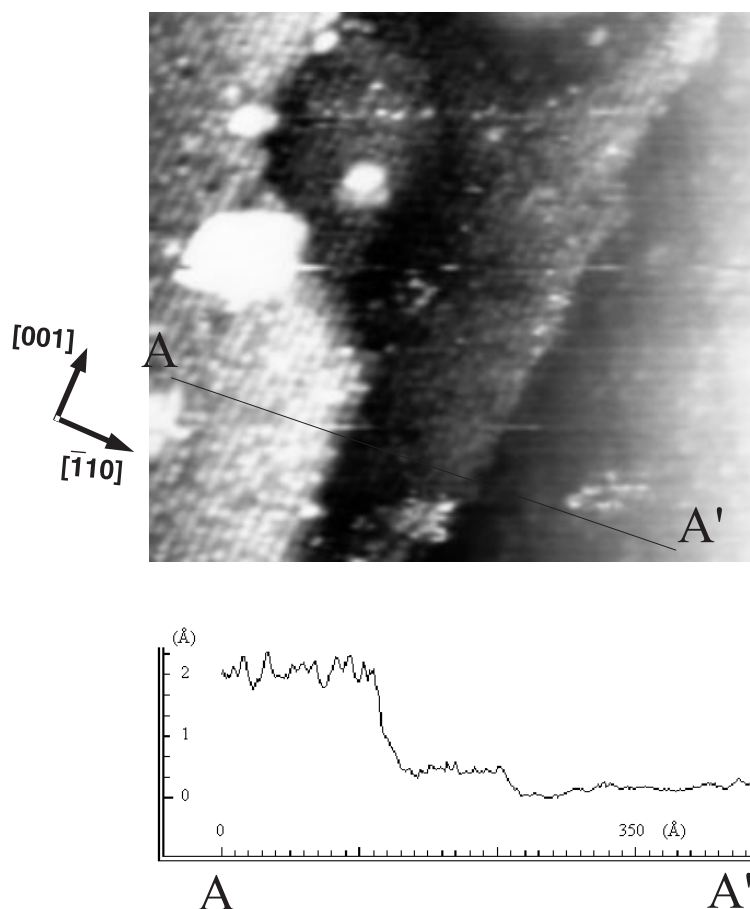
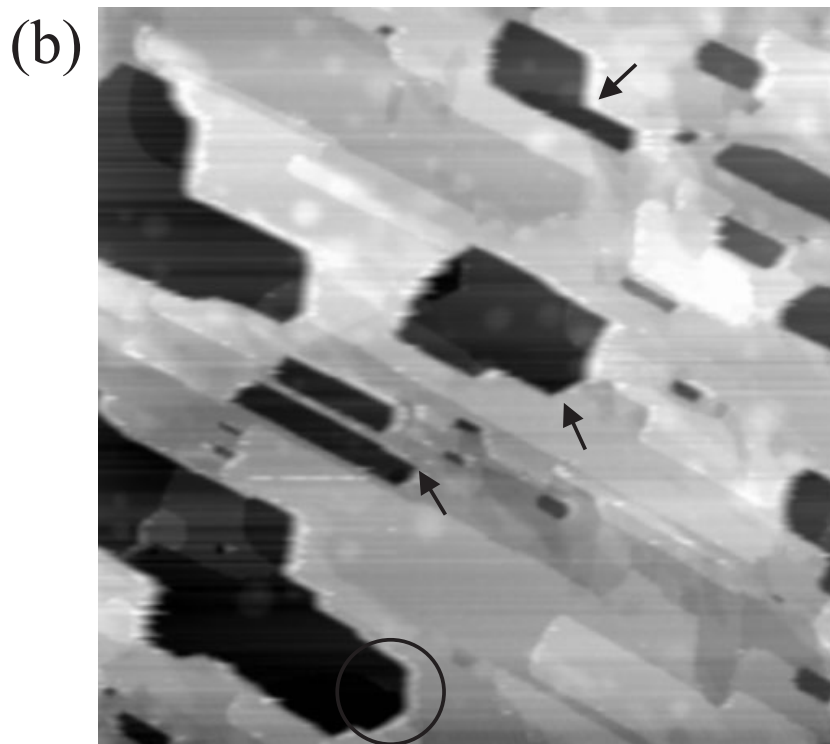
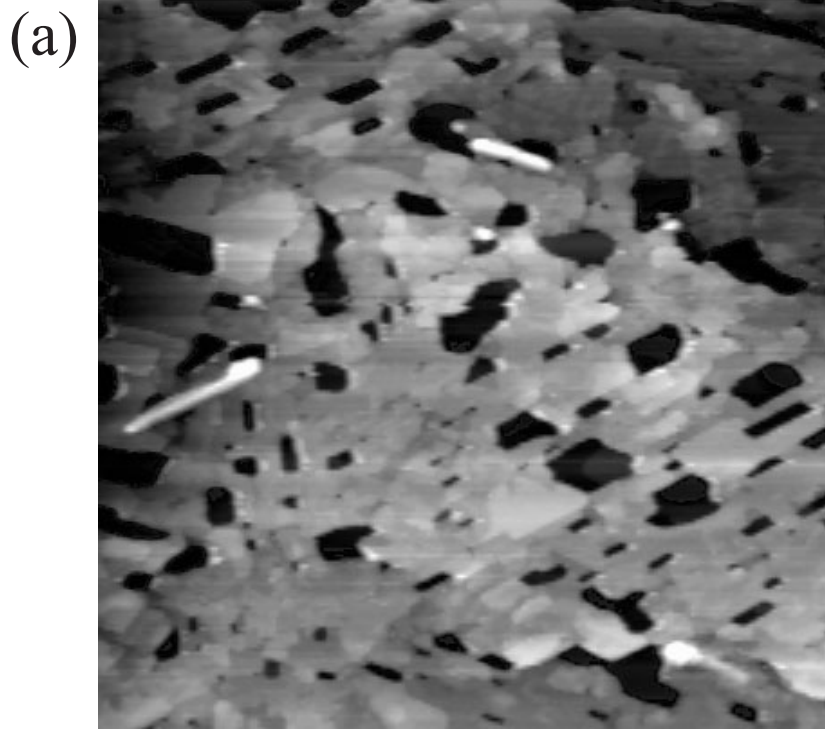


Figure 4.4: Monolayer thick oxide film. $U_T = 0.6$ V, $I_T = 2.2$ nA. $450 \text{ \AA} \times 450 \text{ \AA}$.

4.3.2 Partial evaporation of the oxide film and its equilibrium morphology

The equilibrium morphology of the oxide film was determined from partial evaporation of the film by flashing up to various temperatures (Fig. 4.5). The film does not evaporate layer by layer, but parts of the oxide film evaporate and holes emerge. The holes always go entirely down to the substrate, once the size of the hole has reached a certain limit, while the thickness of the oxide is unchanged. As the flash temperature goes higher, the holes grow larger and eventually merge each other (Figs. 4.5 a–c).

The holes have a characteristic form. When they exist in a terrace of the oxide film, their corners are mostly not rectangular, but have



[001] [110]

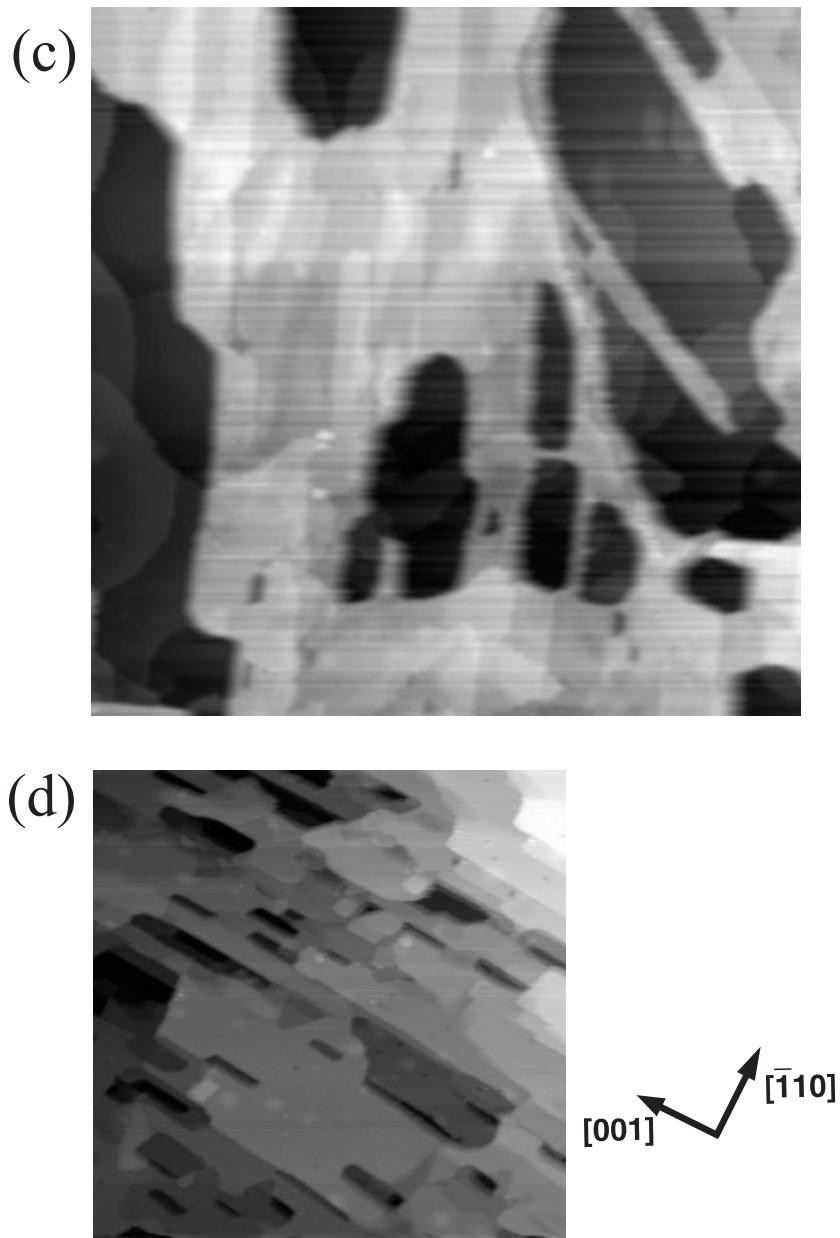


Figure 4.5: Mesoscopic morphology of the partially evaporated oxide film after flashing to increasing temperatures. (a) Flash up to 750 K, (b) up to 800 K, (c) up to 850 K. (d) Detailed structure of the holes at their initial state. $U_T = -0.6$ V, $I_T = 2.2$ nA. (a)-(c) $2700 \text{ \AA} \times 2700 \text{ \AA}$, (d) $1600 \text{ \AA} \times 1600 \text{ \AA}$.

acute or obtuse angles to the $[001]$ direction (Fig. 4.5b, indicated with arrows). The acute angle is 50° to 70° to the $[001]$ direction. Sometimes, when the holes become bigger, two slanting sides meet and form hexagonally shaped corners (Fig. 4.5b, indicated with a circle).

This obliqueness can be readily explained if one looks carefully into the atomic model of $\text{RuO}_2(110)$ surface (Fig. 4.6). In the perpendicular direction to $[001]$ direction, i.e. $[\bar{1}10]$ direction, there are four bonds (two A bonds, two B bonds in Fig. 4.6a) per vertical unit cell to break down (indicated with arrows) in order to cleave the film. On the other and, in a slant direction (26°) to $[\bar{1}10]$ direction, there is one more bond (C bond in Fig. 4.6b) to break down. However, if we compare the densities of the bonds per (vertical) unit area along the two directions, they are almost the same. In $[\bar{1}10]$ direction, there are four bonds in $6.38 \text{ \AA} \times 3.11 \text{ \AA}$ [9] ($0.200 \text{ bond} / \text{\AA}^2$). In the slant direction, there are five bonds in $7.10 \text{ \AA} \times 3.11 \text{ \AA}$ ($0.225 \text{ bond} / \text{\AA}^2$). If we assume that the strength of the bonds are similar, it costs for a hole almost the same energy per unit area to have a vertical side in both cases.

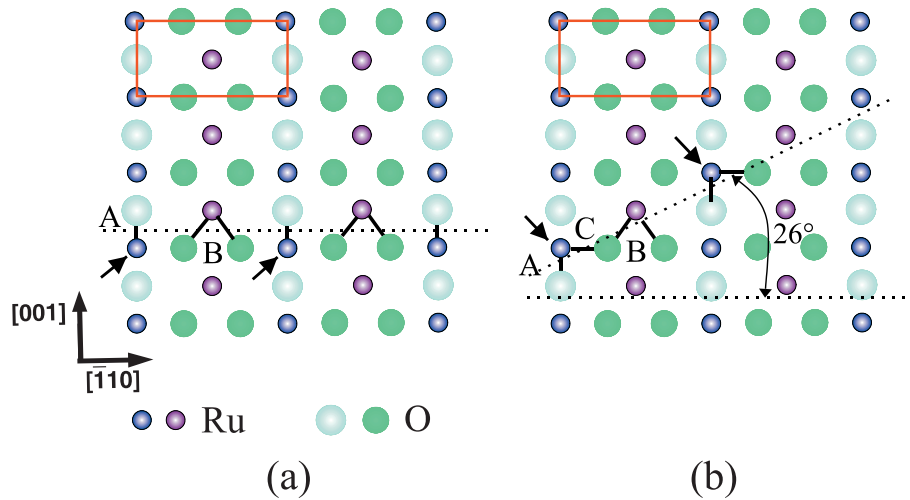


Figure 4.6: Top view of the stick-and-ball model of the $\text{RuO}_2(110)$ surface. A rectangle in each image indicates the unit cell of the surface whose size is $6.38 \text{ \AA} \times 3.11 \text{ \AA}$ [9]. (a) Breaking down of bonds in $[\bar{1}10]$ direction. (b) Breaking down of bonds in a slant direction to $[\bar{1}10]$ direction.

Another characteristic of the holes is that, from the initial state of the formation (Fig. 4.5d), they are always longer in $[001]$ direction. In addition, the atomic structure of the holes shows that the hole goes down to the $\text{Ru}(0001)$ surface and that part of the hole is covered by

the (2×2) -O structure (Fig. 4.7). This characteristic shape of the holes can be analyzed quantitatively by a thermodynamic analysis I will present below.

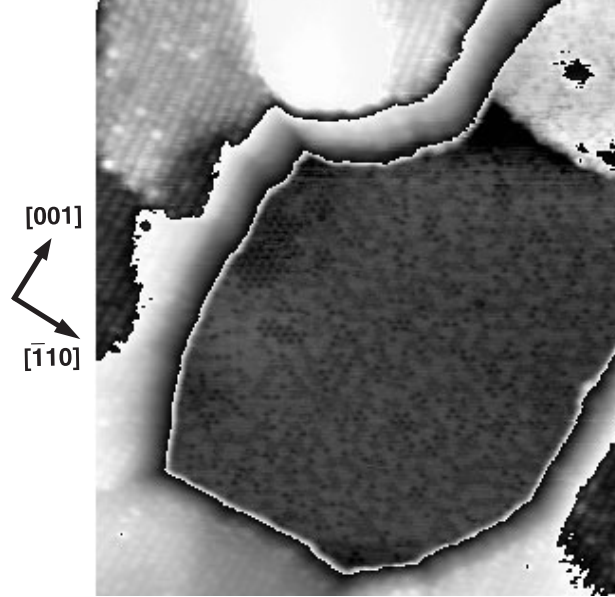


Figure 4.7: Atomic structure of a hole and the oxide film around it. $U_T = 0.6$ V, $I_T = 2.2$ nA. $250 \text{ \AA} \times 260 \text{ \AA}$.

In general, when a crystal grows on a substrate, the equilibrium shape (ES) of the grown crystal can be determined when the related surface free energies are known [110]. Inversely, the relation of the surface free energies can be determined when the ES on the substrate is known [111]. These relations are based on the Wulff construction for the free ES of a crystal without substrate [112, 113].

In the Wulff construction, the ratio of the distance from the center-of-mass of the crystal O (Wulff's point) to the i -th surface r_i and the surface free energy of the i -th surface γ_i is constant,

$$\frac{r_1}{\gamma_1} = \frac{r_2}{\gamma_2} = \dots = C. \quad (4.1)$$

In the presence of a substrate, we can still use the relation by adding the effective surface energy of the free surface contacting the substrate γ^* (Fig. 4.8) [111]. γ^* is related to the surface energy of the interface $\gamma_{interface}$ and the surface energy of the substrate $\gamma_{substrate}$ as

$$\gamma^* = \gamma_{interface} - \gamma_{substrate}. \quad (4.2)$$

If γ^* is negative, Wulff's point O is located below the substrate surface (fig 4.8b). The adhesion energy between the crystal and the substrate β is

$$\beta = \gamma_{crystal} - \gamma^*, \quad (4.3)$$

where $0 < \beta < 2\gamma_{crystal}$, because $-\gamma_{crystal} < \gamma^* < \gamma_{crystal}$ [114]. For example, in the diagram in Fig. 4.8, $\gamma_{crystal}$ is γ_1 and $-\gamma_1 < \gamma^* < \gamma_1$. For γ^* outside of this range, the crystal would not contact the substrate or be fully embedded in the bulk, which are nonphysical situations during crystal growth.

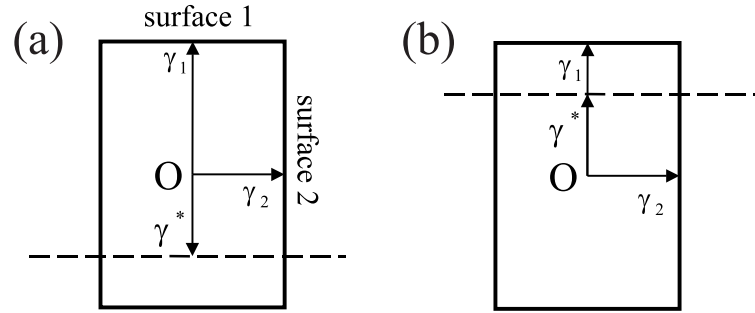


Figure 4.8: The Wulff diagram for a crystal growing on a substrate (side view). The dotted line indicates the surface of the substrate. (a) $\gamma^* > 0$, $\beta < \gamma_1$ (b) $\gamma^* < 0$, $\beta > \gamma_1$.

In the present case, although the overall morphology is influenced more and more by thermodynamic effects as T_{prep} is increased (Fig. 4.2), the shapes of the oxide grains are complicated. We believe that this phenomenon is due to their mesoscopic size. In other words, they are so large that it takes too much time to reach the ES even if T_{prep} is near the evaporation temperature of the oxide film. For the growth of mesoscopic crystals, several hours of annealing are usually needed to obtain the ES [115, 116]. However, we find small holes in large terraces like in Fig. 4.5d. Sometimes we also find isolated oxide islands on Ru(0001) with simple shapes (Fig. 4.9a). Because of the small size of these holes and islands and of the high T_{prep} of $850 \sim 900 \text{ K}^2$, we can assume that the growth condition for these holes and islands are near the thermodynamic equilibrium. However, the vertical growth

²The temperature range is near the evaporation temperature of the oxide film (see section 4.2).

may still be governed by kinetic restrictions or by the elastic energy between the substrate and the crystal.

The holes are usually parallelograms as discussed above. However, for simplicity, we model them as rectangular parallelepipeds with (001), ($\bar{1}10$), and (110) surfaces (Fig. 4.9b). Their depths are 9 ~ 15 Å, i.e. 3 ~ 5 oxide layers high *regardless* of their size. The heights of the holes are very low compared to their area, which ranges from 50 Å × 200 Å to 300 Å × 900 Å. The isolated islands are almost rectangular and their height is also 9 ~ 12 Å, i.e. 3 ~ 4 oxide layers high *regardless* of their size. The heights of the islands are also very low compared to their area, which ranges from 50 Å × 250 Å to 450 Å × 850 Å. The islands can also be modelled as rectangular parallelepipeds with the same surfaces as the holes.

Let the surface energies of the three different types of surfaces, (001), ($\bar{1}10$), and (110) surfaces be γ_{001} , $\gamma_{\bar{1}10}$, and γ_{110} , respectively. Then from Eq. (4.1),

$$\frac{h + h'}{\gamma_{110}} = \frac{a}{\gamma_{001}} = \frac{b}{\gamma_{\bar{1}10}}, \quad (4.4)$$

and from Eq. (4.3),

$$\beta = \gamma_{110} - \gamma^*, \quad (4.5)$$

where the symbols are explained in Figs. 4.8a, b and 4.9c.

Now, we can compare the surface free energies of the oxide surfaces from Eq. (4.4). Some examples of holes and islands are listed in Table 4.1. The ratios between $\gamma_{\bar{1}10}$ and γ_{001} are readily calculated and γ_{001} is 2 ~ 5 times higher than $\gamma_{\bar{1}10}$. In other words, it costs for the holes 2 ~ 5 times more energy to have a (001) surface than a ($\bar{1}10$) surface of the same area. This fact also explains the mesoscopic morphology of the oxide film. The uppermost oxide film always shows 2 ~ 5 times longer terraces in [001] direction than in [$\bar{1}10$] direction (Figs. 4.2c, d).

Table 4.1: Examples of various sizes of holes and isolated islands and the ratio of surface energies of the vertical sides of the holes and the islands. About 10 holes and 10 islands are measured. Parameters from Fig. 4.9

islands size	a (Å)	b (Å)	h (Å)	$\gamma_{\bar{1}10} : \gamma_{001}$
larger one	830	420	12	1 : 2.0
medium one	450	200	10	1 : 2.3
smaller one	270	80	12	1 : 3.4

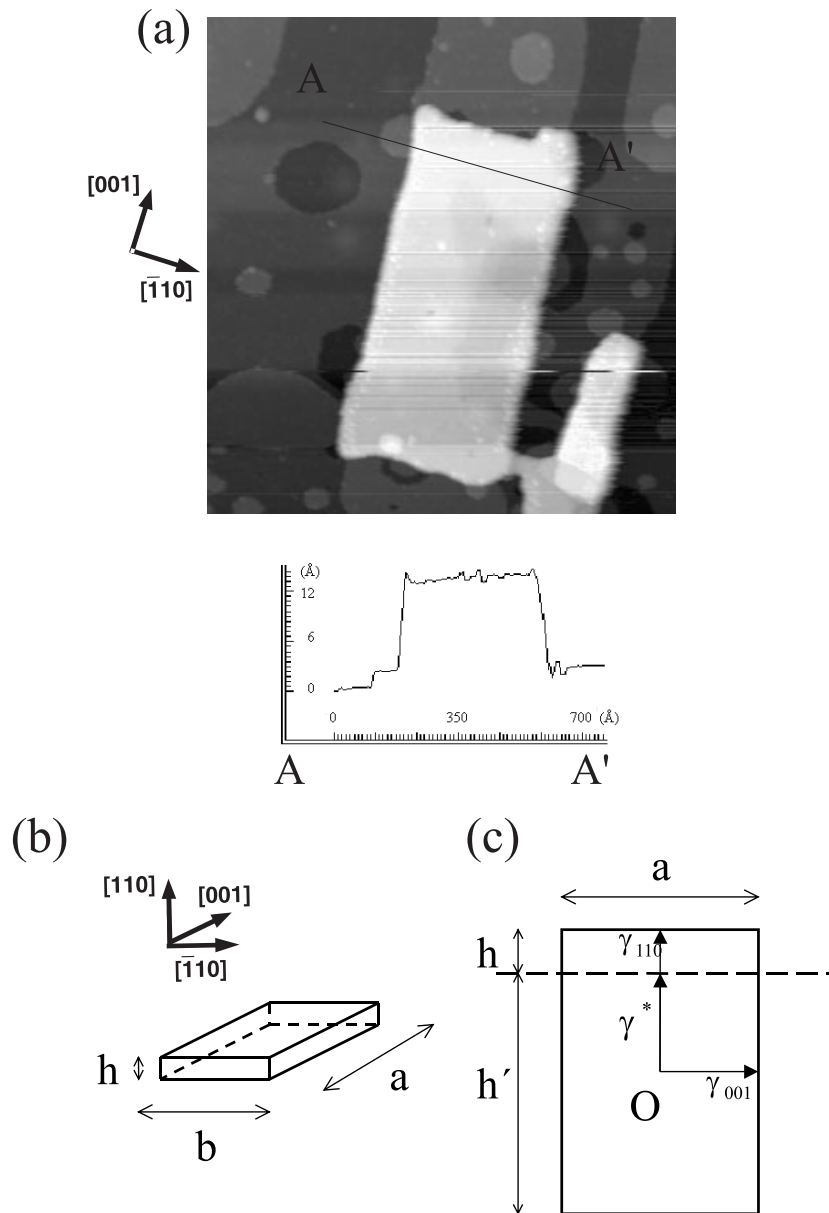


Figure 4.9: Isolated oxide island near the ES. (a) An isolated oxide island near the ES. $U_T = -0.5$ V, $I_T = 2.2$ nA. $1150 \text{ \AA} \times 1150 \text{ \AA}$. (b) Model of the island. This model is applied also to the holes with a simple shape. (c) Wulff diagram for the model in (b) with substrate (dotted line). See text for the nomenclature.

If we consider the surface energy as the average strength of bonds perpendicular to the surface, the bonds in $[\bar{1}10]$ direction are $2 \sim 5$ times weaker than the bonds in $[001]$ direction.

For comparison of γ_{110} with γ_{001} or $\gamma_{\bar{1}10}$, h' should be known, which was impossible from our images.

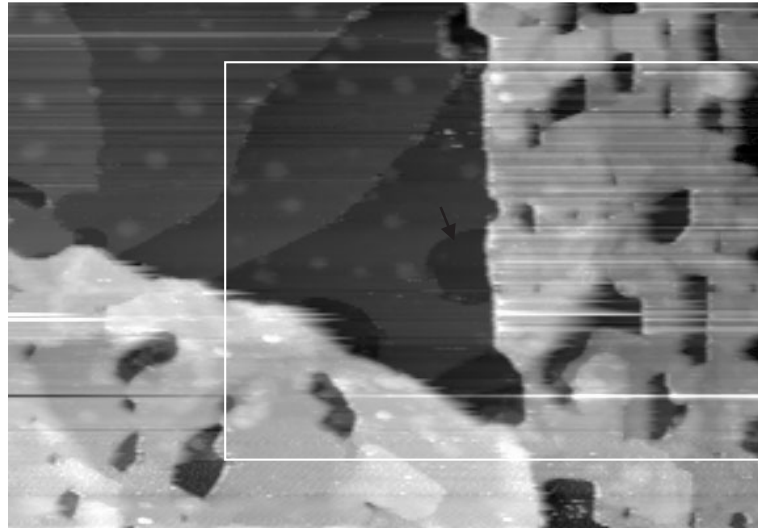
4.3.3 The Ru(0001) substrate in the proximity of the oxide film

Finally, I discuss the Ru(0001) surface in the proximity of the oxide film. It is obvious from Fig. 4.10a that the step edges on the substrate have little effect on the growth of the oxide film. The oxide film seems to grow across the step edges, and the step edges look similar as on the clean Ru(0001) (Fig. 4.3).

The substrate at the border with the oxide film, however, is moderately affected by the formation of the oxide film. One observes monoatomic deep large holes on the terrace directly at the border with the oxide film (indicated with an arrow). The vacant Ru atoms from the holes should be used to build the oxide film. Presumably, they are the exposed parts of a more complicated morphology of the substrate beneath the oxide film. Indeed, we observe the extended morphology of the holes beneath the oxide film by subtracting the height of the oxide film from the image (Fig. 4.10b, indicated with dark arrows). It means that the steps on the substrate are occasionally reflected by the morphology of the oxide surface. Steps on the oxide due to steps on the substrate have different heights than the height of the intrinsic oxide step (Fig. 4.10c). The line profile along a white line in Fig. 4.10b shows that a step due to the substrate (indicated with A) is ~ 2.0 Å high, reflecting the height of steps on Ru(0001), while an intrinsic oxide step (indicated with B) is ~ 3.5 Å high. Steps less than the oxide monolayer high were mentioned in section 4.3. Fig. 4.11 shows the structure of such steps schematically.

After flashing off most of the oxide film, the morphology of the Ru surface is very different from that of the well prepared, bare Ru(0001). In Fig. 4.12a, some remnant oxide islands are observed. The substrate in the proximity of the oxide islands shows a very complicated morphology. Steps are still mostly one layer high, but the terraces are much smaller than on clean Ru(0001). Altogether about 4 layers of Ru (A to D in Fig. 4.12a) are affected in this way. Such a complicated morphology of the substrate is mainly due to the Ru atoms evaporated during evaporation of the oxide film. Flashes even up to 1600 K only remove the oxygen atoms, whereas the Ru atoms remain on the surface [117].

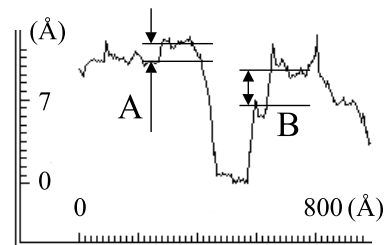
The density of Ru atoms in one oxide layer is ~ 65 % of the density



(a)



(b)



(c)

Figure 4.10: (a) The Ru(0001) surface at the border of the oxide film. $3680 \text{ \AA} \times 2300 \text{ \AA}$. (b) The same area (indicated with a rectangle in (a)) with the height of the oxide film subtracted. Some steps on the Ru(0001) continue to the steps on the Ru(0001) beneath the oxide film (indicated with dark arrows). $2400 \text{ \AA} \times 1600 \text{ \AA}$. (c) Line profile along the white line in (b). Step A (due to the substrate) has a different height than step B (intrinsic oxide step) $U_T = 0.6 \text{ V}$, $I_T = 2.2 \text{ nA}$.

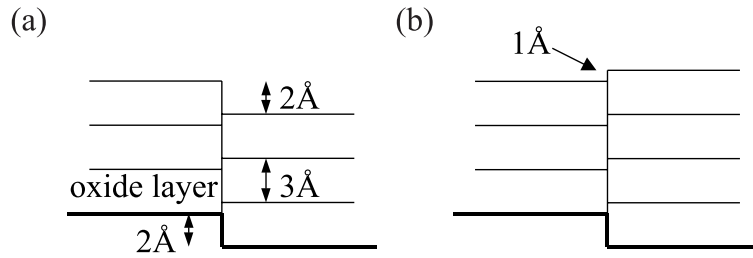


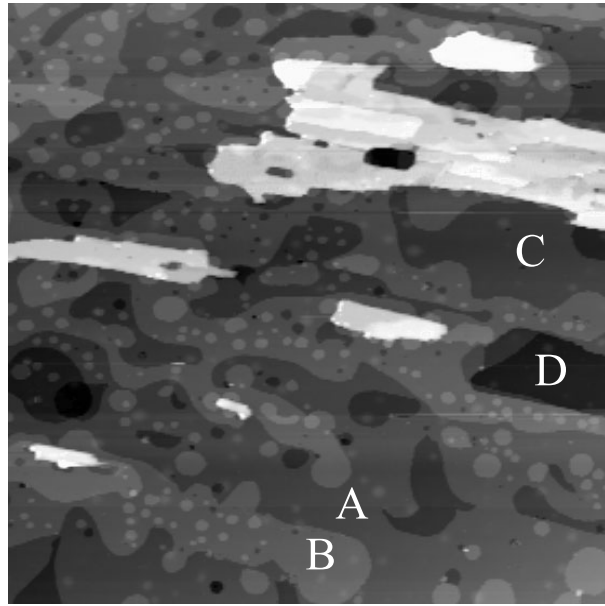
Figure 4.11: Model for steps less than one oxide layer high. Thicker lines at the bottom indicate the substrates with a step. (a) 2.0 Å high step on the oxide surface, (b) 1.0 Å high step on the oxide surface. All distances are approximate ones. Note that the uppermost steps are as disrupted as the steps on the substrate.

of Ru atoms on the substrate. In section 4.3.2 we found that the oxide film does not evaporate layer by layer and the remaining oxide film retains its height. Here the remaining oxide film was ~ 12 Å high, suggesting that the original oxide film is also ~ 12 Å, i.e. four monolayers high. When an oxide film of four monolayer thick is evaporated, 2.6 ML (0.65×4) of Ru atoms will remain on the same area. From this estimation we conclude that the substrate layers A, B, C, D, and many small round adatom islands in Fig. 4.12a are formed from the Ru atoms of the evaporated oxide film.

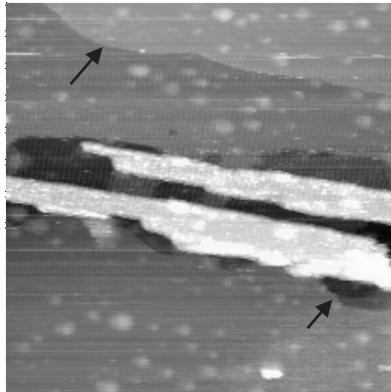
In particular, small round islands on layers A and B must have formed from Ru atoms which did not have enough energy to diffuse downwards across the steps (interlayer diffusion). Although the atoms do not have enough energy to reach lower layers, they form compact islands, because diffusion along the periphery of an adatom island costs less energy than interlayer diffusion [118]. The energy difference manifests itself in the fact that most adatom islands are located on the highest layer of the substrate (layer B), while there are fewer adatom islands on the one step lower layer (layer A) and much fewer on the two steps lower layer (layer C) in Fig. 4.12a.

This explanation is further supported by the morphology of the substrate at the proximity of intact oxide grains (Fig. 4.12b). The substrate terraces are monoatomic, and the steps are similar to those on the clean $\text{Ru}(0001)$ (indicated with a long arrow). Just at the border of the oxide islands, there are holes as is observed in Fig. 4.10 (indicated with a short arrow in Fig. 4.10a).

The shape of adatom islands on terraces was investigated in more detail (Fig. 4.13). The ES of the islands of the same species as the



(a)



(b)

Figure 4.12: (a) The Ru(0001) surface in the proximity of an evaporated oxide film. $U_T = 0.6$ V, $I_T = 2.2$ nA. $3700 \text{ \AA} \times 3700 \text{ \AA}$. (b) A Ru(0001) surface in the proximity of an intact oxide film for comparison. $U_T = -0.6$ V, $I_T = 2.2$ nA. $2300 \text{ \AA} \times 2300 \text{ \AA}$.

substrate is usually a polygon reflecting the symmetry of the substrate, and it becomes more and more circular with increasing sample temperature. This temperature dependence of the corners has its origin in the product of the step energy of the straight step and the configurational entropy of the kinked steps [118, 119]. The adatom islands in

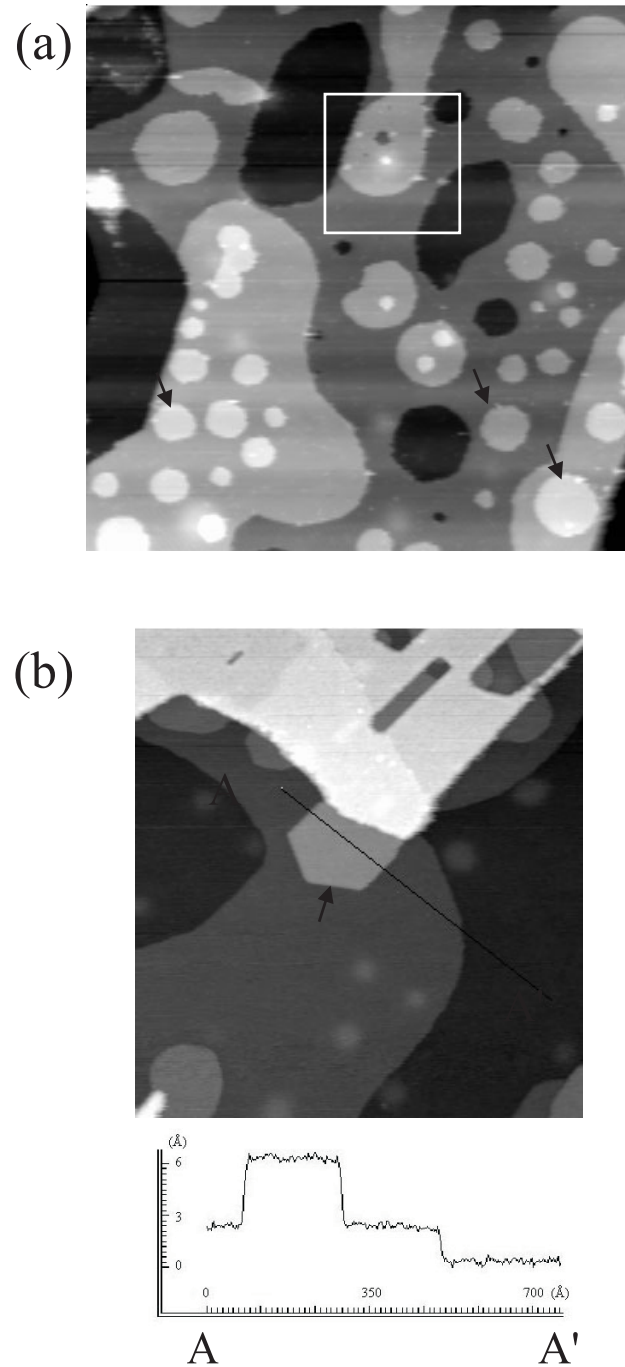


Figure 4.13: (a) Ru islands on $\text{Ru}(0001)$ in the proximity of the evaporated oxide film. Some adatom islands are indicated with arrows. $U_T = 0.6$ V, $I_T = 2.2$ nA. $1160 \text{ \AA} \times 1160 \text{ \AA}$. (b) A Ru island with a well defined shape due to a thickness of two layers (indicated with an arrow). Note that this island is connected with the oxide film in the upper part of the image. The line profile shows that the island is two layers ($\sim 4 \text{ \AA}$) high. Flash up to 850 K. $U_T = -0.6$ V, $I_T = 2.2$ nA. $1080 \text{ \AA} \times 1080 \text{ \AA}$.

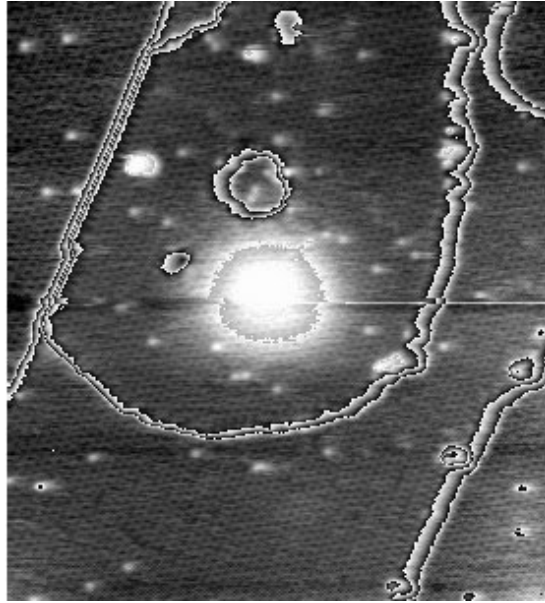


Figure 4.14: (2×2) -O adlayer on a Ru island magnified from Fig. 4.13a. The magnified area is indicated with a square in fig 4.13a. $U_T = 0.6$ V, $I_T = 2.2$ nA. $265 \text{ \AA} \times 265 \text{ \AA}$.

Fig. 4.13a have diffuse hexagonal or circular forms, suggesting that the temperature is already high enough for the islands to have equilibrium shapes. On the other hand, Fig. 4.13b shows a hexagonal island of Ru atoms in the proximity of the oxide film that has a different shape with sharp corners (indicated with an arrow). The difference is that this island is *two* monolayers high (Fig. 4.13b, line profile). Its steps therefore have higher step energies than monoatomic steps. Therefore, the island would need even higher temperatures for the corners to become round as for the monoatomic islands in fig 4.13a.

In usual epitaxy or thin film growth experiments, most islands are just one monolayer high. It is a very rare case that there exist adatom islands two monolayer high. We observe such a rare island formation here because the adatom island in Fig. 4.13b is formed from the Ru atoms resolved from the oxide film which is connected to the island. Presumably, the resolved Ru atoms first form a monolayer high adatom island alongside the oxide film. More resolved Ru atoms diffuse onto the island, but they do not have enough energy to cross the step. Instead, they fill the entire area of the monolayer island, hence forming an island two monolayer high. Using the Wulff construction as in section 4.3.2, it is concluded that the step energies of the island are nearly equal.

This phenomenon is usual for the ES of adatom islands on substrates with three-fold symmetry [118].

Finally, the atomic structure of the adatom island and the terrace shows that the Ru(0001) in the proximity of the oxide film is covered with the (2 × 2)-O adlayer (Fig. 4.14). Directly after the preparation of the oxide film, the remaining Ru(0001) surface is known to be covered by the (1 × 1)-O adlayer [9]. After preparation of the oxide film, the sample was flashed to 700 to 900 K before each measurement. This observation suggests that some amounts of the initially adsorbed oxygen desorb during these flashes.

4.3.4 Summary of section 4.3

The morphology of the oxide film RuO₂(110) grown on Ru(0001) is strongly dependent on the sample temperature during the preparation (T_{prep}). The growth of the oxide film is mostly kinetically determined at $T_{\text{prep}} \sim 650$ K, and thermodynamic effects on the morphology become more important as T_{prep} goes up to ~ 900 K. The thickness of the oxide film is independent of T_{prep} , and it ranges between 7 Å and 15 Å, i.e. 2 to 5 oxide (Ru-O) layers. We also occasionally find oxide films just 0.5 Å high which is explained as an oxide monolayer on a lower layer of the substrate. The structure of this oxide layer is already identical to that of a thicker oxide film, in contrast to the prediction by K. Reuter et al. [101]. A partial evaporation of the oxide film by flashing the sample to various temperatures reveals the stable morphology of the oxide film. The film does not evaporate layer by layer, but parts of the oxide film evaporate and holes emerge. The holes go entirely down to the substrate, once their size grows large enough while the thickness of the other parts of the oxide is unchanged. The holes have a characteristic form. They are parallelograms or rectangles and are longer in [001] direction. The surface energies of the vertical sides of the holes and of isolated oxide islands were analyzed by the Wulff construction. The surface free energy γ_{001} of the side of a hole is 2 to 5 times higher than $\gamma_{\bar{1}10}$. We are not able to compare the surface free energy of the oxide surface γ_{110} with either γ_{001} or $\gamma_{\bar{1}10}$ in this way due to kinetic restrictions and to the unknown elastic energy between the oxide islands and the substrate. There is no difference between the Ru(0001) morphology in the proximity of the oxide film and in the clean state. When the oxide film is evaporated, the dissolved Ru atoms from the evaporating oxide film remain on the substrate and form a complicated morphology of hexagonal or circular adatom islands. The step energies of the adatom

islands are nearly the same with each other. The Ru(0001) surface not covered by the oxide film is covered by the (2×2)-O adlayer, apparently because some amount of the adsorbed oxygen atoms desorbs during the repeated flashes to 700 to 900 K before each measurement.

4.4 Clean RuO₂(110) surface

Let us now turn to the physical and chemical processes of the oxide surface at the atomic level. The stoichiometric surface of RuO₂(110), RuO₂(110)–(1×1), and the nomenclature for adsorbates on the surface will be discussed first. In the introduction of chapter 4, a stick-and-ball model of the RuO₂(110) surface was shown (Fig. 4.1). The nomenclature used in that figure will be defined in this section. In order to explain the surface structure of RuO₂(110), the bulk structure of RuO₂ will be introduced first. RuO₂ has a rutile structure, which means that the Ru atoms are six-fold coordinated to oxygen atoms in an octahedral configuration, while the O atoms are three-fold coordinated to Ru atoms in a planar *sp*² hybridization. The RuO₂(110) surface is terminated by two kinds of O atoms and one kind of Ru atoms:

1. three-fold coordinated O as in bulk RuO₂,
2. two-fold coordinated O on bridge positions with respect to Ru atoms,
3. five-fold coordinated Ru atoms.

The atoms in 2 and 3 are one-fold undercoordinated with respect to the atoms in the bulk. I will call the five-fold coordinated Ru atoms ‘1f-cus Ru’ or Ru_{1f} according to previous studies (1f-cus stands for one-fold coordinatively unsaturated sites) [87]. The Ru atoms where the two-fold coordinated oxygen atom sits on are two-fold undercoordinated if the O atoms are removed. Therefore they will be called ‘2f-cus Ru’ or Ru_{2f}. The two-fold coordinated oxygen atoms are called bridge oxygen atoms (O_{br}) in previous studies [87, 89]. I will call them O_{2f} for a more systematical nomenclature that will be used in sections 4.5 and 4.6. ‘2f’ stands for ‘on 2f-cus Ru row’. In this way, O atom on Ru_{1f} will be called O_{1f}, CO on Ru_{1f} CO_{1f}, and on Ru_{2f} CO_{2f}. Then, the RuO₂(110) surface consists of Ru_{1f} rows and O_{2f} rows running in [001] direction (Fig. 4.1).

The undercoordinated atoms, Ru_{1f} and O_{2f}, play an important role in chemical processes on the surface because they possess dangling bonds. This electronic structure was revealed by DFT calculations [9]. It is different from usual metal surfaces, where the wave functions of conduction electrons at the surface are delocalized, so that energy differences between different adsorption sites are not so strong.

The calculated binding energy of CO_{1f} is 1.2 eV [9]. This value is considerably larger than CO binding energies on other oxide surfaces with typical values of 0.7 eV [120]. The reason is that there is backdonation from *d* states of the substrate located at E_F to the $2\pi^*$ orbitals of CO like in metals, whereas most other oxides, which are non-metallic, do not have *d* states at E_F . The binding energy of O_{2f} is 1.6 eV [9], which is 0.5 eV lower than that of O atoms in the (1 × 1)-O structure on Ru(0001) [86]. CO is thus more strongly bound than on the metallic Ru and O is less strongly bound. These factors make RuO₂ a good CO oxidation catalyst in contrast to the metallic Ru surface.

Directly after preparation of the oxide film, the surface is usually not stoichiometric. There are many contaminants on it, and the O_{2f} rows are usually not complete. To prepare a clean RuO₂(110) surface, the following preparation method was used [30]. First, by mild heating of the sample up to 700 K, most of the contaminants were desorbed. In order to completely fill the O_{2f} rows with oxygen atoms, the sample was then exposed to 1 to 2 L O₂ at room temperature. The O₂ molecules adsorb dissociatively on the Ru_{1f} rows. The sample was then heated again to 700 K, so that the adsorbed O_{1f} atoms could diffuse into the vacancies in the O_{2f} rows and thus complete the rows. Surplus O_{1f} atoms desorbed at around 400 K. Therefore, observation of an oxygen peak around 400 K at the last sample heating could be used as a criterium that the O_{2f} rows were complete, and that the Ru_{1f} rows were free of contaminants. If no oxygen peak was observed at around 400 K, the above described cycle was repeated until the peak occurred.

In the following, I discuss the STM images of the RuO₂(110)–(1 × 1) surface. In the stick-and-ball model of the stoichiometric surface, the Ru_{1f} rows and the O_{2f} rows run in [001] direction (Fig. 4.1). STM images of the clean RuO₂(110)–(1 × 1) surface indeed show alternating bright and dark rows expected from the model (Fig. 4.15). The image agrees with the previous STM study [9]. Bright rows consist of densely packed ovals if one closely looks into the image. The distance between centers of neighboring ovals is $\sim 3 \text{ \AA}$, and the distance between centers of neighboring bright rows is $\sim 6.5 \text{ \AA}$. This size of the unit cell agrees well with the known unit cell of the RuO₂(110)–(1 × 1) surface, 6.38

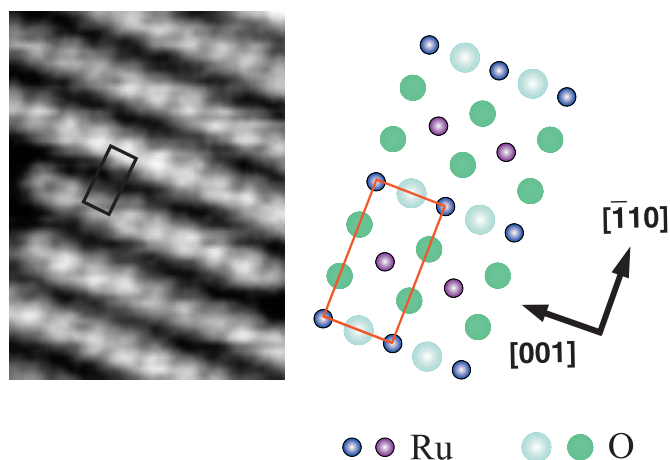


Figure 4.15: High resolution image of the stoichiometric RuO₂(110) surface. $U_T = -0.6$ V, $I_T = 2.2$ nA. $27 \text{ \AA} \times 40 \text{ \AA}$. The schematic on the right side is a top view of the RuO₂(110)–(1 × 1) model [28]. A rectangle in the image and in the model indicates the unit cell.

$\text{\AA} \times 3.11 \text{ \AA}$ [28]. The ovals turn out to be O_{2f} atoms, as will become clear in section 4.5. It was found that in most cases the O_{2f} rows were imaged as bright rows. In some cases they were imaged as dark rows, which was mostly correlated with an unstable state of the tip or when the tip state changed in the course of an experiment. However, the sample bias did not affect the contrast of the image.

This type of structure is clearly not the general structure of oxide surfaces. The few surface oxides or surfaces of bulk oxides that to date have been investigated on the atomic scale display quite different structures (Fig. 4.16). For example, the TiO₂(110) surface has the same structure as RuO₂(110) (Fig. 4.16a). A Pd₅O₆ oxide film grown on Pd(111) shows very complicated structures (Fig. 4.16b). There is no corresponding bulk oxide of this film. Another surface oxide structure was just discovered by our group on Rh(111) (Fig. 4.16c).

A perfectly clean surface of RuO₂(110) was obtained only when the base pressure of the chamber was less than 1×10^{-10} Torr, because the clean surface of RuO₂(110) is very reactive to the rest gas in the chamber. This strict condition to maintain a clean surface is, however, not a serious problem for our investigation because even if the surface has defects or contaminants, these do not affect the adsorption behaviors of CO and O₂.

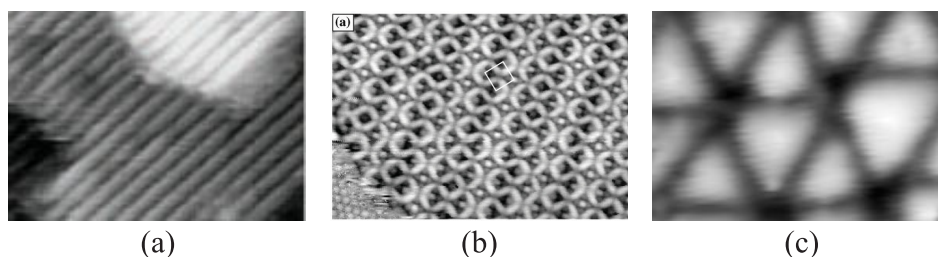


Figure 4.16: Diverse structures of other oxide surfaces. (a) $\text{TiO}_2(110)$ [121], (b) Pd_5O_6 [122], (c) Oxide on $\text{Rh}(111)$. $100 \text{ \AA} \times 70 \text{ \AA}$.

4.5 Structural analysis of the $\text{RuO}_2(110)$ surface during CO and O_2 adsorption

As introduced in section 4.1, the established model for CO oxidation on the $\text{RuO}_2(110)$ can be summarized as the Mars-van Krevelen mechanism [103]. When expressed with the nomenclature in section 4.4, O_{2f} oxidizes adsorbing CO. The oxide surface is restored by O atoms from the dissociatively adsorbing O_2 [9, 104]. The presently existing model, that is based on HREELS, TDS, LEED, and STM experiments, is summarized in the following.

At room temperature, CO adsorbs at first on the Ru_{1f} atom, but reacts off readily with a neighboring O_{2f} . After all of the O_{2f} is reacted off in this way, CO begins to occupy the Ru_{2f} sites. If the surface is exposed to O_2 in this state, the CO_{2f} reacts off with O_{1f} and the Ru_{2f} sites are covered again with O atoms. In this way the initial state of the $\text{RuO}_2(110)$ surface was believed to be restored. With further exposure to O_2 gas, dissociatively adsorbing O_2 fills the Ru_{1f} sites [87, 88, 89, 98].

Most parts of this model have not been verified with direct and microscopic methods yet. For example, at the very initial phase of the chemical processes, the reaction of O_{2f} with adsorbing CO has not yet been observed directly. With STM H. Over et al. observed vacancies in the bright rows of the oxide surface after they had exposed it to 0.5 L CO, but they did not monitor the *same* area before and after the exposure [96]. Therefore, it is not sure if the vacancies are due to reacted off O_{2f} atoms.

Furthermore, there are many unclear aspects in the model. For example, how densely do the CO molecules sit on the Ru_{2f} rows, and is CO_{1f} stable or not at room temperature. There is a DFT calculation which predicts a (1×1) superstructure of CO_{2f} [87]. But there is no

experimental evidence yet. While CO_{1f} was predicted to be unstable at room temperature [87] and the signal of the CO_{1f} had not been observed by HREELS [89], H. Over et al. interpreted their STM images to the contrary [96]. In addition, there is no experimental study about the *kinetics* and the *mechanisms* of the reactions between O_{2f} and CO_{1f} , between O_{1f} and CO_{1f} , and between O_{1f} and CO_{2f} ³.

In this section, a detailed structural analysis of the $\text{RuO}_2(110)$ surface during CO and O_2 adsorption will be presented. By exposing the $\text{RuO}_2(110)$ surface to CO or O_2 in small steps, e.g. 0.1 L, the sequence of the chemical processes on the surface at room temperature becomes clear, and states unclear from the macroscopic studies can be identified. After the structural analysis, an analysis of the dynamics of the processes will be presented, which is essential to reveal the reaction kinetics and mechanisms.

4.5.1 CO adsorption on the $\text{RuO}_2(110)-(1 \times 1)$ surface

In order to follow the adsorption and reaction of CO continuously from the beginning, at first an appropriate, flat area of the clean $\text{RuO}_2(110)$ surface was chosen. Then the surface was exposed to certain amounts of CO step by step while the STM tip was withdrawn in order to exclude the shadow effect of the tip.

First of all, the first step of the reaction on clean $\text{RuO}_2(110)$ between O_{2f} and CO_{1f} was investigated. Fig. 4.17 shows a direct observation of the reaction. Two images show the same area before and after exposure to CO. Vacancies are observed after the exposure (indicated with arrows). This observation clearly shows that the bright rows are the O_{2f} rows and dark rows are Ru_{1f} rows. This observation is quite remarkable considering that O_{2f} is imaged dark in STM images of $\text{TiO}_2(110)$ [121] and O atoms on metals are usually imaged as dark spots because the LDOS at E_F reduces due to the high electronegativity of oxygen atoms [27].

Fig. 4.18 shows a series of images, all recorded from the same area while the clean $\text{RuO}_2(110)$ surface was saturated with CO, and while the CO saturated surface was exposed to O again. In this series, two main features are important. One is the observation of two types of vacancies in the bright rows and the other additional bright dots in the dark rows.

³The reaction between O_{2f} and CO_{2f} is thought to occur at ~ 500 K [98].

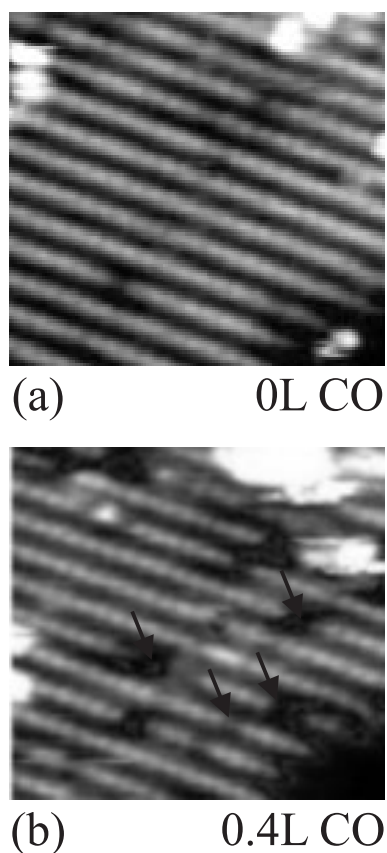


Figure 4.17: Direct observation of the reaction between O_{2f} and CO_{1f} at room temperature. (a) Clean $\text{RuO}_2(110)$, (b) the same area after the surface is exposed to 0.4 L CO. Vacancies due to the reaction are indicated with arrows. $U_T = -0.6$ V, $I_T = 2.2$ nA. $75 \text{ \AA} \times 70 \text{ \AA}$.

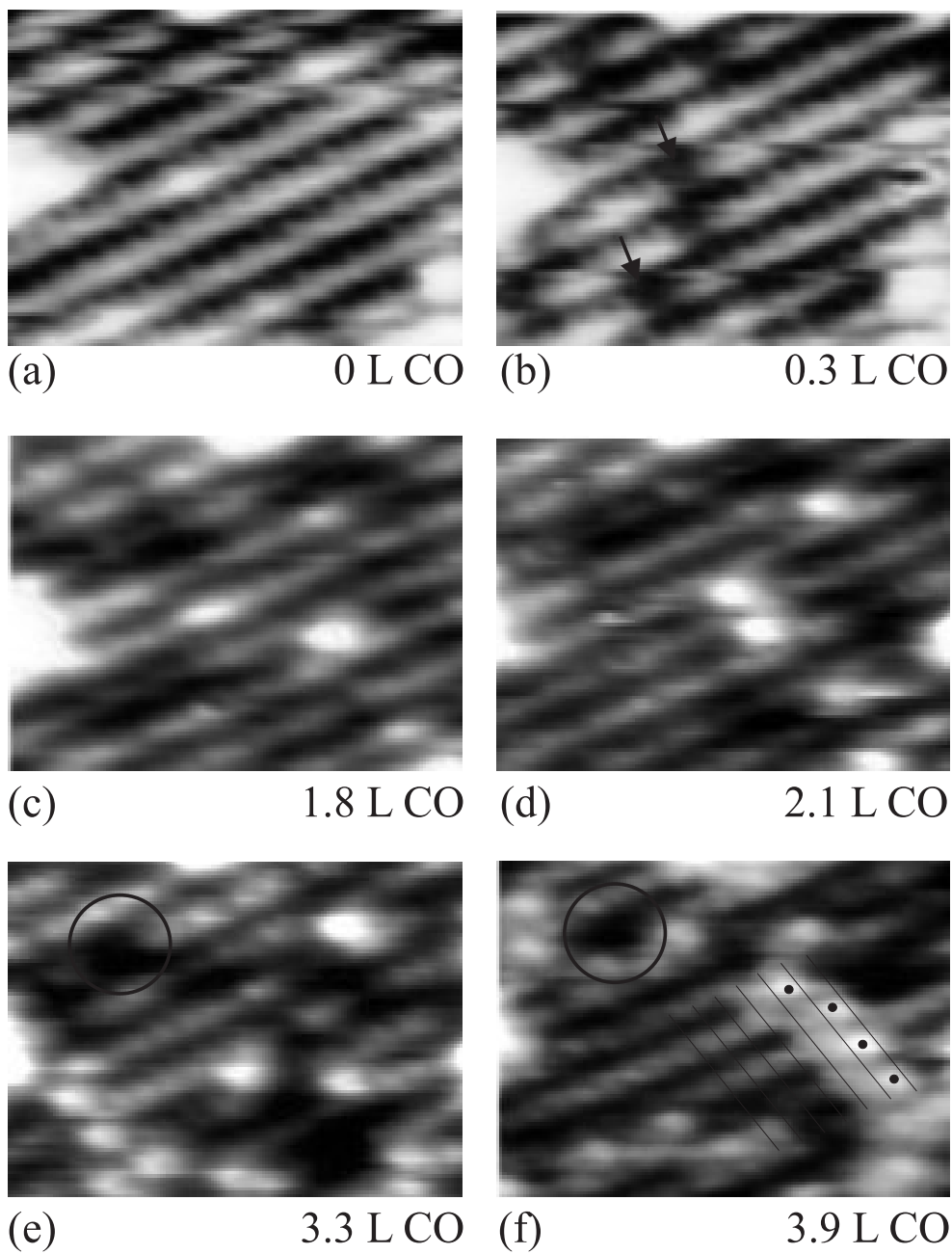
First, vacancies occur as the surface is exposed to CO (Fig. 4.18b, indicated with arrows). The vacancies make the brightness of the bright rows modulated as the surface is further exposed to CO (Fig. 4.18c, d). In this way, O_{2f} reacts off further while the surface is exposed to CO. According to the existing model, CO may sit in the vacancies of the O_{2f} row, but these molecules cannot react off with neighboring O_{2f} at room temperature [98]. We may expect that the vacancies and CO_{2f} will be imaged differently by STM. However, we cannot assign the brighter parts to CO_{2f} and the less bright parts to vacancies, or vice versa. This is because the changes in the modulation of the brightness are usually too subtle or not clear enough in series such as in Fig. 4.18. Therefore, we just assume that the modulated bright rows in Fig. 4.18c

or d have O_{2f}, vacancies, and CO_{2f} simultaneously.

As the RuO₂(110) surface is exposed to more CO, this modulation disappears and the brightness of the rows becomes constant again (Fig. 4.18f). The constant brightness means that the rows consist again of one species. If O_{2f} is reacted off completely but CO_{2f} is not stable at room temperature, the species should be Ru_{2f} atoms without CO_{2f} on them. If CO_{2f} is stable at room temperature, the species should be CO_{2f}, because the surface is already exposed to a considerable amount of CO. It will turn out that the species is CO_{2f} by studying the O₂ adsorption on the oxide surface saturated with CO (section 4.5.2). As is shown in Fig. 4.18f, the packing of CO_{2f} on the Ru_{2f} rows is as dense as of the O_{2f} atoms on the clean RuO₂(110) surface. This density of CO_{2f} at room temperature had been predicted by DFT calculations and by LEED observations [87].

In addition to the gray vacancies just discussed, there is another type of dark feature on the O rows. This feature is darker than the gray vacancies. Once it appears, it remains while dosing CO (Figs. 4.18e, f, indicated with circles) and dosing O₂ as well (Figs. 4.18j, k, indicated with circles) at the *same* position. It was observed many times that the darker vacancies *remain* at their positions in the course of repeated exposures to CO and O₂. These two types of features, i.e. the gray and dark ones, appear to be present in the STM data of H. Over et al., too [9]. In their experiment, H. Over et al. dosed 10 L of CO at room temperature, then heated the sample up to ~ 500 K. Then they observed that no CO remained on the surface, but that O_{2f} was regenerated with some dark features remaining. They interpreted the dark features as removed oxide double layers, where Ru_{2f} atoms have also been removed [98]. This was believed to happen while O atoms from deeper layers come to the surface, regenerating the O_{2f} rows. In these images, there were also some gray features that are different from the dark ones. According to the interpretation suggested here, these might be interpreted as O_{2f} vacancies. Taken together, the fact that both types of features were observed here just by CO adsorption indicates that etching of deeper layers already occurs at room temperature.

Second, when the oxide surface is exposed to more than ~3 L CO, we observe that CO begins to adsorb on the dark row, too (Figs. 4.18 e–h). For the beginning of this series, it was shown that the dark rows are Ru_{1f} rows (Fig. 4.18b). Because we are still observing the same area, the white dots on the dark rows should be adsorbed CO molecules on Ru_{1f} sites (CO_{1f}). The existence of CO_{1f} at room temperature has



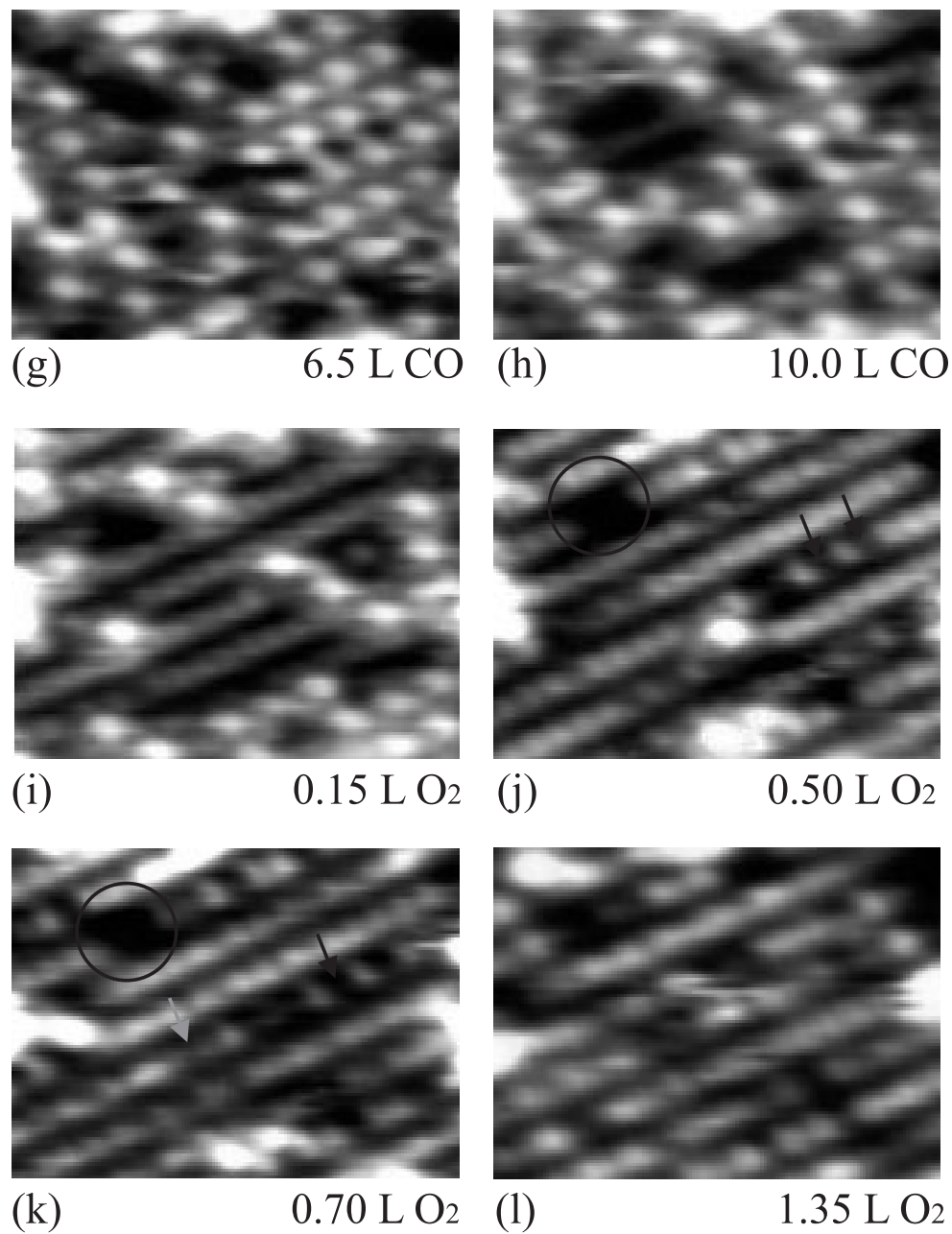


Figure 4.18: Changes of $\text{RuO}_2(110)$ during CO and O_2 adsorption. This series of images shows the same area of a clean $\text{RuO}_2(110)$ surface exposed first to CO up to saturation, then to O_2 . The exposure below each image is the total exposure of the surface to the gas. Circles in (e), (f), (j), and (k) show the same dark feature remained at its position. $U_T = -0.6$ V, $I_T = 2.2$ nA. $54 \text{ \AA} \times 40 \text{ \AA}$.

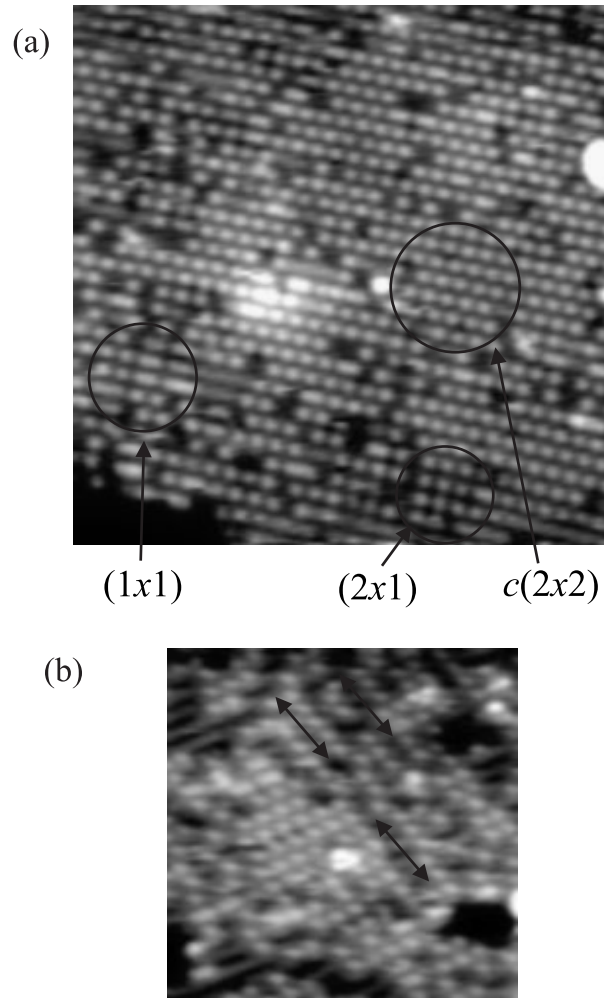


Figure 4.19: Superstructures of CO_{1f} . (a) At maximum coverage, $\theta_{\text{CO}_{1f}} = 0.5$, several superstructures are observed. A quasi-hexagonal $c(2 \times 2)$, a rectangular (2×1) , and occasionally also a (1×1) structure (indicated with circles). Elongated white dots in the circle for the (1×1) superstructure are two CO molecules on neighboring sites in a row. $U_T = 0.6$ V, $I_T = 2.2$ nA. $160 \text{ \AA} \times 160 \text{ \AA}$. (b) At an intermediate coverage, $\theta_{\text{CO}_{1f}} \sim 0.3$, chain like ordering of CO_{1f} across the Ru_{1f} and Ru_{2f} rows is observed (indicated with arrows). $U_T = -0.6$ V, $I_T = 2.2$ nA. $110 \text{ \AA} \times 110 \text{ \AA}$.

been unclear up to date [87, 89, 96]. The present observations clearly show that CO on Ru_{1f} is *stable* at room temperature. The bright rows in the image should then be CO_{2f} rows, which will be demonstrated in section 4.5.2. The adsorption sites of the CO_{1f} on the Ru_{1f} sites can be obtained from images showing atomic resolution along the bright

rows. Fig. 4.18f shows an example. Inspection of the thin parallel lines in the image shows that the CO_{1f}s are localized between maxima of neighboring bright rows. Assuming that these maxima represent CO molecules on Ru_{2f} sites, it means that the CO_{1f}s occupy the on-top sites of Ru_{1f} atoms (see the RuO₂(110) model in Fig. 4.15). This is because CO_{2f} should occupy bridge sites on the Ru_{2f} row as O_{2f} does [87]. This is exactly the expected adsorption site of the CO_{1f} molecules, in agreement with the HREELS measurement and DFT calculations [87, 88].

CO_{1f} frequently forms ordered structures as shown in Figs. 4.18g and 4.19. The maximum coverage of CO_{1f} ($\theta_{\text{CO}_{1f}}$) is ~ 0.5 , i.e. on an average, CO occupies every second Ru_{1f} atom. At high $\theta_{\text{CO}_{1f}}$, CO_{1f} forms two superstructures, a quasi-hexagonal $c(2 \times 2)$ structure and a rectangular (2×1) structure, and occasionally a (1×1) structure (Fig. 4.19a). At intermediate coverages, CO_{1f} molecules frequently form 1D chains perpendicular to the Ru_{1f} and Ru_{2f} rows (Fig. 4.19b). Although the CO_{1f} molecules are stable enough to be imaged with STM, they slowly desorb if the coverage is high ($\theta_{\text{CO}_{1f}} > 0.25$). In addition, they are much more mobile than CO_{2f}, O_{1f}, and O_{2f}. Mobility and reaction of CO_{1f} will be discussed in section 4.6.

Fig. 4.18 also shows the behavior of the surface upon further CO exposure. The surface was each time exposed to 0.5 L CO and imaged up to a total exposure of 10.0 L CO. The coverage of CO_{1f} remains around 0.25. This means that either CO does not adsorb any more on the Ru_{1f} rows, or that some CO desorbs again at higher coverages. In other experiments, we find that the maximum $\theta_{\text{CO}_{1f}}$ of 0.5 can be reached only if the surface is exposed to a large amount of CO (> 3 L) at one time or if the surface is exposed to partial pressures of CO higher than $\sim 10^{-8}$ Torr (Fig. 4.26 and Fig. 4.29).

4.5.2 O₂ adsorption on the CO/RuO₂(110) surface

In the experiment shown in Fig. 4.18, the surface was, after saturation with CO, subsequently exposed to O₂. With just 0.15 L of O₂, most of the CO_{1f} reacts off (Fig. 4.18i). With increasing exposure to O₂, the CO_{1f} reacts off completely, and vacancies begin to appear in the CO_{2f} rows (Fig. 4.18j, indicated with arrows). These vacancies directly show that the bright row must have consisted of CO because they appear during the reaction with oxygen. Again two types of vacancies (gray and dark) are observed (Fig. 4.18k, indicated with a gray and a dark arrows, respectively), and the brightness modulation along the CO_{2f}

rows changes with more adsorbed O_2 (Fig. 4.18l). This state is similar to the one in Fig. 4.18c or d. In short, the chemical processes are reversed in their order to those during exposure of the clean $\text{RuO}_2(110)$ surface to CO. It is again not clear whether the brightness modulation is due to vacancies or to O atoms adsorbed in these vacancies.

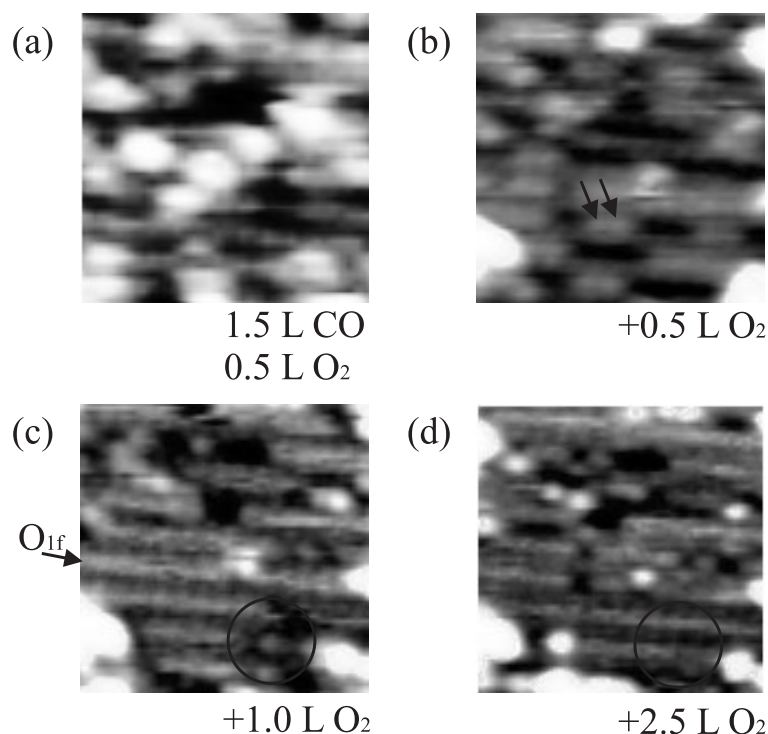


Figure 4.20: Structural changes of $\text{RuO}_2(110)$ surface during O_2 adsorption. This series of images shows the same area after exposed to O_2 . The indicated amount below each image is, (a) already dosed, (b)–(d) additionally dosed to (a). $U_T = -0.6$ V, $I_T = 2.2$ nA. 52 Å \times 48 Å.

Another aspect for the reaction is shown in Fig. 4.20. A clean $\text{RuO}_2(110)$ surface was successively exposed to 1.5 L CO and 0.5 L O_2 (Fig. 4.20a). There are vacancies in the bright rows and some white dots in the dark rows, presumably CO molecules. Although this surface cannot be characterized well, Fig. 4.20b shows that as most of the white dots in the dark rows have disappeared, some paired dots are observed in the dark rows (indicated with arrows). This means that additionally adsorbed O atoms adsorb in the Ru_{1f} rows (dark rows). Paired dots are readily explained as dissociatively adsorbed O_2 molecules. These pairs were also observed in a previous study [96]. With further exposure

to O_2 , more O_{1f} atoms fill the Ru_{1f} rows (Fig. 4.20c, indicated with arrows). In this case, they are imaged brighter than the bright rows (indicated with an arrow), but sometimes they appear similarly bright [95]. The adsorbed O atoms eventually fill some of the vacancies in the original bright rows (Fig. 4.20d, indicated with a circle), thereby recovering O_{2f} rows. O_{1f} forms a (1×1) superstructure on the Ru_{1f} rows in contrast to the (2×1) superstructure of CO_{1f} .

4.5.3 Summary of section 4.5

The structural aspects of CO and O_2 adsorption and reaction on the clean $RuO_2(110)$ surface at room temperature can be summarized as follows.

On the stoichiometric $RuO_2(110)-(1 \times 1)$ surface, CO adsorbs on Ru_{1f} atoms and reacts off readily with a neighboring O_{2f} , creating vacancies in the O_{2f} rows. There are two types of vacancies, shallow and deep one. Shallow ones are interpreted as O_{2f} vacancies. Deep ones presumably involve the removal of O_{2f} and Ru_{2f} atoms from the layer underneath. These deeper vacancies persist during the reaction. CO fills the Ru_{2f} rows as densely as O_{2f} did, forming a (1×1) superstructure. When the Ru_{2f} rows are fully covered with CO, CO begins to occupy Ru_{1f} sites. The adsorption site of CO_{1f} is on-top, consistent with the previous studies. The maximum coverage of CO_{1f} is 0.5. At high $\theta_{CO_{1f}}$, CO_{1f} forms two superstructures, a quasi-hexagonal $c(2 \times 2)$ structure and a rectangular (2×1) structure, and occasionally a (1×1) structure (Fig. 4.19a). When the CO saturated $RuO_2(110)$ surface is exposed to O_2 , O_2 molecules adsorb dissociatively on Ru_{1f} sites and react readily with CO_{1f} . When all of the CO_{1f} has reacted off, O_{1f} reacts with neighboring CO_{2f} , creating vacancies in the CO_{2f} rows. When all CO_{2f} has reacted off and O have occupied the Ru_{2f} sites, pairs of dissociatively adsorbed O atoms start to occupy Ru_{1f} sites. After higher oxygen exposure the Ru_{1f} rows are completely occupied, at least locally, by O atoms.

4.6 Analysis of the reaction dynamics and of the diffusion of CO and O on RuO₂(110)

4.6.1 Reaction between O_{2f} and CO_{1f}

When the clean RuO₂(110) surface is exposed to CO, most of the CO_{1f} molecules react immediately off with O_{2f}. However, some of the CO_{1f} molecules remain on Ru_{1f} rows long enough to be imaged by STM before they react off. Fig. 4.21 shows such reactions between CO_{1f} and O_{2f}. 30 seconds after exposing the stoichiometric RuO₂(110) to 0.3 L CO, three still unreacted CO molecules were observed on Ru_{1f} sites (Fig. 4.21b). After 90 seconds, one CO molecule disappeared and one vacancy appeared in the O_{2f} row nearby (Fig. 4.21c). After 210 seconds, the second CO disappeared and another vacancy appeared in the O_{2f} row (Fig. 4.21d). This observation verifies the model that CO adsorbs at first on the Ru_{1f} row and reacts with a neighboring O_{2f} on the stoichiometric RuO₂(110) [89, 98].

Fig. 4.22 shows a surface that was exposed to 0.8 L CO. There are vacancies in the O_{2f} rows where O_{2f} atoms have reacted with CO_{1f} (fig 4.22a). There are very few hopping events of the vacancies (fig 4.22b). From the analysis of the series, the hopping rate of the created vacancies in O_{2f} rows is $(4.2 \pm 4.7) \times 10^{-5} \text{ s}^{-1}$ at $\theta_{\text{O}_{2f}} \sim 0.7$ (Table 4.2). This result that the deviation in the rate is larger than the measured value is due to the fact that the hopping event is rare. For the most time during the observation, there does not occur any hopping. Therefore the deviation is so large, and this result means that the O_{2f} atoms are almost immobile at 300 K.

From the hopping rate the effective diffusion barrier E_{diff}^* of the hole can be estimated by postulating a preexponential factor Γ_{O} . With the usual assumption of 10^{13} s^{-1} for Γ_{O} , E_{diff}^* of the hole is 1.00 eV (Table 4.2). This value is reasonable considering the calculated diffusion barrier of O_{1f} on the RuO₂(110) surface (1.2 eV) [95]. O_{1f} is believed to be also almost immobile [95].

Such a low mobility means that unreacted O_{2f} remains at its position and reacts off randomly with CO. Accordingly, the distribution of vacancies shows where the reaction has occurred. Fig. 4.23a shows that the distribution of vacancies in the O_{2f} rows is statistical, indicating a random reaction probability.

Sometimes the reaction displays a weak tendency to proceed along

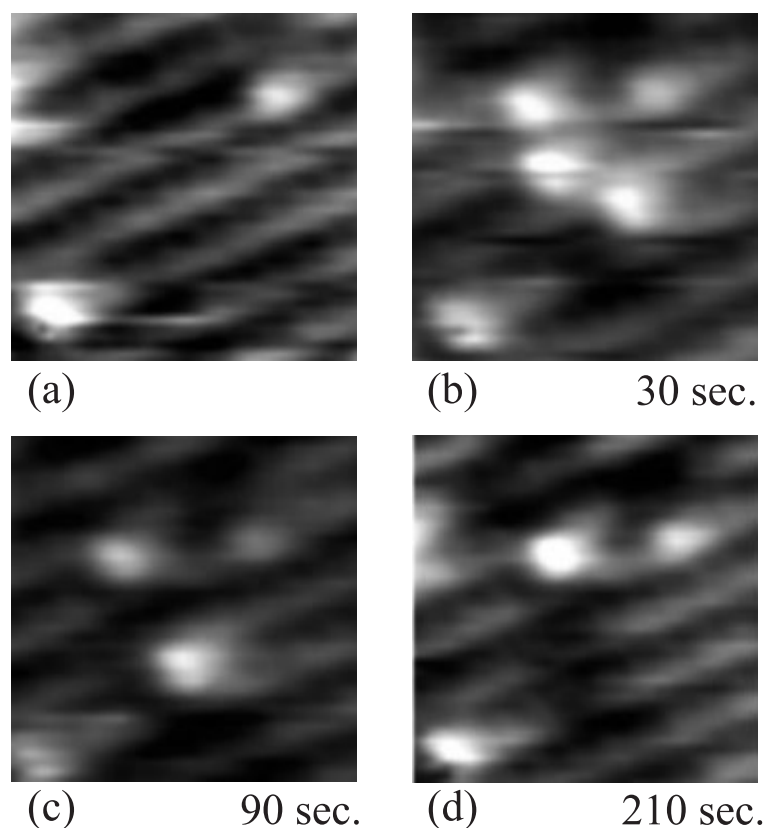


Figure 4.21: In situ observation of the reaction between O_{2f} and CO_{1f} . This series of images shows the same area after an exposure of 0.3 L CO. (a) Clean $RuO_2(110)$ surface. Indicated below each image is the elapsed time after the surface (a) was exposed to 0.3 L CO. $U_T = -0.6$ V, $I_T = 2.2$ nA. $35 \text{ \AA} \times 35 \text{ \AA}$.

a certain direction. Fig. 4.23b shows a mostly random distribution of vacancies. However, occasionally lines of vacancies perpendicular to the Ru_{1f} and Ru_{2f} rows are observed (indicated with arrows). These lines indicate that O_{2f} neighboring a vacancy perpendicular to the rows react with CO_{1f} more easily than randomly chosen O_{2f} atoms. Some attractive interaction between O_{2f} and CO_{1f} across the rows ($[\bar{1}10]$ direction) may play a role in this directionality.

In summary, the reaction between O_{2f} and CO_{1f} is predominantly statistical. Interactions between the O_{2f} atoms have thus little influence on the reactivity of the O_{2f} , so that the reaction events are independent of each other. The low mobility of the O_{2f} atoms also prevents a rearrangement of the O_{2f} layer during the reaction, which is much faster (calculated reaction barrier is just 0.7 eV [98, 102].) than the diffusion.

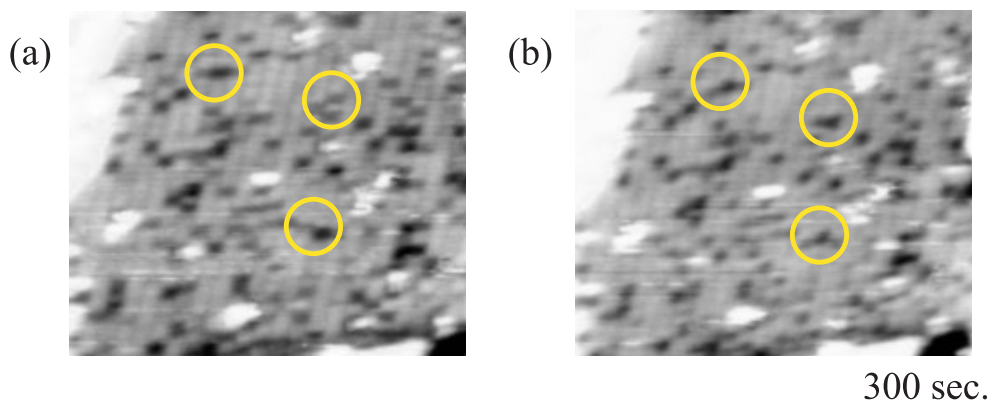


Figure 4.22: Diffusion of O_{2f} atoms. A clean RuO₂(110) surface is exposed to 0.8 L CO. The area where the diffusion of O_{2f} occurred is indicated by circles. U_T = -0.6 V, I_T = 2.2 nA. 145 Å × 130 Å.

Weak interactions between O_{2f} and CO_{1f} may lead to some preferential reactivity across the Ru_{1f} and Ru_{2f} rows. The general statistical nature of the reaction shows that defects of the RuO₂(110) surface do not represent active sites [96]. This is quite different from the TiO₂(110) surface, where defects are responsible for the reactivity [104].

Table 4.2: Hopping and desorption rates and estimated barriers for O and CO species on RuO₂(110). We assume 10¹³ s⁻¹ as the preexponential factor for diffusion and 10¹⁶ s⁻¹ for desorption according to [87]. The desorption rate is calculated as the time derivative of the coverage

Species	Coverage	Hopping rate (s ⁻¹)	E_{diff}^* (exp.)	E_{diff}^* (cal.) [87, 95]
O _{2f}	0.71	$(4.2 \pm 4.7) \times 10^{-5}$	1.00 eV	O _{1f} : 1.2 eV
CO _{2f}	0.72	$< 10^{-5}$	> 1.00 eV	
CO _{1f}	0.42	$(0.9 \pm 0.3) \times 10^{-3}$	0.93 eV	1.1 eV
CO _{1f}	0.22	$(4.0 \pm 0.8) \times 10^{-3}$	0.89 eV	
CO _{1f}	0.12	$(1.0 \pm 0.3) \times 10^{-3}$	0.92 eV	
Species	Coverage	Desorption rate (s ⁻¹)	E_{des}^* (exp.)	E_{des}^* (cal.) [87]
CO _{1f}	0.42	$(5.7 \pm 2.2) \times 10^{-5}$	1.14 eV	1.32 eV

The reaction between O_{1f} and CO_{2f} occurs in almost the same, statistical, way as the reaction between CO_{1f} and O_{2f}, for similar reasons.

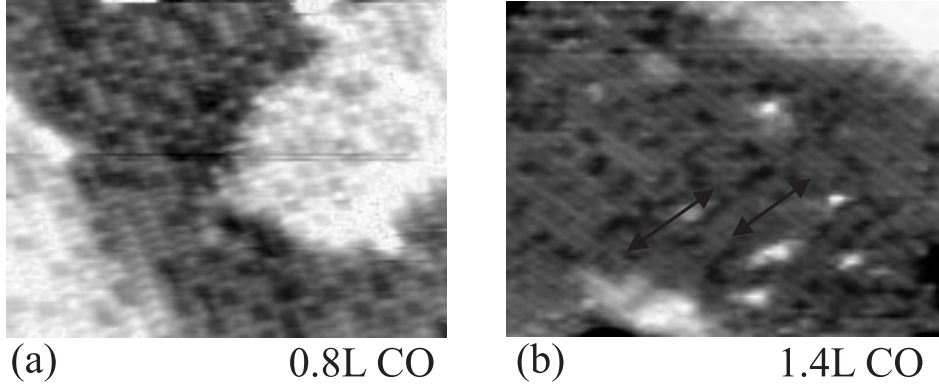


Figure 4.23: Predominantly statistical nature of the reaction between O_{2f} and CO_{1f} . (a) Random distribution of vacancies. $U_T = 0.6$ V, $I_T = 2.2$ nA, $115 \text{ \AA} \times 65 \text{ \AA}$. (b) Sometimes the reaction occurs preferentially perpendicular to the Ru_{1f} and Ru_{2f} rows (indicated with arrows). $U_T = -0.6$ V, $I_T = 2.2$ nA, $195 \text{ \AA} \times 120 \text{ \AA}$.

The measured hopping rate of CO_{2f} is even lower than the rate of O_{2f} (Table 4.2).

4.6.2 Reaction between O_{1f} and CO_{1f}

In general, the reactivity of adsorbates depends on the adsorption energy E_{ad} on the adsorption sites [123]. The value for E_{ad} of CO_{1f} can be obtained from the STM data. At high coverages, some CO_{1f} slowly desorbs as time goes on. From Fig. 4.24, the desorption rate is $(5.7 \pm 2.2) \times 10^{-5} \text{ s}^{-1}$ at $\theta_{CO_{1f}} = 0.42$ to 0.43 . Desorption of CO_{1f} can be assumed to be first order, and a preexponential factor k_o of 10^{16} s^{-1} can be assumed using the Redhead formula [87, 124]. With these values the desorption barrier for CO_{1f} E_{des}^* ($= E_{ad}$) becomes 1.14 eV from $-d\theta_{CO_{1f}}/dt = k_o\theta_{CO_{1f}}\exp(-E_{des}^*/k_B T)$. This value is reasonable considering the calculated value of 1.32 eV [87] (Table 4.2).

In contrast to O_{2f} , the interactions between CO_{1f} molecules are not negligible. The interactions are strong enough to form 1D rows perpendicular to the Ru_{1f} rows at low coverages (Fig. 4.25b) and to form (2×1) rectangular structures or $c(2 \times 2)$ quasi-hexagonal structures at high coverages (Fig. 4.19). The CO_{1f} molecules are about 100 times more mobile than O_{2f} (Fig. 4.25, Table 4.2). The mobility also depends on the coverage (Table 4.2). At intermediate coverage, the diffusion rate is maximum, which implies that the mobility is influenced by the interaction between CO_{1f} molecules. The dependence of

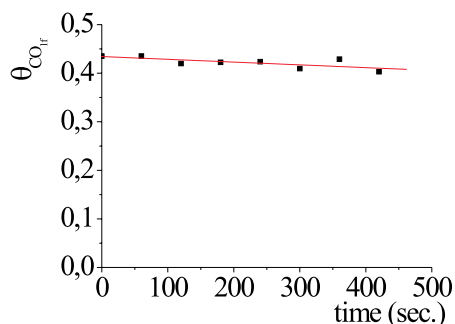


Figure 4.24: Desorption of CO_{1f} at high coverages.

mobility on the interaction between particles on the surface is a common phenomenon, and one explicit example can be found in [33]. As is in section 4.6.1, we estimate E_{diff}^* for CO_{1f} under the assumption of a preexponential factor 10^{13} (Table 4.2). They are 0.89 to 0.93 eV, and are reasonable considering the calculated E_{diff}^* for CO_{1f}, 1.1 eV [87].

Although CO_{1f} is more mobile and the interactions with each other are stronger than for O_{2f}, our data show that they still react *statistically*. Fig. 4.26 shows the reaction between CO_{1f} and O_{1f} while the surface is exposed to O₂ gas. Only CO_{1f} is resolved throughout the series. What we observe is the reduction of initially ordered CO_{1f} molecules. Note that the state of the STM tip is different from the tip used in Fig. 4.18, so that CO_{1f} is imaged as sitting on bright rows, not on dark rows. The row below CO_{1f} is imaged as a bright one or a dark one, according to the state of the STM tip.

The tip was not retracted here, differently from the other experiments in section 4.5. However, the shadow effect of the tip is small, because the reaction occurs overall on the surface. Shadow effects usually caused the reaction to start at one edge of the scanned area. In addition, the time to remove approximately the same number of CO_{1f} molecules as in the experiments with the tip retracted (section 4.5) was about the same here at the similar partial pressures of O₂. Therefore, we can be sure that the shadow effect was negligible.

At the initial state, CO_{1f} occupies nearly every second Ru_{1f} site. There are some sporadic vacancies in the superstructure (Fig. 4.26a). At the initial stage of the reaction, the reaction rate is low and the ordered initial superstructure of CO_{1f} remains almost intact (Fig. 4.26b). After this initial stage, the reaction rate becomes higher (Fig. 4.26c,

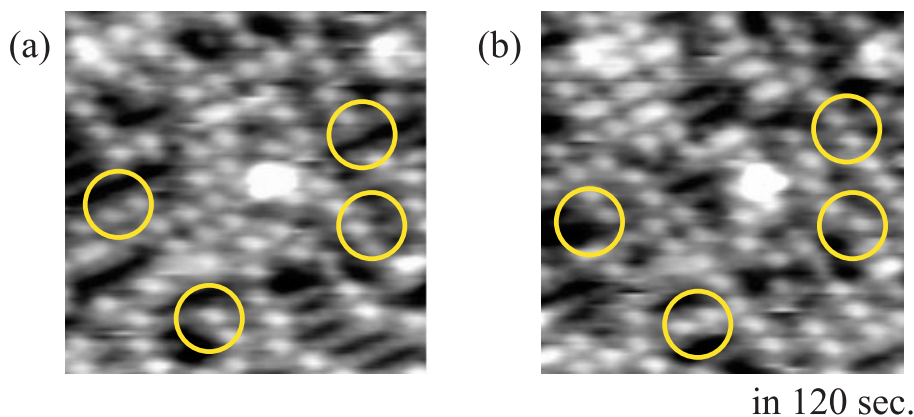


Figure 4.25: Hopping of CO_{1f} molecules at intermediate coverages ($\theta_{CO_{1f}} \sim 0.25$). (b) shows the same area as (a) after 120 sec. Some hopping events are indicated with circles. Compare the mobility of CO_{1f} with the mobility of O_{2f} in Fig. 4.22. $U_T = -0.6$ V, $I_T = 2.2$ nA. $63 \text{ \AA} \times 63 \text{ \AA}$.

d). Overall the reaction seems to be random. In addition, another type of bright feature is observed during the reaction. In Figs. 4.26 b–d, brighter dots than the dots at the initial stage in Fig. 4.26a are observed (an example is indicated with an arrow in Fig. 4.26c). They may be an intermediate product during the reaction or carbonates [125].

When CO_{1f} forms a superstructure with nearly maximum coverage of 0.5 as is in Fig. 4.26a, O_2 can adsorb only in defects in the superstructure. This is because O_2 needs two neighboring adsorption sites for dissociative adsorption. Therefore, the reaction should begin from vacancies, where O_2 can adsorb dissociatively. Fig. 4.27 shows the processes in greater detail. The initial state is the nearly perfect (2×1) superstructure of CO_{1f} that has some vacancies. The circle shows the evolution of one such vacancy from the beginning. After 70 seconds, sites around the vacancy have reacted, indicating that the reaction starts at vacancies (Fig. 4.27b). Then the vacancy grows further. In particular, we observe that the vacancy grows perpendicular to the rows (Figs. 4.27c, d, indicated with arrows). At the same time, a gray feature occurs in the initial vacancy, indicating that it has become filled by O_{1f} (Fig. 4.27c, circle). After this induction period the ordered CO_{1f} adlayer quickly disappears. In this stage, there are enough sites for O_2 to dissociate, so that most of the CO_{1f} molecules are accessible to O_{1f} .

Table 4.3 shows the quantitative analysis. Thanks to the high quality of the images in Fig. 4.26, we can count the CO molecules at the

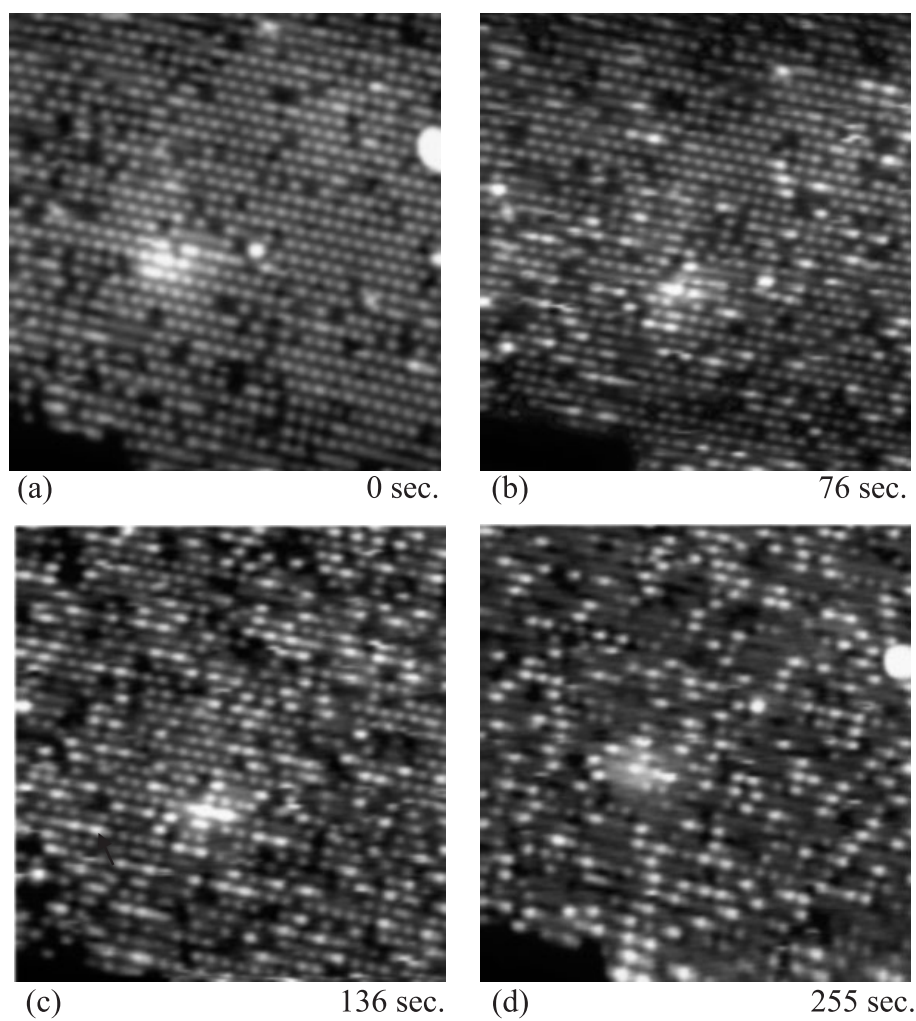


Figure 4.26: In situ observation of the reaction between CO_{1f} and O_{1f} . This series of images shows the same area. $P_{\text{O}_2} = 2 \times 10^{-8}$ Torr. Dots are CO_{1f} . There appears another type of dots which are brighter than CO_{1f} during the reaction. One example is indicated with an arrow in (c). Indicated below each image is the elapsed time after the exposure. $U_T = 0.6$ V, $I_T = 2.2$ nA. $160 \text{ \AA} \times 180 \text{ \AA}$.

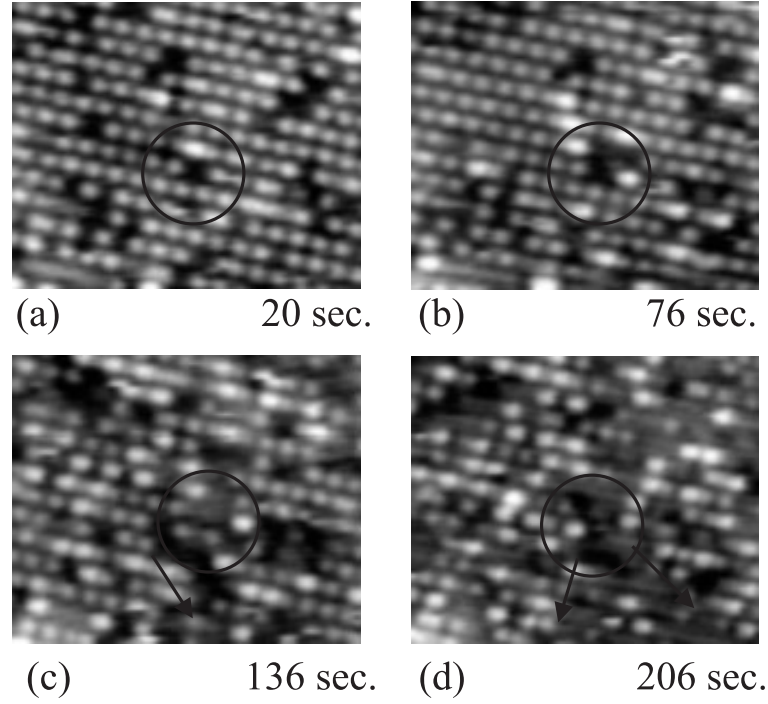


Figure 4.27: Details from Fig. 4.26. The series shows the same area during exposure to O_2 . The vacancy indicated with a circle in (a) grows across the Ru_{1f} and Ru_{2f} rows as shown in (c) and (d). $U_T = 0.6$ V, $I_T = 2.2$ nA. $90 \text{ \AA} \times 70 \text{ \AA}$.

ends of the CO_{1f} rows (CO_{1f_end}) and in the rows (CO_{1f_in}) during the reaction. In the beginning of the reaction, the reaction rate is correlated with $\theta_{CO_{1f_end}}$, not with $\theta_{CO_{1f}}$ or $\theta_{CO_{1f_in}}$. It means that the reaction occurs indeed at the ends of the CO_{1f} rows, i.e. at the vacancies in the beginning.

Table 4.3: Reaction rate between CO_{1f} and O_{1f} and estimated activation barrier of the reaction. We assume 10^{13} as a preexponential factor. Reaction rate is calculated as the time derivative of $\theta_{CO_{1f}}$

$\theta_{CO_{1f}}$	$\theta_{CO_{1f_in}}$	$\theta_{CO_{1f_end}}$	Reaction rate ($\times 10^{-3} s^{-1}$)	E_{reac}^* (exp.)	E_{reac}^* (cal.) [126]
0.40	0.26	0.14	1.1	0.87 eV	0.62 eV
0.29	0.14	0.15	2.3		
0.17	0.05	0.12	1.8		
0.09	0.02	0.07	0.6		

From these findings, the reaction between CO_{1f} and O_{1f} proceeds

as follows. The reaction starts at vacancies. In this stage, the reaction rate is low, because only O₂ molecules adsorbing in sporadic vacancies can react with CO_{1f}. The reaction rate then becomes larger as more empty sites become available for O₂ to adsorb, and most of the CO_{1f} molecules are accessible to adsorbed O_{1f}. The distribution of CO_{1f} during the reaction is random and CO_{1f} is not so mobile compared to the reaction rate (Table 4.2, Table 4.3). Therefore, the reaction occurs almost statistically between CO_{1f} and O_{1f}.

This two-step reaction mechanism also becomes apparent in the time evolution of $\theta_{\text{CO}_{1f}}$ (Fig. 4.28a). There is a kink in the graph at ~ 70 seconds (indicated with A). After the kink, the decrease rate of $\theta_{\text{CO}_{1f}}$ becomes higher. The double logarithmic plot of the reaction rate after the kink vs $\theta_{\text{CO}_{1f}}$ falls on a straight line with a slope of 1.0 ± 0.3 (Fig. 4.28b), i.e., the reaction appears to follow a simple first-order kinetics. At later stages of the reaction (after A), practically all CO_{1f} is accessible to O_{1f}, and most of the CO_{1f} molecules have potential O_{1f} reaction partners on neighboring sites for the following reason. Partial pressure of O₂ in Fig. 4.26 is 2×10^{-8} Torr. From the kinetic theory of dilute gases, the surface impact rate of O₂ molecule is $9.7 \times 10^{12} \text{ cm}^{-2} \text{ s}^{-1}$ [127]. If we assume the sticking coefficient (s) of O₂ on RuO₂(110) as 1, it takes ~ 25 seconds for O_{1f} atoms to reach one monolayer. s is believed to be near 1, considering effective reacting off of CO_{1f} with O_{1f} in Figs. 4.18 h–j. This adsorption rate of O₂ is much higher than the reaction rate, considering that the reaction takes place in the order of 100 seconds (Fig. 4.28a). This situation is consistent with the many vacancy defects in the later stage of the reaction. A reaction order of 1 thus agrees with the almost statistical reaction.

Under these conditions the reaction barrier between CO_{1f} and O_{1f} (E_{reac}^*) can be estimated using the Arrhenius law. Again, we assume 10^{13} as a preexponential factor k_o . Then, the reaction kinetics can be written as

$$-\frac{d\theta_{\text{CO}_{1f}}}{dt} = k' \cdot \theta_{\text{CO}_{1f}}, \quad k' = k_o \cdot \theta_{\text{O}_{1f}}^n \cdot \exp(-E_{\text{reac}}^*/k_B T), \quad (4.6)$$

where the reaction rate is not limited by the adsorption rate of O₂ (after A in Fig. 4.28a). $\theta_{\text{O}_{1f}}$ is between 0.5 to 0.9, but it can be regarded as a constant because O atoms are abundant, and therefore $\theta_{\text{O}_{1f}}$ is not rate limiting factor (section 3.7.2). As in section 3.7.2, k' is obtained from the integrated form of Eq. (4.6), and is $(4.5 \pm 0.8) \times 10^{-3} \text{ s}^{-1}$. This value corresponds to an activation energy of 0.87 eV (Table 4.3).

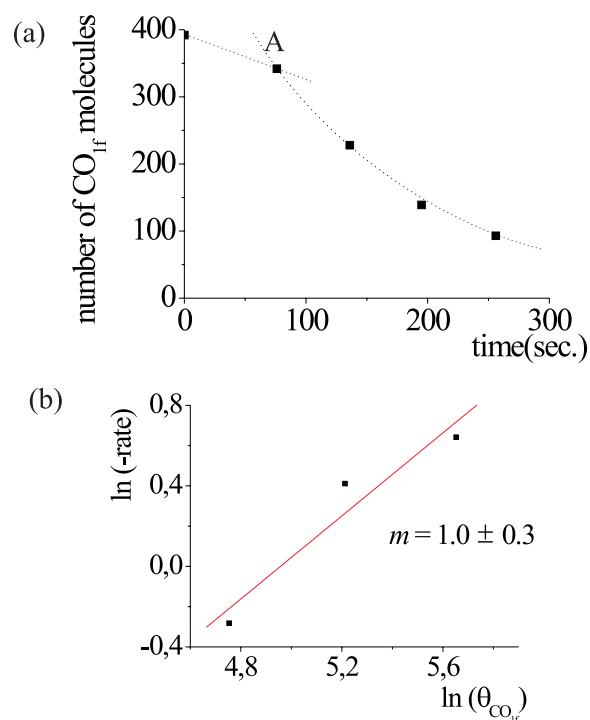


Figure 4.28: Reaction order of the reaction between CO_{1f} and O_{1f}. (a) Time evolution of $\theta_{\text{CO}_{1f}}$. There is one kink at ~ 70 sec. in the graph. Dotted lines are eye guides. (b) Reaction order m after the kink. $m \sim 1$ shows that the reaction occurs statistically.

The value is somewhat larger than the calculated value for the reaction (0.62 eV) [126]. However, this calculation does not consider exactly the same situation because Ru_{2f} rows are covered with O_{2f}, not with CO_{2f} as in the experiment.

4.6.3 Summary of section 4.6

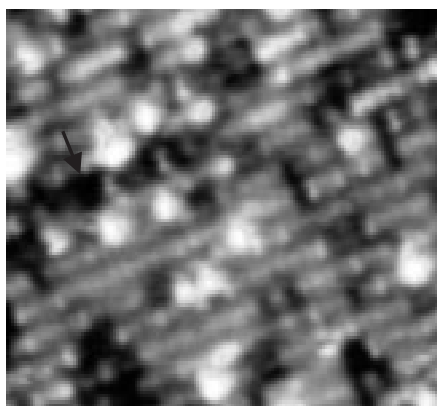
The analysis of the diffusion of CO and O on RuO₂(110) shows that the hopping rates of O_{2f} and CO_{2f} are very low ($\sim 10^{-5} \text{ s}^{-1}$). The estimated diffusion barrier for O_{2f} is 1.00 eV. The hopping rate of CO_{1f} is higher and depends on $\theta_{\text{CO}_{1f}}$. At intermediate coverages ($\theta_{\text{CO}_{1f}} \sim 0.25$), the hopping rate is highest. Estimated diffusion barriers for CO_{1f} are 0.89 to 0.93 eV. The reaction of O_{2f} on the stoichiometric surface with CO_{1f} is largely random. Defects do not represent active sites.

The same holds for the reaction between CO_{1f} and O_{1f}. Estimated barriers for the reaction between CO_{1f} and O_{1f} are ~ 0.87 eV. When the initial $\theta_{\text{CO}_{1f}}$ is near the maximum coverage of 0.5, the reaction is no longer random, because there are not enough adsorption sites for O₂ to adsorb dissociatively. Under these conditions, the reaction occurs at the vacancies in the CO_{1f} superstructure. After $\theta_{\text{CO}_{1f}}$ has become lower than 0.40 in this way, practically all CO_{1f} molecules have enough empty sites around them, and the reaction between CO_{1f} and O_{1f} occurs statistically. The graph $\theta_{\text{CO}_{1f}}$ vs. time shows a kink that indicates the change of the reaction mechanism. After the kink, the reaction order m is 1, consistent with the statistical nature of the reaction.

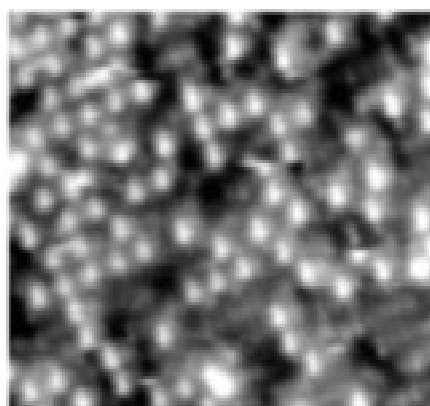
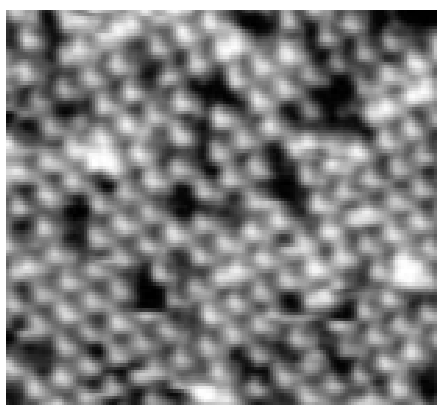
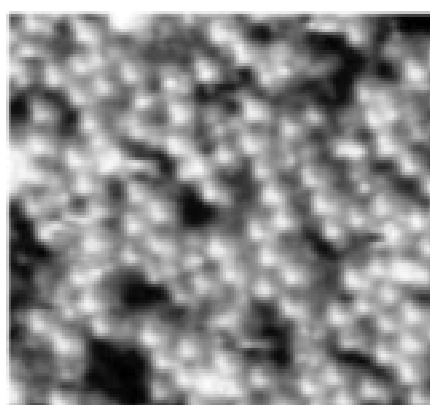
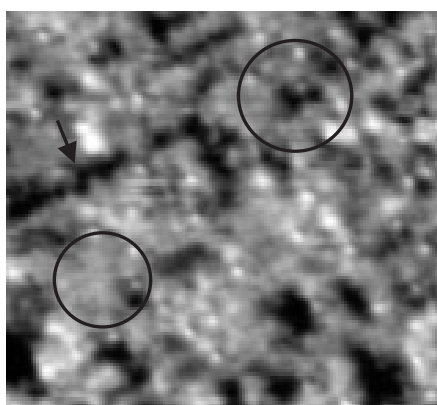
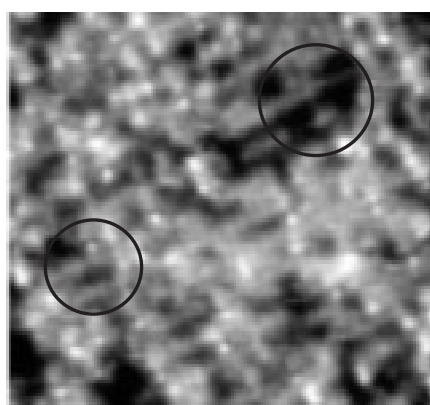
4.7 Reversibility of the reaction and steady-state conditions

The reversibility of the CO oxidation reaction on RuO₂(110) was checked by subsequent adsorption experiments with CO and O₂. Fig. 4.29 shows an example with two such cycles.

Fig. 4.29a shows the RuO₂(110) surface exposed to ~ 4 L CO. Parts of the Ru_{2f} rows (bright rows) are covered with CO, and there are also some CO_{1f} molecules (white dots on dark rows). The RuO₂(110) surface was further exposed to CO ($P_{\text{CO}} = 5 \times 10^{-8}$ Torr) until saturation, $\theta_{\text{CO}_{1f}} \sim 0.5$ (Figs. 4.29b, c). The saturated RuO₂(110) surface with CO was then exposed to O₂ ($P_{\text{O}_2} = 5 \times 10^{-8}$ Torr) and observed until the surface is covered with O atoms again (Fig. 4.29d, e). Fig. 4.29e shows this state. Most of the Ru_{1f} rows (dark rows) are filled with adsorbed O atoms, although the filling is not complete. The oxygen saturated RuO₂(110) surface was then again exposed to CO ($P_{\text{CO}} = 5 \times 10^{-8}$ Torr) until saturation (Figs. 4.29 f–h). In the beginning, CO adsorbs on vacancies in Ru_{1f} rows and reacts off with O_{1f} (Figs. 4.29e, f, indicated with circles). Simultaneously, adsorbing CO reacts with O_{2f} and finally the surface is saturated again with CO (Figs. 4.29g, h). Although the partial pressure of CO is the same as during the first exposure, it takes about twice as long time for adsorbed CO to reach the saturated state, because O_{1f} and O_{2f} must be reacted off first. The once again saturated RuO₂(110) surface with CO appears essentially identical to the previously CO saturated surface (Fig. 4.29c), except that $\theta_{\text{CO}_{1f}}$ in fig 4.29h is lower than in Fig. 4.29c ($\theta_{\text{CO}_{1f}} = 0.43$ vs. 0.38).



(a)

(b) $P_{\text{CO}} = 5 \times 10^{-8}$ Torr 232 sec.(c) $P_{\text{CO}} = 5 \times 10^{-8}$ Torr 350 sec.(d) $P_{\text{O}_2} = 5 \times 10^{-8}$ Torr 187 sec.(e) $P_{\text{O}_2} = 5 \times 10^{-8}$ Torr 370 sec.(f) $P_{\text{CO}} = 5 \times 10^{-8}$ Torr 170 sec.

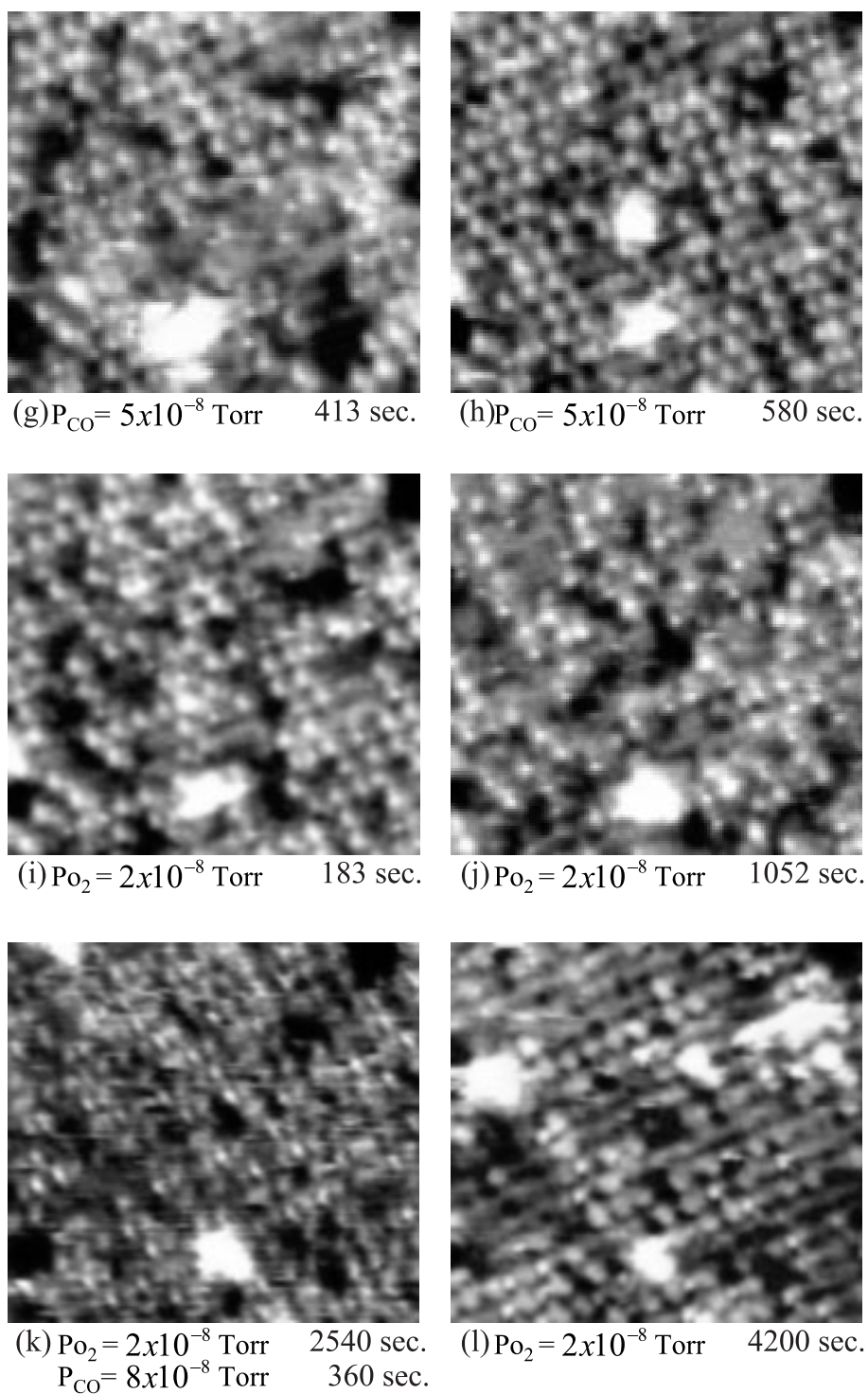


Figure 4.29: In situ observation of the reaction between CO_{1f} and O_{1f} on RuO₂(110) during cycles of CO and O₂ exposure and under steady-state conditions. The images show the *same* area throughout the whole series. $U_T = -0.6$ V, $I_T = 2.2$ nA. $95 \text{ \AA} \times 90 \text{ \AA}$.

After repeating the O_2 exposure, a few white dots remain on the surface similar to the CO dots in Fig. 4.26c (Fig. 4.29j). Here they cannot be caused by CO_{1f} , because of the massive O_2 exposure. They might be carbonates or some other modification of the surface that is unreactive (cf. Fig. 4.29j and f).

Hence, the $RuO_2(110)$ surface essentially shows reversibility between the CO saturated state and the O saturated state, but some irreversible effects seem to accumulate. Of course, such irreversible effects may become important under steady-state reaction conditions, when both CO and O_2 simultaneously adsorb on the surface (Figs. 4.29k, l).

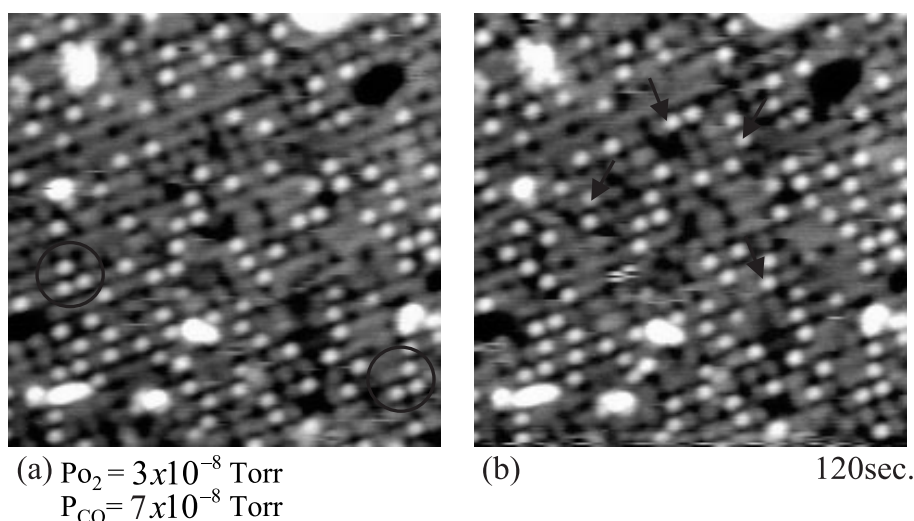


Figure 4.30: Inactive $RuO_2(110)$ to CO after the surface is massively exposed to O_2 . When $RuO_2(110)$ is exposed to massive O_2 (~ 110 L), white dots are still observed. During O_2 exposure, occasionally the surface is also massively exposed to CO (total amount of ~ 160 L). The images show the same area during exposure of CO and O_2 together. Some adsorption events are indicated with arrows in (b). Physical properties of the white dots are different from those of CO_{1f} (Table 4.4). $U_T = -0.6$ V, $I_T = 2.2$ nA. $110 \text{ \AA} \times 110 \text{ \AA}$.

When P_{O_2} is still 2×10^{-8} Torr and P_{CO} is 8×10^{-8} Torr, we observe that CO_{1f} appears again (Fig. 4.29k) up to $\theta_{CO_{1f}} \sim 0.30$. The superstructure of CO_{1f} does *not* appear to be different from the superstructure of CO_{1f} under CO pressure only or during titration. When the partial pressure of CO is again reduced to zero, the number of dots decreases (Fig. 4.29l). Again, it is not sure whether these features are CO_{1f} s or other species, because no CO molecules should

remain on the RuO₂(110) surface under these conditions. Because CO_{1f} under steady-state conditions forms the same superstructure as in the titration experiments in sections 4.5 and 4.6, it is concluded that the reaction mechanism between CO_{1f} and O_{1f} under *steady-state* condition is the same.

Table 4.4: Hopping, desorption, and adsorption rate of the white dots after the RuO₂(110) surface is massively exposed to O₂ and CO. They are measured from series of images like one in Fig. 4.30. Desorption (adsorption) rates are calculated as the ratio of the number of desorbed (adsorbed) dots to the total number of dots. $\theta_{\text{dot}} = 0.11 \sim 0.17$

Pressure ($\times 10^{-8}$ Torr)	Hopping rate ($\times 10^{-4} \text{s}^{-1}$)	Desorption rate ($\times 10^{-4} \text{s}^{-1}$)	Adsorption rate ($\times 10^{-4} \text{s}^{-1}$)
P _{O₂} = 3 P _{CO} = 0	16 ± 4	26 ± 6	21 ± 6
P _{O₂} = 3 P _{CO} = 7	2.4 ± 2.4	8.7 ± 4.3	6.9 ± 2.9
P _{O₂} = 3 P _{CO} = 20	0.8 ± 0.8	3.8 ± 2.4	4.9 ± 0.9
P _{O₂} = 0 P _{CO} = 20	1.4 ± 1.0	3.6 ± 1.0	2.9 ± 1.0
P _{O₂} = 0 P _{CO} = 0	0.7 ± 0.7	2.2 ± 1.8	< 0.1

As already mentioned, during repeated exposures to CO and O₂, the surface shows irreversible changes that tend to accumulate (Fig. 4.29). When the oxide surface is massively exposed to O₂ and CO, additional white dot features occur (Fig. 4.30). The dots occasionally form a (2 × 1) superstructure (indicated with circles in Fig. 4.30a), similar to the CO_{1f} molecules. However, for the following reason it is ruled out that these additional features are due to CO_{1f}. Table 4.4 shows hopping, desorption, and adsorption rates of the white dots during exposure to O₂ alone (first row), to CO alone (fourth row), during exposure of CO and O₂ together (second, third rows), and after pumping to UHV pressures (last row). The dot coverage (θ_{dot}) during the exposure experiment remained at 0.11 ~ 0.17. Because the mobility of the dot is very low under UHV conditions, we could distinguish the hopping events from desorption or adsorption events during the gas exposures. For example, some adsorption events are indicated with arrows in Fig. 4.30b.

Under most conditions (rows 2 ~ 5 in Table 4.4), the hopping rates of the white dots are much lower than that of CO_{1f} (Table 4.2). The negligible adsorption rate after pumping down shows that the dots are not any adsorbate from the rest gas in the chamber. When the surface is exposed to O₂ alone (first row), the hopping rate increases by one order of magnitude to a value as high as that of CO_{1f}, the most mobile species on RuO₂(110). In addition, desorption and adsorption rates also become high, indicating some interaction with O₂. The two rates are similar to each other, so that θ_{dot} remains constant during the exposure. Constant θ_{dot} means that the dots are *not reactive* with adsorbing O₂. This enhanced dynamics of the dot becomes weaker when the surface is additionally exposed to CO (second, third rows). Under these conditions, the lower mobility of the dots correlates with a higher partial pressure of CO. When the surface is exposed to CO only, the mobility of the dot is as low as that under UHV, whereas the adsorption rate is slightly higher than that under UHV. This behavior indicates that the dots are *not reactive* with adsorbing CO, either.

These observations indicate a close relation of the white dot features with oxygen. In an O₂ atmosphere these features are mobile and adsorb and desorb, whereas they are practically unaffected by adsorbing CO. Because it does not seem that contaminants play a role, a massive exposure to O₂ may cause some structural change of the RuO₂(110) surface. An ongoing study of RuO₂(110) under a high partial O₂ pressure of up to 200 mbar is investigating this problem in our group [128]. Another possibility is that some other species than CO or O is involved. For example, carbonate has been observed after high O₂ doses in a HREELS experiment [125].

The built-up of these species could explain the observation of a very low steady-state CO₂ production rate on RuO₂(110) at room temperature [90]. In this study it was found that significant CO₂ production could only be obtained by heating the sample to ~ 350 K. It was concluded that at room temperature the surface is poisoned by carbonate, which desorbs at slightly higher temperatures.

4.8 Summary

Mesoscopic and microscopic investigations about the morphology of RuO₂(110) oxide films grown on Ru(0001)

The mesoscopic morphology of RuO₂(110) oxide films grown between 650 K and 900 K shows a strong dependence on the preparation temperature (T_{prep}). The growth of the oxide film is mostly kinetically determined at $T_{\text{prep}} \sim 650$ K, and thermodynamic effects become more important as T_{prep} is increased to 900 K. The thickness of the oxide film is independent of T_{prep} , and it ranges between 7 Å and 15 Å, i.e. 2 to 5 oxide (Ru-O) monolayers. Monolayer high oxide films are occasionally observed, and they already display the surface structure of thicker oxide films. Partial evaporations of the oxide film by flashing the sample to various temperatures reveal the thermodynamic stability of its morphology. The film does not evaporate layer by layer, but holes emerge in the oxide film. The holes go entirely down to the substrate, once they have reached a certain size, while the thickness of the other part of the film is unchanged. The holes have a characteristic shape. They form parallelograms or rectangles and they are longer in [001] direction. The surface free energy γ_{001} of the side of a hole in [001] direction is 2 to 5 times higher than the surface free energy of the perpendicular side γ_{110} . Furthermore, the energy of a (001) side is about equal to that of a side $\sim 65^\circ$ inclined to this direction. The morphology of the Ru(0001) substrate in the proximity of the oxide film does not differ from clean Ru(0001). When the oxide film is evaporated, the dissolved Ru atoms from the evaporating oxide film remain on the substrate and form a complicated terrace morphology with hexagonal or circular Ru islands.

Microscopic investigations about the physical and chemical processes during CO oxidation on the RuO₂(110) surface

When the stoichiometric RuO₂(110) is exposed to CO at room temperature, CO adsorbs on Ru_{1f} atoms. Adsorbed CO_{1f} reacts off readily with neighboring O_{2f}, and a vacancy occurs in the O_{2f} row. CO_{1f} occupies the vacancy, forming CO_{2f}. In the course of the reaction, the Ru_{2f} rows are thus completely filled with CO (CO_{2f}). CO_{2f} sits on Ru_{2f} rows as densely as O_{2f}, i.e., the maximum $\theta_{\text{CO}_{2f}}$ is 1, so that a (1 × 1) superstructure is formed. After saturation of the Ru_{2f} rows

with $\text{CO}_{2\text{f}}$, CO occupies $\text{Ru}_{1\text{f}}$ sites. The maximum $\theta_{\text{CO}_{1\text{f}}}$ is 0.5, and ordered superstructures are mostly (2×1) , $c(2 \times 2)$, and very small (1×1) units. When this CO saturated $\text{RuO}_2(110)$ is exposed to O_2 , dissociatively adsorbed O atoms on $\text{Ru}_{1\text{f}}$ rows ($\text{O}_{1\text{f}}$) react with $\text{CO}_{1\text{f}}$, and vacancies occur in the $\text{CO}_{1\text{f}}$ superstructure. Simultaneously, $\text{O}_{1\text{f}}$ reacts with $\text{CO}_{2\text{f}}$ and vacancies occur also in the $\text{CO}_{2\text{f}}$ rows. $\text{O}_{1\text{f}}$ atoms occupy the vacancies, forming $\text{O}_{2\text{f}}$ again. In this way, $\text{O}_{2\text{f}}$ restores the (1×1) superstructure. When the surface is further exposed to O_2 , O atoms occupy $\text{Ru}_{1\text{f}}$ rows, forming locally $\text{O}_{1\text{f}}$ (1×1) superstructures.

The analysis of these experiments yields values for diffusion barriers (E_{diff}^*) and desorption barriers (E_{des}^*) of the various adsorbed species, and effective reaction barriers (E_{reac}^*) between $\text{CO}_{1\text{f}}$ and $\text{O}_{1\text{f}}$. The values (Table below) are based on preexponential factors of 10^{13} s^{-1} for diffusion and reaction, and of 10^{16} s^{-1} for desorption. While the E_{diff}^* and E_{des}^* is lower than results from DFT calculations, E_{reac}^* is higher than the calculated values.

Species	E_{diff}^* (eV)
$\text{O}_{2\text{f}}$	1.00
$\text{CO}_{2\text{f}}$	> 1.00
$\text{CO}_{1\text{f}}$	0.89 to 0.93
Species	E_{des}^* (eV)
$\text{CO}_{1\text{f}}$	1.14
Reaction	E_{reac}^* (eV)
$\text{CO}_{1\text{f}} + \text{O}_{1\text{f}}$	0.87

The reaction between $\text{O}_{2\text{f}}$ and $\text{CO}_{1\text{f}}$, between $\text{O}_{1\text{f}}$ and $\text{CO}_{2\text{f}}$, and between $\text{O}_{1\text{f}}$ and $\text{CO}_{1\text{f}}$ are mostly statistical. However, some preferential reaction perpendicular to the Ru rows was occasionally observed.

Under steady-state reaction conditions, CO can adsorb in the presence of O_2 , provided that the partial pressure of CO is high enough. The $\text{CO}_{1\text{f}}$ superstructure under the condition is the same as that under CO pressure or in CO titration experiments. When the surface is exposed to larger quantities of O_2 and CO ($\sim 100 \text{ L}$), white dots similar to $\text{CO}_{1\text{f}}$ are observed on the surface. However, they do not react with either O_2 or CO. This observation suggests that the chemical property of the oxide surface in this state is different from that of the clean $\text{RuO}_2(110)$ surface at the beginning.

Chapter 5

Conclusions

The aim of this thesis was to apply the demonstrated ability of STM to investigate the *reaction mechanisms* to more *complicated* reactions. For this purpose, the oxidation of CO on two surfaces was investigated, Pd(111) and RuO₂(110)/Ru(0001). Structural analyses of the O-, CO-, and (CO+O) adlayers on Pd(111) and on RuO₂(110)/Ru(0001) reveal the microscopic distributions of the adsorbates on the surfaces. By means of time dependent quantitative analyses of the reactions the reaction kinetics and the reaction mechanisms were revealed. Detailed summaries of the results are in section 3.9 and 4.8.

Comparison between CO oxidation on Pd(111) and on RuO₂(110)/Ru(0001)

The different reaction mechanisms for CO oxidation on Pd(111) and on RuO₂(110) can be traced back to the different electronic structures of the two surfaces.

On Pd(111) the electronic states at the surface are very delocalized so that adsorbates can easily diffuse between different adsorption sites. This ‘smooth’ electronic structure is reflected by low E_{diff}^* s for O and CO. Values measured in this work are ~ 0.54 eV and ~ 0.15 eV, respectively. Therefore, superstructures and reactivities of O and CO on Pd(111) are to a considerable part determined by interactions between the adsorbates. When the initial (2×2) -O adlayer on Pd(111) with $\theta_{\text{O}} = 0.25$ is exposed to CO, the adlayer is compressed by the repulsive action of CO until (2×1) islands with $\theta_{\text{O}} = 0.5$ are formed. Adsorbed CO molecules first form $(\sqrt{3} \times \sqrt{3})$ R30°-CO islands with $\theta_{\text{CO}} = 0.33$, in a later stage a $c(4 \times 2)$ superstructure with $\theta_{\text{CO}} = 0.5$ due to repulsive interactions. By this compression the reactivity of O atoms increases

so that the initially unreactive O atoms in the (2×2) -O adlayer become highly reactive in the (2×1) islands. The high reactivity is reflected by low E_{reac}^* for the reaction, which is estimated in this work as 0.41 eV.

On the $\text{RuO}_2(110)$ the electronic states at the surface are localized, forming some kind of dangling bond at every adsorption site. Consequently, adsorbates on $\text{RuO}_2(110)$ are much less mobile than on $\text{Pd}(111)$, which is reflected by high E_{diff}^* s for O and CO. Measured values are between 0.9 and 1.0 eV. Therefore, superstructures and reactivities of O and CO on $\text{RuO}_2(110)$ are much more determined by their bonding to the substrate, rather than by interactions between them. Superstructures of O and CO on $\text{RuO}_2(110)$ do not undergo any compressions, and the reactivity of an individual adsorbate is not significantly influenced by neighboring adsorbates. Consequently, reactions mainly occur statistically. Estimated E_{reac}^* for the reaction between CO_{1f} and O_{1f} in this work is 0.87 eV. Under steady-state conditions, the superstructure of adsorbed CO is the same as that observed in the titration experiments, implying that the reaction mechanism under steady-state conditions is also mainly a statistical one. In this sense, the $\text{RuO}_2(110)$ surface is closer to the ideal ‘checker board’ surface suggested by I. Langmuir [129]. However, under heavy exposures to O_2 and CO, adsorbates with physical and chemical properties different from those of CO or O are observed on the $\text{RuO}_2(110)$ surface. Therefore, it is still an open question whether these results obtained under UHV conditions can be applied to conditions of technical catalysts.

Bibliography

- [1] G. Ertl, H. Knözinger, and J. Weinkamp (Eds). *Handbook of Heterogeneous Catalysis*. Wiley-VCH, Weinheim (1997).
- [2] J. Wintterlin. *Adv. Catal.*, **45**, 131 (2000).
- [3] J. Wintterlin, S. Völkening, T. V. W. Janssens, T. Zambelli, and G. Ertl. *Science*, **278**, 1931 (1997).
- [4] S. Völkening. *Untersuchungen von Reaktionsmechanismen auf Oberflächen mittels Rastertunnelmikroskopie - Die atomar aufgelösten Oxidationsreaktionen von Kohlenmonoxid und Wasserstoff*. Ph.D. thesis, Freie Universität Berlin (1999). [Http://www.diss.fu-berlin.de/1999/10/](http://www.diss.fu-berlin.de/1999/10/).
- [5] C. T. Cambell, G. Ertl, H. Kuipers, and J. Segner. *J. Chem. Phys.*, **73**, 5862 (1980).
- [6] T. Engel and G. Ertl. *Adv. Catal.*, **28**, 1 (1978).
- [7] T. Engel and G. Ertl. In *The Chemical Physics of Solid Surfaces and Heterogeneous Catalysis*. Elsevier, Amsterdam (1982).
- [8] H. Conrad, G. Ertl, and J. Küppers. *Surf. Sci.*, **76**, 323 (1978).
- [9] H. Over, Y. D. Kim, A. P. Seitsonen, S. Wendt, E. Lundgren, M. Schmid, P. Varga, A. Morgante, and G. Ertl. *Science*, **287**, 1474 (2000).
- [10] J. H. Xu, T. Jarlborg, and A. J. Freeman. *Phys. Rev. B*, **40**, 7939 (1989).
- [11] C. J. Chen. *Introduction to Scanning Tunneling Microscopy*. Oxford University Press, New York (1993).
- [12] H. J. Güntherodt and R. Wiesendanger, eds. *Scanning Tunneling Microscopy I*. Springer, Berlin (1992).

- [13] J. A. Stroscio and W. J. Kaiser, eds. *Scanning Tunneling Microscopy*. Academic Press, San Diego, CA (1993).
- [14] G. Binnig, H. Rohrer, C. Gerber, and E. Weibel. *Phys. Rev. Lett.*, **49**, 57 (1982).
- [15] G. Binnig and H. Rohrer. *Helv. Phys. Acta.*, **55**, 726 (1982).
- [16] J. Tersoff and D. R. Hamann. *Phys. Rev. Lett.*, **50**, 1998 (1983).
- [17] J. Tersoff and D. R. Hamann. *Phys. Rev. B*, **31**, 805 (1985).
- [18] T. Gritsch. Ph.D. thesis, Freie Universität Berlin (1990).
- [19] A. Steltenpohl and N. Memmel. *Surf. Sci.*, **443**, 13 (1999).
- [20] K. Besocke. *Surf. Sci.*, **181**, 145 (1987).
- [21] J. Frohn, J. F. Wolf, K. Besocke, and M. Teske. *Rev. Sci. Instrum.*, **60**, 1200 (1989).
- [22] T. Zambelli. *Dissoziationsvorgänge, Diffusion und Phasenbildung bei der Adsorption an Oberflächen: Untersuchungen mit dem Rastertunnelmikroskop*. Ph.D. thesis, Freie Universität Berlin (1996).
- [23] J. Méndez, S. H. Kim, J. Wintterlin, and G. Ertl. *in preparation*.
- [24] J. Wintterlin. *Struktur und Reaktivität einer Oberfläche - Eine Untersuchung mit dem Rastertunnelmikroskop am System Al(111)/Sauerstoff*. Ph.D. thesis, Freie Universität Berlin (1988).
- [25] J. Wiechers. *Aufbau eines Ultrahochvakuum-Rasterkraftmikroskops und erste Messungen an oxidischen Proben*. Ph.D. thesis, Ludwig-Maximilians-Universität München (1993).
- [26] S. Renisch. *Zur Diffusion adsorbierter Teilchen auf Einkristalloberflächen: Dynamische Untersuchungen mit dem Rastertunnelmikroskop*. Ph.D. thesis, Freie Universität Berlin (1999). [Http://www.diss.fu-berlin.de/1999/52/](http://www.diss.fu-berlin.de/1999/52/).
- [27] J. Wintterlin, J. Trost, S. Renisch, R. Schuster, T. Zambelli, and G. Ertl. *Surf. Sci.*, **394**, 159 (1997).

- [28] Y. D. Kim, A. P. Seitsonen, and H. Over. *Surf. Sci.*, **465**, 1 (2000).
- [29] S. Schwegmann. *Strukturuntersuchungen zur Wechselwirkung und Reaktion von Sauerstoff und Kohlenmonoxid auf Rhodium- und Ruthenium-Einkristalloberflächen*. Ph.D. thesis, Freie Universität Berlin (1997).
- [30] S. Wendt. *Komplexe Redox-Chemie auf der RuO₂(110)-Oberfläche*. Ph.D. thesis, Freie Universität Berlin (2002).
- [31] A. P. Seitsonen, Y. D. Kim, S. Schwegmann, and H. Over. *Surf. Sci.*, **468**, 176 (2000).
- [32] D. L. Weissman, M. L. Shek, and W. E. Spicer. *Surf. Sci.*, **92**, L59 (1980).
- [33] S. Renisch, R. Schuster, J. Wintterlin, and G. Ertl. *Phys. Rev. Lett.*, **82**, 3839 (1999).
- [34] J. Trost, T. Zambelli, J. Wintterlin, and G. Ertl. *Phys. Rev. B*, **54**, 17850 (1996).
- [35] T. Zambelli, J. Trost, J. Wintterlin, and G. Ertl. *Phys. Rev. Lett.*, **76**, 795 (1996).
- [36] J. Trost, J. Wintterlin, and G. Ertl. *Surf. Sci.*, **329**, L583 (1995).
- [37] G. Ertl. *Adv. Catal.*, **45**, 1 (2000).
- [38] T. Engel and G. Ertl. *J. Chem. Phys.*, **69**, 1267 (1978).
- [39] T. Matsushima. *Surf. Sci.*, **127**, 403 (1983).
- [40] T. Matsushima and H. Asada. *J. Chem. Phys.*, **85**, 1658 (1986).
- [41] H. Conrad, G. Ertl, J. Küppers, and E. E. Latta. *Surf. Sci.*, **65**, 245 (1977).
- [42] H. Over. *Prog. Surf. Sci.*, **58**, 249 (1998).
- [43] G. Odörfer, E. W. Plummer, H. J. Freund, H. Kuhlenbeck, and M. Neumann. *Surf. Sci.*, **198**, 331 (1988).
- [44] R. Imbihl and J. E. Demuth. *Surf. Sci.*, **173**, 395 (1986).

- [45] P. Légaré, L. Hilaire, G. Maire, G. Krill, and A. Amamou. *Surf. Sci.*, **107**, 533 (1981).
- [46] L. Ruan, F. Besenbacher, I. Stensgaard, and E. Laegsgaard. *Phys. Rev. Lett.*, **70**, 4079 (1993).
- [47] E. G. Seebauer and C. E. Allen. *Prog. Surf. Sci.*, **49**, 265 (1995).
- [48] J. Wintterlin, R. Schuster, and G. Ertl. *Phys. Rev. Lett.*, **77**, 123 (1996).
- [49] T. Gießel, O. Schaff, C. J. Hirschmugl, V. Fernandez, K. M. Schindler, A. Theobald, S. Bao, R. Lindsay, W. Berndt, A. M. Bradshaw, C. Baddely, A. F. Lee, R. M. Lambert, and D. P. Woodruff. *Surf. Sci.*, **406**, 90 (1998).
- [50] X. Guo and J. T. Yates Jr. *J. Chem. Phys.*, **90**, 6761 (1989).
- [51] M. Tüshaus, W. Berndt, H. Conrad, A. M. Bradshaw, and B. Persson. *App. Phys. A*, **51**, 91 (1990).
- [52] M. K. Rose, T. Mitsui, J. Dunphy, A. Borg, D. F. Ogletree, M. Salmeron, and P. Sautet. *Surf. Sci.*, **512**, 48 (2002).
- [53] S. Behler, M. K. Rose, J. C. Dunphy, D. F. Ogletree, M. Salmeron, and C. Chapelier. *Rev. Sci. Instrum.*, **68**, 2479 (1997).
- [54] T. Engel. *J. Chem. Phys.*, **69**, 373 (1978).
- [55] H. Conrad, G. Ertl, J. Koch, and E. E. Latta. *Surf. Sci.*, **43**, 462 (1974).
- [56] G. Ertl, M. Neumann, and K. M. Streit. *Surf. Sci.*, **64**, 393 (1977).
- [57] J. L. Gland and E. B. Kollin. *J. Chem. Phys.*, **78**, 963 (1983).
- [58] M. Silverberg, A. Ben-Shaul, and F. Rebentrost. *J. Chem. Phys.*, **83**, 6501 (1985).
- [59] M. A. Barteau, E. I. Ko, and R. J. Madix. *Surf. Sci.*, **104**, 161 (1981).
- [60] S. Völkening and J. Wintterlin. *J. Chem. Phys.*, **114**, 6382 (2001).

- [61] C. J. Zhang and P. Hu. *J. Am. Chem. Soc.*, **123**, 1166 (2001).
- [62] P. Sautet, M. K. Rose, J. C. Dunphy, S. Behler, and M. Salmeron. *Surf. Sci.*, **453**, 25 (2000).
- [63] Y. D. Kim, H. Over, G. Krabbes, and G. Ertl. *Top. Catal.*, **14**, 95 (2001).
- [64] N. Cant, P. C. Hicks, and B. S. Lennon. *J. Catal.*, **54**, 372 (1978).
- [65] C. Stampfl and M. Scheffler. *Surf. Sci.*, **433**, 119 (1999).
- [66] C. H. F. Peden, G. S. Herman, I. Z. Ismagilov, B. D. Kay, M. A. Henderson, Y.-J. Kim, and S. A. Chambers. *Catal. Today*, **51**, 513 (1999).
- [67] H.-I. Lee and J. M. White. *J. Catal.*, **63**, 261 (1980).
- [68] K. Christmann. *Introduction to Surface Physical Chemistry*. Springer, New York (1991).
- [69] T. E. Madey, H. A. Engelhardt, and D. Menzel. *Surf. Sci.*, **48**, 304 (1975).
- [70] V. I. Savchenko, G. K. Boreskov, A. V. Kalinkin, and A. N. Salanov. *Kinet. Catal.*, **24**, 983 (1983).
- [71] C. H. F. Peden and D. W. Goodman. *J. Phys. Chem.*, **90**, 1360 (1986).
- [72] C. H. F. Peden, D. W. Goodman, M. D. Weisel, and F. M. Hoffmann. *Surf. Sci.*, **253**, 44 (1991).
- [73] C. H. F. Peden. In F. M. Hoffmann D. J. Dwyer, ed., *Surface Science of Catalysis*. American Chemical Society, Washington, DC (1992).
- [74] A. Böttcher, H. Niehus, S. Schwegmann, H. Over, and G. Ertl. *J. Phys. Chem. B*, **101**, 11185 (1997).
- [75] C. Stampfl and M. Scheffler. *Phys. Rev. B*, **54**, 2868 (1996).
- [76] C. Stampfl, S. Schwegmann, H. Over, M. Scheffler, and G. Ertl. *Phys. Rev. Lett.*, **77**, 3371 (1996).
- [77] A. Böttcher, M. Rogozia, H. Niehus, H. Over, and G. Ertl. *J. Phys. Chem. B*, **103**, 6267 (1999).

- [78] R. L. Burwell, G. L. Haller, K. C. Taylor, and J. F. Read. *Adv. Catal.*, **20**, 1 (1969).
- [79] G. K. L. Cranstoun and D. R. Pyke. *Appl. Surf. Sci.*, **2**, 359 (1979).
- [80] G. K. L. Cranstoun, D. R. Pyke, and G. D. W. Smith. *Appl. Surf. Sci.*, **2**, 375 (1979).
- [81] W. J. Mitchell and W. H. Weinberg. *J. Chem. Phys.*, **104**, 9127 (1996).
- [82] Lj. Atanasoska, W. E. O'Grady, R. T. Atanasoski, and F. H. Pollak. *Surf. Sci.*, **202**, 142 (1988).
- [83] R. R. Daniels, G. Margaritondo, C.-A. Goerg, and F. Lévy. *Phys. Rev. B*, **29**, 1813 (1984).
- [84] A. K. Goel, G. Skorinko, and F. H. Pollak. *Phys. Rev. B*, **24**, 7342 (1981).
- [85] Y. D. Kim, A. P. Seitsonen, and H. Over. *Phys. Rev. B*, **63**, 115419 (2001).
- [86] Y. D. Kim, A. P. Seitsonen, S. Wendt, J. Wang, C. Fan, K. Jacobi, H. Over, and G. Ertl. *J. Phys. Chem. B*, **105**, 3752 (2001).
- [87] A. P. Seitsonen, Y. D. Kim, S. Wendt, and H. Over. *Phys. Rev. B*, **65**, 035413 (2001).
- [88] J. Wang, C. Y. Fan, K. Jacobi, and G. Ertl. *Surf. Sci.*, **481**, 113 (2001).
- [89] C. Y. Fan, J. Wang, K. Jacobi, and G. Ertl. *J. Chem. Phys.*, **114**, 10058 (2001).
- [90] J. Wang, C. Y. Fan, K. Jacobi, and G. Ertl. *J. Phys. Chem. B*, **106**, 3422 (2002).
- [91] H. Over, A. P. Seitsonen, E. Lundgren, M. Wiklund, and J. N. Andersen. *Chem. Phys. Lett.*, **342**, 467 (2001).
- [92] H. Madhavaram, H. Idriss, S. Wendt, Y. D. Kim, M. Knapp, H. Over, J. Aßmann, E. Löffler, and M. Muhler. *J. Catal.*, **202**, 296 (2001).

- [93] A. Böttcher, B. Krenzer, H. Conrad, and H. Niehus. *Surf. Sci.*, **466**, L811 (2000).
- [94] A. Böttcher, B. Krenzer, H. Conrad, and H. Niehus. *Surf. Sci.*, **504**, 42 (2002).
- [95] H. Over, A. P. Seitsonen, E. Lundgren, M. Schmid, and P. Varga. *J. Am. Chem. Soc.*, **123**, 11807 (2001).
- [96] H. Over, A. P. Seitsonen, E. Lundgren, M. Schmid, and P. Varga. *Surf. Sci.*, **515**, 143 (2002).
- [97] A. Böttcher, H. Conrad, and H. Niehus. *Surf. Sci.*, **478**, 229 (2001).
- [98] S. Wendt, A. P. Seitsonen, Y. D. Kim, M. Knapp, H. Idriss, and H. Over. *Surf. Sci.*, **505**, 137 (2002).
- [99] K. Reuter and M. Scheffler. *Surf. Sci.*, **490**, 20 (2001).
- [100] K. Reuter and M. Scheffler. *Phys. Rev. B*, **65**, 035406 (2002).
- [101] K. Reuter, M. Veronica Ganduglia-Pirovano, C. Stampfl, and M. Scheffler. *Phys. Rev. B*, **65**, 165403 (2002).
- [102] Z.-P. Liu, P. Hu, and A. Alavi. *J. Chem. Phys.*, **114**, 5956 (2001).
- [103] P. Mars and D. W. van Krevelen. *Chem. Eng. Sci. Suppl.*, **3**, 41 (1954).
- [104] H. Idriss and M. A. Barteau. *Adv. Catal.*, **45**, 261 (2000).
- [105] M. Todorova, W. X. Li, M. V. Ganduglia-Pirovano, C. Stampfl, K. Reuter, and M. Scheffler. *Phys. Rev. Lett.*, **89**, 096103 (2002).
- [106] E. Bauer. *Z. Krist.*, **110**, 372 (1958).
- [107] A. Steltenpohl and N. Memmel. *Surf. Sci.*, **402**, 277 (1998).
- [108] K. Bromann, H. Brune, H. Röder, and K. Kern. *Phys. Rev. Lett.*, **75**, 677 (1995).
- [109] M. Gsell, P. Jakob, and D. Menzel. *Science*, **280**, 717 (1998).
- [110] P. Müller and R. Kern. *Surf. Sci.*, **467**, 229 (2000).

- [111] K. H. Hansen, T. Worren, S. Stempel, E. Lægsgaard, M. Bäumer, H. J. Freund, F. Besenbacher, and I. Stensgaard. *Phys. Rev. Lett.*, **83**, 4120 (1999).
- [112] G. Wulff. *Z. Kristallogr.*, **34**, 449 (1901).
- [113] C. Herring. In Gomer-Smith, ed., *Structure and Properties of Solid Surfaces*, 5. Univ. Chicago Press, Chicago, IL (1953).
- [114] W. L. Winterbottom. *Acta. Metall.*, **15**, 303 (1967).
- [115] F. K. Legoues, M. C. Reuter, J. Tersoff, M. Hammar, and R. M. Tromp. *Phys. Rev. Lett.*, **73**, 300 (1994).
- [116] D. Eaglesham, F. Unterwald, and D. Jacobson. *Phys. Rev. Lett.*, **70**, 966 (1993).
- [117] H. Wolter, K. Meinel, Ch. Ammer, K. Wandelt, and H. Neddermeyer. *J. Phys.: Condens. Matter.*, **11**, 19 (1999).
- [118] M. Giesen, C. Steimer, and H. Ibach. *Surf. Sci.*, **471**, 80 (2001).
- [119] G. Schulze Icking-Konert, M. Giesen, and H. Ibach. *Phys. Rev. Lett.*, **83**, 3880 (1999).
- [120] V. E. Henrich and P. A. Cox. *The Surface Science of Metal Oxides*. Cambridge Univ. Press, Cambridge (1996).
- [121] U. Diebold, J. F. Anderson, K.-O. Ng, and D. Vanderbilt. *Phys. Rev. Lett.*, **77**, 1322 (1996).
- [122] E. Lundgren, G. Kresse, C. Klein, M. Borg, J. N. Anderson, M. De Santis, Y. Gauthier, C. Konvicka, M. Schmid, and P. Varga. *Phys. Rev. Lett.*, **88**, 246103 (2002).
- [123] A. Alavi, P. Hu, T. Deutsch, P. L. Silvestrelli, and J. Hutter. *Phys. Rev. Lett.*, **80**, 3650 (1998).
- [124] P. A. Redhead. *Vacuum*, **12**, 203 (1962).
- [125] L. Lafosse, Y. Wang, and K. Jacobi. *J. Chem. Phys.*, **117**, 2823 (2002).
- [126] A. Seitsonen and H. Over. *High Performance Computing in Science and Engineering in Munich 2002*. Springer (2002).

- [127] A. Zangwill. *Physics at Surfaces*. Cambridge Univ. Press, Cambridge (1988).
- [128] M. Rössler, J. Wintterlin, and G. Ertl. *Verhandl. DPG (VI)*, **36**, 372 (2001).
- [129] I. Langmuir. *J. Am. Chem. Soc.*, **40**, 1361 (1918).

Acknowledgement

Looking back my stay in Germany at the end stage of my doctoral study, it is hardly necessary to say that there have been many direct and indirect contributors to this thesis.

My first and many thanks goes to Professor Dr. Joost Wintterlin, my supervisor, who showed me how to ‘research’ with his elaborate skills at apparatus and thoroughness at experiments and writing.

I am much obliged to Professor Dr. Gerhard Ertl, our department director, for his allowing my study and promoting very favorable working conditions at the Fritz Haber Institute, and for his generous support for my travel to inland and abroad conferences.

I am grateful to Professor Dr. H. Niehus and Professor Dr. R. Imbuhl, who readily appraised my thesis and to Ingeborg Reinhard and Waruno Mahdi, who corrected English in my manuscript.

Many thanks goes to my (former) colleagues, Mario Rößler, Javier Méndez, Stefano Marchini, Christian Sachs who created comfortable atmosphere in our group. They enabled me also to taste, at first not always understandable but now enjoyably accustomed, German or European way of life.

I am very grateful to Peter Geng, who helped me to construct oxygen shower system in the chamber, to the people in the electronic lab, workshops, and PP&B, who provided me excellent aid when some electronics went out of order or some mechanical components were needed or computers went on strike.

I am thankful to G. Weinberg who took SEM picture of STM tips for me.

Professor K. Jacobi and Stefan Wendt deserve my gratitude for active discussions about $\text{RuO}_2(110)$ experiments.

Colleagues from former Surfaces Physics Department, Rolf’s and Katharina’s group deserve also many thanks for having regularly lunch with

us, which always amused me and was usefully informative in and around the institute.

I specially thank to my Korean (former) colleagues in the institute, Young Dok Kim, Jaeyoung Lee, Tae Geun Noh, Jeong Won Kim, Seung Mi Lee, Minseok Kim, with whom I could gap in Korean freely, which cheered me.

Financial support through the scholarship for the doctoral study in Germany of the German Academic Exchange Service (DAAD) is gratefully acknowledged.

I wish to express my gratitude to the mental support from my family and family-in-law in Korea. At last but not least, I cannot find the words to thank Woo Sook's love, endurance, and sacrifice that gave me strength to get my way to this point. This thesis born in Berlin is dedicated to Namu, our son, who was also born in this city.

Curriculum Vitae

Name Sang Hoon Kim

Oct. 22th 1973 born in Changnyoung, Korea

Mar. 1980 - Apr. 1983 *Gong-Reung* Elementary School, Seoul, Korea

Apr. 1983 - Feb. 1986 *Hwi-Kyung* Elementary School, Seoul, Korea

Mar. 1986 - Feb. 1989 *Cheong-Ryang* Middle School, Seoul, Korea

Mar. 1989 - Feb. 1992 Seoul Science High School, Korea

Mar. 1992 - Jan. 1994 Study of Physics, Seoul National University, Korea

Feb. 1994 - Aug. 1995 Military Service in the Korean Army

Sep. 1995 - Feb. 1997 Study of Physics, Seoul National University

Feb. 1997 Bachelor of Science

Mar. 1997 - Feb. 1999 Study of Experimental Physics,
Graduate School at the Seoul National University

Feb. 1999 Master of Science (Prof. Y. Kuk)

Oct. 1999 to date Doctoral Student at the Fritz Haber Institute of
the Max Planck Society, Berlin, Germany
(Prof. Dr. G. Ertl, Prof. Dr. J. Wintterlin)

List of publications

- [1] Jeong Young Park, S. H. Kim, W. G. Park, and Y. Kuk :
Interference pattern of a coherent electron beam by localized leakage magnetic field, Appl. Phys. Lett., 78(12), pp. 1745-1747 (2001).
- [2] Jeong-Young Park, S. H. Kim, Y. D. Suh, W. G. Park, and Y. Kuk :
Low-energy electron point source microscope with position-sensitive electron energy analyzer, Rev. Sci. Instrum., 70(11), pp. 4304-4307 (1999).

Presentations

- [1] Sang Hoon Kim, J. Wintterlin, and G. Ertl :
Atomic scale investigations of the catalytic oxidation of CO on RuO₂(110), APS (American Physical Society) March Meeting 2002, Indianapolis, USA.
- [2] Sang Hoon Kim, J. Wintterlin, and G. Ertl :
STM-Untersuchungen zur katalytischen Oxidation von CO auf RuO₂(110), DPG (German Physical Society) 2002, Mar. 2002, Regensburg, Germany.
- [3] Sang Hoon Kim, Javier Méndez, J. Wintterlin, and G. Ertl :
Atomic resolution of CO oxidation on Pd(111) with Scanning Tunneling Microscopy, 20th ECOSS (European Congress on Surface Science), Sep. 2001, Krakow, Poland.
- [4] Sang Hoon Kim, Javier Méndez, J. Wintterlin, and G. Ertl :
Atomare Auflösung der CO-Oxidation auf Pd(111) mit Rastertunnelmikroskop, DPG 2001, Mar. 2001, Hamburg, Germany.

Selbständigkeitserklärung

Hiermit erkläre ich, die vorliegende Arbeit selbständig ohne fremde Hilfe verfasst zu haben und nur die angegebene Literatur und Hilfsmittel verwendet zu haben.

Sang Hoon Kim
21. März 2003